POWER CONVERTERS FOR PHOTOVOLTAIC ENERGY GENERATION

a thesis submitted by

DANIEL MICHAEL KENNETH SCHOFIELD

in partial fulfilment of the requirements of the degree of
Doctor of Philosophy

in

THE DEPARTMENT OF ELECTRONIC AND ELECTRICAL ENGINEERING AT THE UNIVERSITY OF SHEFFIELD

supervised by

DR MARTIN P. FOSTER AND PROF. DAVID A. STONE

APRIL 2014

SUMMARY

Global demand for renewable energy has provided impetus for increased research into photovoltaic (PV) technology. Photovoltaic modules have intrinsically low efficiency and therefore, to maximise generated electricity, advances must be made in the efficient extraction of energy to maintain viability of their use. In this thesis, efficiency is maximised using novel power electronics.

To facilitate advanced design, novel methods for generating accurate models of PV generators are presented. Conventional methods rely on the characterisation of PVs under continuous illumination. These methods cause heating of the module which can degrade the performance below that which would be seen during normal operation. To counter this problem, the use of flashed illumination is presented as a method for unobtrusively generating a PV electrical characteristic which can be used for accurate model-parameter extraction.

To develop optimised-switch mode power converters for PVs, the reasons for suboptimal operation in existing converters is analysed and validated experimentally. Whereas existing research has considered the effect of current perturbation at mains frequency, this thesis extends the analysis to 500 kHz, which represents typical switchmode operation. A typical boost converter cannot meet the requirements for optimal power extraction from the PV module and therefore a novel circuit topology based on a SEPIC converter which can achieve optimal conditions is developed and presented.

Since the methods for power transfer optimisation presented in this thesis require that the additional hardware is implemented in order to take full advantage of the PV generator, a method is presented whereby the resulting increased cost is significantly reduced. This reduction is achieved through the adaptation of redundant computer power supplies for PV battery charging applications, a method which can be used to produce a PV battery charger with minimal material or design investment.

THIS THESIS IS DEDICATED TO THE MEMORY OF

MICHAEL FRANK SCHOFIELD

whilst he currently resides in a
stacker-box at the back of the study,
his love and encouragement
knows no such bounds

Fliegt heim, ihr Raben!
Raunt es eurem Herren,
was hier am Rhein ihr gehört!
An Brünnhildes Felsen
fahrt vorbei! ≠
Der dort noch lodert,
weiset Loge nach Walhall!
Denn der Götter Ende
dämmert nun auf.
So ≠ werf ich den Brand
in Walhalls prangende Burg.

- Richard Wagner,
Der Ring des Nibelungen

ACKNOWLEDGMENTS

For showing spite to all challenges and difficulties, I would like to acknowledge the contributions of my supervisors, Martin Foster and Dave Stone for their continued support throughout my study.

For his limitless skills of bodgery, I'd like to particularly thank Daniel Rogers.

For the love and kind words of encouragement, I would like to thank my family and friends, without whom I would not have had the strength and sheer bloody-mindedness to persevere.

AUTHOR'S PUBLICATIONS

[1] D. M. K. Schofield, M. P. Foster, and D. A. Stone, "Low-cost solar emulator for evaluation of maximum power point tracking methods," *Electronics Letters*, vol. 47, no. 3, p. 208, 2011.

[2] D. M. K. Schofield, M. P. Foster, and D. A. Stone, "Impact of ripple current on the average output power of solar cells," in *6th IET International Conference on Power Electronics, Machines and Drives (PEMD 2012)*, 2012, pp. D43–D43.

[3] D. Rogers, J. Green, M. Foster, D. Stone, D. Schofield, S. Abuzed, and A. Buckley, "Repurposing of ATX computer power supplies for PV applications in developing countries," in *2013 International Conference on Renewable Energy Research and Applications (ICRERA)*, 2013, pp. 973–978.

[4] D. M. K. Schofield, S. Abuzed, M. P. Foster, D. A. Stone, D. J. Rogers, and J. E. Green, "Second life of computer power supplies in PV battery charging applications," in *2013 15th European Conference on Power Electronics and Applications (EPE)*, 2013, pp. 1–10.

[5] D. Rogers, J. Green, M. Foster, D. Stone, D. M. K. Schofield, B. Alastair, and S. Abuzed, "ATX power supply derived MPPT converter for cell phone charging applications in the developing world," in *Proceedings of 2014 The 7th IET international conference on Power Electronics, Machines and Drives*, 2014.

[6] D. Rogers, J. Green, M. Foster, D. Stone, D. Schofield, S. Abuzed, and A. Buckley, "A low cost photovoltaic maximum power point tracking buck converter for cell phone charging applications," in *Proceedings of PCIM Europe 2014*, 2014.

TABLE OF CONTENTS

Chapter 1 - Introduction

1.1 - Background and motivation

Influences of modern society have dictated that an ever increasing proportion of electrical power must be generated from both renewable and low-carbon technologies. Low carbon technologies are qualified by the one metric – the particularly low volume of carbon-dioxide equivalent gases produced by their implementation. The term low-carbon has been erroneously applied by many authors and journalists to imply that the implementation of technology is carbon-emitting at only the point of use. The term low-carbon must be applied more generally over the full lifecycle, from resource extraction to disposal. For the aforementioned reasons, the term low-carbon will rarely encompass photo-voltaic energy generation methods, where, including the initial production of carbon-dioxide during the semiconductor fabrication and transportation costs, a signification quantity of carbon-dioxide is produced.

The practically of PV energy generation is promoted in this thesis beyond its problems of lifecycle carbon-dioxide production. The primary benefits of PV energy generation championed are that its operation consumes no fuel and does not involve moving mechanical parts that require frequent maintenance. For these reasons PV technology presents an ideal source of energy for remote areas and applications including the charging of backup energy storage in instrumentation and communications. The low profile nature of a small PV installation makes it also ideal for high penetration implementation in urban environments where wind-turbines and more mechanical options lose favour.

1.2 - PV Basics

One of the earliest reference to the harnessing of power from sunlight is by Aristophanes [7] in his play, “The Clouds”, which refers to a Burning Glass used to create intense beams of the sun’s light for the lighting of fires. Photo-voltaic applications later became evident to scientists from 1839 with the

discovery of the photovoltaic effect by A. E. Becquerel. The photovoltaic effect was initially the result of work performed using silver-chloride and platinum electrodes in acidic solutions [8]. The Becquerel effect, as it later became known, was left as a matter of scientific curiosity with no real capacity for useful power generation nor the demand for electricity at that time. By 1883, sufficient understanding had been gained with semiconducting selenium devices that the first photovoltaic cell was produced using semiconductors boasting an efficiency approaching 1%, primarily used for measurement of light intensity. Circa 1950 some of the principal ideas of the understanding of the effect were established, and recognised as an important technology for electricity generation along with a growing demand for electricity in the world [9], [10]. Advances in semiconductors and the understanding of electromagnetic quanta permitted the first practical photovoltaic cell in 1954 [11]. Continued developments in semiconductor fabrication techniques to the present day have increased the efficiency of commercial PV cells to nearly 16% and growing demand has reduced the cost to a level where they form a practical generation method for large quantities of electrical power.

1.2.1 - Production of cells

Modern fabrication methods produce individual PV cells from a wafer of silicon cut from a large ingot. A PN junction is formed by the addition of dopant atoms to the silicon wafer, commonly through thermal diffusion. Because of the processing techniques applied to wafers individually, there is a wide scope for variations between individual cells, further increased between batches. This factor is one of many that make PV cells tend to imbalance in parallel connection [12], this is due to a large imbalance of the generated voltages. Process variations make it only practical to form PV modules by connecting cells in series. Operation at increased system voltage is a measure that can also increase the efficiency of an installation by maximising the voltage and reduced current in main bus cabling for the reduction of ohmic losses..

1.2.2 - Characteristics of PV generators

The semiconductor makeup of a PV cell gives it non-linear electrical characteristics. The electrical characteristics have been extensively studied in literature. The result of the extensive studies has been a number of models, all of which are centred on a diode and current source and represent varying degrees of accuracy by which can be used to reproduce a characteristic from experimental data. The varying degrees of accuracy come primarily from the type of characteristic import to the user. Dependent on the required DC accuracy a number of elements can be omitted and if required, high frequency AC characteristics can be represented. The AC characteristics, however, rely on certain parameters such as cable inductance, inductance due to the cell arrangement and parasitic elements that are all very difficult to determine with any degree of accuracy. In most reported cases, a simplified model is sufficient.

Where multiple cells are connected in series and non-uniformly illuminated a phenomenon known as partial shading is apparent. This reduction occurs by the reverse bias of the shaded cells in the absence of a photo-current. The voltage drop produced by the reverse bias subtracts from the module voltage and can be more so apparent with increased current. Many effects change the characteristics of a partial shading event including the degree of shading i.e. the number of cells shaded. Since partial shading events can produce local maxima in the power curve it is particular interest to the study of MPPT algorithms, the presence of local maxima can 'mislead' most basic algorithms. The often significant power loss due to partial shading also places a large constraint on the location of PV modules and in urban environments, where the majority of houses possess chimneys, due consideration of the partial shading due to these obstacles is key to the successful operation of the installation.

1.3 - Basics of power conversion

Modern methods of power conversion rely on switching devices capable of producing square waveforms that can be used to excite various combinations and structures of rectifiers and filters to

produce DC/DC converters. Direct-current transformers represent a small subset of the power conversion methods. When supplied with DC power, a number of switching devices are used to produce an alternating magnetic flux in a transformer which subsequently acts on secondary windings to produce a voltage which is then rectified and smoothed to produce a DC output. Whilst in general encompassing DC transformers, the term power converter is taken to imply the remaining subset of power conversion methods. A standard switching power converter will use a switching device to 'chop' the DC waveform such that it has a significant number of harmonic components. The exact nature of the switching can be used to produce a modulation that is used by a filter to produce a variable DC output. The use of switching devices operating at high frequency permit the use of smaller filter components that reduce the size of the converter and increase its efficiency. One key benefit to PV systems is the ability of switch mode power conversion techniques to produce both step-up and step-down topologies.

1.4 - Literature review

1.4.1 - Characterisation of PV cells

PV modules can operate under numerous ranges and extents: both electrical and environmental. Typical applications range from the application of small arrays which can operate under uniform illumination conditions, to larger arrays which cannot but operate under non-uniform conditions due to the nature of sunlight. A third category exists whereby a physically small PV cell or module is used under concentrated conditions whereby the total irradiation on the cell is increased much beyond typical insolation levels, typically with the use of mirrors collecting and focusing light from a wide area on the small cell.

The basic models for the approach have been established primarily from the original investigations of Shockley et al, on PN junction behaviour and models [13]. Models presented in external literature are based primarily on the physics of the interaction of light with matter and from practical

observations of parasitic resistances. The original efforts first occurrence of the illuminated single diode model used extensively in this thesis and other literature [14–17].

The treatment of PV characterisation is further considered in the bounds of concentrated PV, under this mode of operation, the incident irradiation is many times greater than the nominal. As such, a greater efficiency-power product per-unit-cost can be attained [18]. A smaller quantity of greater efficiency materials can be used; along with a reduced area of high performance protective media can be utilised by the minimal additional cost of reflectors (concentrators). Under these conditions, whilst many of the model parameters remain similar to normal circumstances, the much increased current density make certain parasitic elements more prominent [18–20].

Partial shading, or non-uniform illumination conditions form a subset of the conditions under which a PV module can be modelled, under these conditions, a number of the module's cells remain unilluminated, and as connected in a series string present a large voltage drop, which drops much of the voltage of the illuminated string, this presents a large reduction of power. Treatment of the modelling of solar cells under partial shading is provided by [17], [21], [22]. The simplified PV, single diode model is used extensively in this thesis because of the accuracy with which it can represent an entire PV module characteristic [16]. This treatment is performed particularly in Chapter 2 of this thesis.

1.4.2 - MPPT Methods

Maximum power point tracking is a technique applied to the control of a power converter attached to a solar cell which optimises the output power from the solar cell by varying the operating point in terms of voltage and current. A review of the various MPPT methods is provided by Hohm et al [16], this work demonstrates all of the methods that are commonly used in industrial applications.

The use of perturbation and observation (P&O) based algorithms have been most widely adopted because of the minimal complexity and computational power with which a robust system can be produced. The deficiency of such P&O algorithms have been treated primarily with regard to their

dependence on increased resolution analogue to digital converters (ADCs) required to reduce the average deviation from the maximum power point (MPP). In contrast however, research has been performed that indicate the system is made less stable by the use of higher resolution ADCs by causing greater susceptibility to noise. The deficiency of P&O algorithms has been widely addressed in literature with the introduction of variable step-size and hybrid algorithms [23–25].

1.4.3 - Characterisation of dynamic systems and PV cell parasitic capacitance

Knowledge of the solar cell parasitic capacitance is crucial to some MPPT mathods, in particular the parasitic capacitance method. The parasitic capacitance model is not often used because of this difficulty. Knowledge of the parasitic capacitance is required in this method to determine the direction of the MPP [16].

Capacitance measurement techniques generally rely on using a discharged capacitance and performing an injection of either a determined charge or by raising the capacitor to a determined voltage, a method of calculating the parasitic capacitance whilst the solar cell is on-line (under normal operating conditions) is required. The use of maximum length sequences (MLS) generated by pseudo-random binary sequence generators has been long accepted as a method of characterisation of simple systems [26]. Frequency domain methods exist in various guises, a sinusoidal perturbation can be applied to the current drawn by the load and then swept in frequency, as is the technique performed by many network analysers, however, this process is time consuming and to perform the measurement in a time which will prevent the changing sunlight conditions from having an effect on the measurement would require a costly piece of equipment [27].

1.4.4 - Classical and Heuristic problem solving methods

Mathematical models presented for the solar cells must be converted to a form that can easily be solved by a computer for the purpose of simulation, various methods of equation solving are discussed in [28]. Classical methods of numerical root finding or equation solving are typically used where the

equation does not have an analytical root. This is typical of many PV equations; they are based around an exponential element from the Shockley diode equation. For some simplified cases there is an analytical solution but it has been demonstrated where parasitic components are included the model-equation becomes implicit, containing transcendental functions [29], [30]. Gradient methods such as the Newton Rhapson method require that a derivative can be calculated, the majority of PV based equations are differentiable and as such an be appropriate and would be an efficient solving mechanisms. In some cases where hard constraints are used, the equation becomes non-differentiable and as such gradient methods can no longer be used and an algorithm not requiring a derivative is required. An example of such an algorithm that does not require a derivate is the Van Windergarten Dekker Brent (VWDB) method [28]. Some work in this thesis has required the computation of solutions to PV derived equations as part of wider optimisation routines (see Chapter 3 development of a PV emulator) and require attention to computational efficiency. The VWDB method has been used for this purposes because of its computational efficiency as a non-gradient method [28], a gradient method would still demonstrate greater computational efficiency. Furthermore, the VWDB method offers an increased range of convergence over the Newton-Rhapson method which reduces the a-priori knowledge of the system required.

Heuristic methods are used for equation solving and problem solving where the search space exceeds the limitations of computing power and where tailored solutions are unobtainable [31], [32].

Methods of parameter estimation using genetic algorithms showing advantages over traditional search methods are presented by Jervase et al [33] and Lingyun et al [31], which show a much greater agreement between the derived model and experimental data than comparative classical methods, however with decreased repeatability and dependability.

1.4.5 - Single inductor hard-switched converters

Single inductor hard switched converters are the fundamental building blocks of switched mode power supply development. From the boost and buck converter, numerous combinations can be

achieved. Both Mohan [34] and Severns [35] extensively deal with the development of power supply types.

Hard-switched power converters have been used extensively for PV system power interfaces and MPPT, extensive works have been produced on their design and optimisation using traditional methods [36–38]. Works are also presented for topics relevant to the design of converters for PV systems, such as low current-ripple techniques [39–43]. Techniques for the analysis of such power converters are also discussed in [44].

1.4.6 - Transfer efficiency

Transfer efficiency, that is commonly defined as the ratio of average power extracted from a PV module to that at MPP conditions, is dealt with in Chapter 4. This matter is concerned with the investigation of high frequency effects of switched mode power supplies (SMPSs) on the average output power. This has received little attention in literature (Benevides et al [45]), but more prominently, the effects due to mains related fluctuations is dealt with in great details [22], [46]. These flow frequency effects arise from primarily from the power pulsations of energy driven into the grid. This is of greater importance where there is no energy storage device between the MPPT front end and the grid feeding inverter.

1.4.7 - Soft-switched switch-mode power converters

Resonant power supplies are a broad class of power converters which generally share the common advantage that greater switching frequency can be achieved without the associated increased loss [47–51]. One of the properties of transfer efficiency is that increased transfer efficiency can be exploited at increased frequency, due to the filtering effect of the parasitic elements of the PV module. The total system, efficiency, as previously stated is considered as the combined transfer efficiency and power converter efficiency. The application of the requirements for increased transfer efficiency (decreased ripple and increased frequency) has been shown to degrade the total system efficiency in Chapter 5.

The degradation of total system efficiency is due primarily to the reduction of power converter efficiency under conditions for increased transfer efficiency, and a reduction in the power transfer efficiency at conditions of improved power converter efficiency. Resonant power converters thus present one method by which increased transfer efficiency conditions can be implemented without the associated increased losses of a hard-switched power converter. This matter has not been exploited explicitly, however, extensive research has been performed in the field of resonant power converters for PV applications [39], [50], [52], [53].

1.4.8 - Multiple-inductor hard-switched converters

Multiple inductor hard switched converters are an evolution of single inductor power converters that operate with two inductors and can achieved a greater range of operation. The Ćuk and SEPIC converter topologies form the two most prominent converter topologies in this area. The Ćuk and SEPIC converter were initially studied by Ćuk and Middlebrook [35] who performed numerous investigations with the integration of the two inductors into a single magnetic components. This showed the most favourable property of the Ćuk and SEPIC converter being their ability to operate in a zero ripple conditions where the current ripple in either the input or output inductors can be forced to zero by the action of the output or input current ripple respectively. For this reason, the SEPIC converter has been used in this thesis in the solution to the problem of current ripple.

The use of interleaved power converters is also extensively studied in literature. The primary focus for this attention is the reduction of ripple and noise for EMC requirements [54]. Multi-phase separation in the switching of identical converters presents one method by which the efficiency can be kept constant whilst increasing the frequency of the ripple perturbation seen by the source [55], [56]. These have been extensively studied in power factor correction and front end power modules where conducted noise and ripple is of foremost concern. Alternative methods to achieve reduced ripple amplitude have been studied by Tsang et al [57] and Testa et al [58] which achieved minimal ripple conditions with marginal impact on the efficiency of the power converter.

1.4.9 - Solar emulators

A solar emulator is a device which can replicate the characteristics of a solar cell, but in a repeatable and programmable way, works on the design of high power solar emulators are given in [59–62]. A system for producing an arbitrary output characteristic using analogue circuits is provided by [63].

Commercial systems are available for the emulation of PV characteristics. These commercial devices are aimed at much greater power ratings than are required in this work [64]. These power ratings dictate that use of a switched mode output power stage in these devices and as such demand the use of a switched mode output stage. This kind of output stage has been deemed unsuitable for the work contained in this thesis due to the effects of switching noise on small signal measurements. Such devices were also primarily developed for applications including high power PV array installations where the prototype array is too large for installation in a laboratory for testing under artificial illumination. For the power levels commonly dealt with in this thesis, the commercial call for an emulator is very small. In more recent years, commercial offerings have become available from the likes of Agilent Technologies [65] in the form of 600 W PV emulators, however these only were commercialised towards the end of this research period.

The techniques for producing an emulation system as shown in Chapter 4 are based on analogue computational methods. These methods are dealt with in [66], [67].

1.4.10 - SMPC control mechanisms

Fundamentally, the control of SMPCs comes in two flavours; these are voltage mode and current mode control [34]. Voltage mode control is most typically used in situations where a stiff voltage source is used to power a SMPC which too is designed to produce a stiff voltage source at differing voltage [35]. This kind of control works best where there is minimal compliance on the input voltage and the output voltage is freely controlled, i.e. unaffected by any fixed voltage sources as in battery charging applications. In battery charging applications the output voltage must comply with the

battery voltage which has a very low incremental resistance and as such small variations in voltage produce very large variations in current [40]. In contrast, current mode control offers maximum voltage compliance and maximum control range in current; this is true of the input voltage also. The input voltage is heavily dependent on the current over certain operating regions, this compliance is best dealt with by current mode control. Current mode control is extensively studied by Middlebrook et al [68], [69] and in particular [70] with regard to PV applications.

1.4.11 - Automatic control systems

A discussion of automatic control systems is presented in [71] which is a well established text book on the subject, a practical guide to control engineering is also presented in [72]. Photovoltaic systems are subject to a wide range of operating conditions that vary with ambient conditions. The design of a simple controller must be designed to operate over a wide range of conditions and thus will, in general, at any one condition be sub-optimal. PV applications generally demand adaptive control algorithms. Self-tuning control is a subset of the adaptive control algorithms. Self-tuning controllers perform online parameter estimation and system identification and calculate the optimum controller solution. The calculated parameters can therefore drift significantly where there is minimal excitation to aid the identification process. A solution to this problem provided by direct model referenced adaptive control in which a primitive model provides some excitation to the adjustment mechanism.

1.4.12 - Reuse of power supplies

Very little engineering research has been performed on the subject of the reuse of computer power supplies for PV applications and discussed in this thesis. This section of work is however primarily supported with the use of consultation and government reports on the impact of recycling and the current infrastructure. The UK government has published the majority of its findings of the assessment of WEEE recycling routes and their effectiveness in [74]. Some engineering research has been performed on the state of health estimation of power supplies as dealt with in [75] and research

has been performed into potential future trends in power supplies as demonstrated in [76] which demonstrates the use of advanced power converter topologies to achieve new demands of efficiency, EMC compliance and manufacturing cost.

1.5 - Thesis outline

This thesis outlines and develops arguments for engineering choices for the design of high performance power converters for PV applications. An established problem in the field of PV power interfaces that has been originally quantified by this thesis is that of the effects of current ripple introduced in the PV system by the switching nature of a modern power converters, this matter has been quantified from both a theoretical standpoint and further developed through experimental work. Problems that have been long standing in the field of PV power interfaces, including research and development cost constraints and evaluation of conditions required for high efficiency power interfaces. The reduction of research and development investment for the evaluation of PV power interfaces is applied through the development of a low cost PV characteristic emulator in Chapter 3. Research into the optimum conditions for power converter operation (dealt with in Chapter 4) enhances the understanding of the limitations of certain power converter topologies for use in PV applications. Furthermore, methods which can enhance the update of PV technology in developing countries is put forth by the demonstration of the repurposing of computer power supplies for PV MPPT applications. This reuse matter demonstrates both a practical method of reducing material investment for the production of low cost MPPT systems which have uses in remote and developing countries, but also demonstrates a low initial investment development platform for PV applications.

1.5.1 - Chapter 2: A review of PV characterisation techniques

This chapter deals primarily with the comparison of various PV characterisation techniques that are relevant to the nature of work in this thesis. Characterisation is required for the identification of model parameters used in computer aided design methods and models in computer simulations.

Modern flashed illumination techniques are used in production units for the verification of PV module performance once constructed. A low duty-cycle flashed illumination source has a significantly reduced average power demand per watt-hour of light used to generate a meaningful characterisation. This reduced power supply demand is beneficial from the perspective of running-cost reduction in production plants. This characterisation is generally performed over a single flash using a rapidly swept load. This duration is often many orders of magnitude smaller than the thermal time-constant of the PV module and therefore it is practical to neglect the heating effect and produce characterisations at impractically low temperatures. This flashed method of characterisation is generally only considered for the energy saving benefits, however, it is demonstrated by the minimal additional heating that an improved characteristic can be obtained.

1.5.2 - Chapter 3: The development of a PV emulator

The development of a power interface for PV applications requires the use of a test method that can be used to produce easily reproducible results. For this purpose, a PV characteristic emulator is required. A PV characteristic emulator is a device that can accurately reproduce the voltage-current characteristics of a PV cell. Instruments for this purpose produced by various manufacturers are available commercially; however, the production instruments are focused on operating at much greater power levels than those required for small scale applications as used through this thesis. Furthermore, available instruments were identified as having switch-mode output stages that were immediately ruled out on the basis that noise would be an undesirable influence on the majority of testing that would be performed. On this basis it was decided that an instrument that meets the specific requirements would have to be developed. Literature has already been presented on the development of various systems that could perform the required task, however, based around obsolete technology, e.g. the solution presented by Marenholtz et al [59] relied on programming a characteristic by a number of cathode ray tube photo-emitters and detectors. A modern, solid-state version was required for this purpose.

The novel construction of the analogue PV emulator demonstrated by this chapter has been published in an IET Electronics Letter [1].

1.5.3 - Chapter 4: Analysis of the effects of power converter ripple on average PV output power

Early investigations based around the measurement of PV characteristics under load by switched-mode power converters were produced and demonstrated a significant voltage ripple due to the drawn current waveforms from aw SMPC containing a significant current ripple. The effects of this high frequency deviation from the average current was evaluation both by simulation and practical measurements. This produced the interesting result that the output power of a PV module is degraded by the presence of current ripple. This investigation presents a vital extension to the works of previous literature [45], [58], which has previously only investigated the effects up to 20 kHz. The investigation of the effect up to 500 kHz provides greater knowledge of the conditions under which the effects of reduced power can be eliminated.

The work demonstrated in this chapter have been presented at the Power Electronic Machines and Drives conference, 2012 [2].

1.5.4 - Chapter 5: A novel SEPIC converter for operation at maximum output power

In order to address the findings of Chapter 4 with regard to the optimum PV operating conditions in this chapter a novel extension of a SEPIC converter is proposed as a method by which the effects of current ripple previously elaborated can be minimised. The SEPIC converter is widely known for its continuous input current and buck-boost transfer characteristic. These factors make it highly suitable for PV operation. Literature on SEPIC converters has described methods that utilise the two inductors internal to a SEPIC converter with various degrees of magnetic coupling to achieve a nullification of this current ripple. This nullification is only applicable, to any great extent, over a narrow operating range of input and output voltage and load current. The wide range of power over which the SEPIC

converter must operate in a PV installation, however, does not make the previously presented nullification methods an effective option in PV applications.

1.5.5 - Chapter 6: The reuse of computer power supplies for PV systems

This chapter demonstrates how modifications to an arbitrary computer power supply to produce a power converter that can effectively operate under MPPT control. The focus of this work was to produce a small scale system capable of charging a battery for remote applications at low cost. Information from this chapter could be used to produce a working kit that could be, perhaps, used in a developing country to not only provide a low cost PV power solution, but also raise awareness and develop skills in electronic engineering required to make any modifications.

An initial scientific approach was used to assess the feasibility of modifications and predict the potential performance of the power converter. This assessment was used to expose the operational limits of the power converter elements when applies to the new electrical conditions (voltage and current ranges) applied by the PV module at the input and battery at the output.

Two regimes of modification are demonstrated: one which utilises only a power factor correction boost converter and one which can utilise both the power factor correction power converter and the bulk power conversion stages. The results of both of these circuits in operation with a 40 W PV module is demonstrated. The results show that a redundant ATX power supply can be adequately formed into an operational MPPT PV battery charger.

Chapter 2 - Photovoltaic models and characterisation methods

Photovoltaic characterisation is useful for a number of purposes. Foremost of these is the frequent requirement to obtain information about the electrical characteristics of the PV module. This information is required in industrial applications where quality control of module production is necessary, and for academic purposes where the characteristics inform models for theoretical evaluation of systems. An abstract model of the characterisation data is often required to support the simulation of a PV system that will later be used as part of the real system. The modelling of PV modules and cells takes many forms, each of which offer different advantages; for example, some models offer greater accuracy while some offer improved computational efficiency.

2.1 - PV Models

As previously described in Chapter 1, PV modules are constructed from a series combination of many PV cells. The single PV cell forms the basis for many of the models seen in the literature [15], [77]. Its behaviour, which is presented as an equivalent circuit in Figure 2-1, is derived directly from the characteristics of a PN junction diode [13], [77].

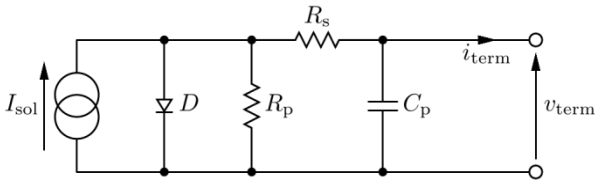

Figure 2-1: PV cell equivalent circuit

The parameters of the diode, D, are determined from the semiconductor material from which the cell is fabricated. The parallel resistance, R_p, is determined from bulk leakage resistance of the semiconductor material and, whilst strictly a component of the internal diode, is shown externally to the diode for clarity because its effect is not included in the Shockley equation used to model the diode element. The series resistance, R_s, is based partly on the bulk resistivity of the semiconductor

material, and partly on the resistance of the interconnects to the cell. Using the Shockley diode equation shown in (2-1) and following basic circuit analysis, an equation which describes the operation of a PV cell can be written. This equation is derived from the equivalent circuit model shown in Figure 2-1 and is given in (2-2).

$$I_{\mathrm{D}} = I_{\mathrm{sat}}\left(e^{\frac{V_{\mathrm{D}}}{nV_{\mathrm{T}}}} - 1\right) \tag{2-1}$$

Where: I_D is the forward current flowing through the diode element

V_{D} is the forward voltage dropped across the diode element

I_{sat} is the diode saturation current, derived from semiconductor material properties

V_{T} is the diode thermal voltage, derived from the semiconductor material (e.g. 25.9 mV for silicon at room temperature)

n is the diode emission coefficient, a form of quality factor, which takes the value of 1 for an ideal diode

$$I_{\mathrm{term}} = I_{\mathrm{sol}} - I_{\mathrm{sat}}\left(e^{\frac{V_{\mathrm{term}} - I_{\mathrm{term}}R_{\mathrm{S}}}{nV_{\mathrm{T}}}} - 1\right) - \frac{V_{\mathrm{term}} - I_{\mathrm{term}}R_{\mathrm{s}}}{R_{\mathrm{P}}} \tag{2-2}$$

Where the symbols have meanings previously defined in (2-1) and Figure 2-1.

By inspection, a direct mathematical solution to (2-2) does not exist as it is an implicit transcendental function. The implicit nature is introduced by the inclusion of R_s which introduces a term in I_{PV} within the exponential function. For this reason, and the fact that the resistance is usually very small, it is frequently not included in mathematical representations [29]. However, the equation (2-2) is solvable by numerical methods. These methods are, however, inefficient because they mostly perform an iterative solution. Alternatively, solutions can be obtained by circuit simulators; however, they tend to be no more computationally efficient than numerical methods because they still implement a numerical solution to the diode equation. To this end, SPICE is used extensively in this thesis for numerical solution of circuit models [78]. However, where a direct mathematical solution is desired for its increased speed and modelling accuracy is not critical, the parasitic elements R_s and R_p can be neglected by assigning them their limiting values of 0 and ∞ respectively and hence a direct solution to the equation can be made.

An example of a characteristic curve determined by SPICE simulation of the model is presented in Figure 2-2. On this curve, the two dominant regions of operation are identified, these being a voltage source region and a current source region. In between the voltage and current source regions there is a transition region in which the effect of the diode equation dominants.

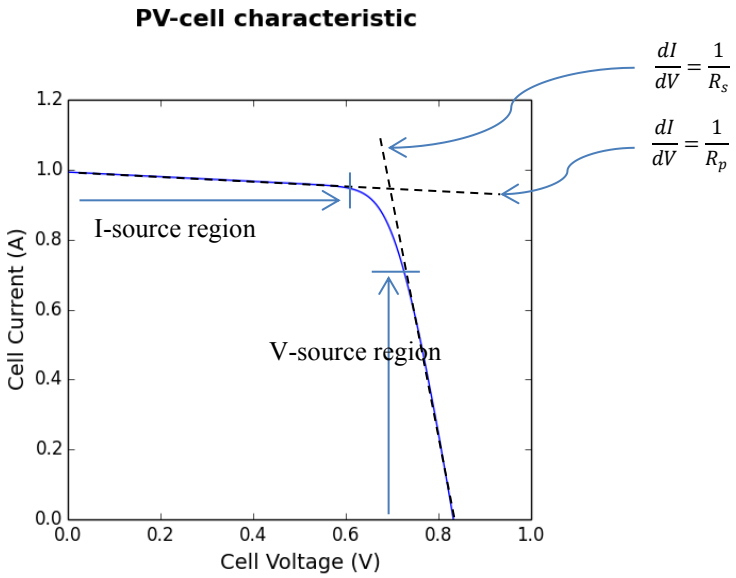

Figure 2-2: Single PV cell characteristic. The effects of parasitic elements from the model are identified. This curve is shown for constant I_{sol} = 1 A.

The effect of varying the series and parallel parasitic resistances are shown in Figure 2-3 and Figure 2-4 respectively. The particular region of the curve that is affected by the change in parasitic component can clearly be seen in both figures. In Figure 2-3, R_s was varied and the characteristics at {0.1, 0.3 and 0.5} Ω are shown; in each case R_p is 30 Ω. In Figure 2-4, R_p was varied and {10, 20 and 30} Ω are shown; in each case R_s is 0.1 Ω. For both figures, the other diode parameters are common and are as given in Table 2-1.

Parameter	**Value**
V_T (thermal voltage)	26 mV
I_s (reverse saturation current)	10^{-14} A

Table 2-1: Diode parameters used for simulation purposes (see Figure 2-3 & Figure 2-4)

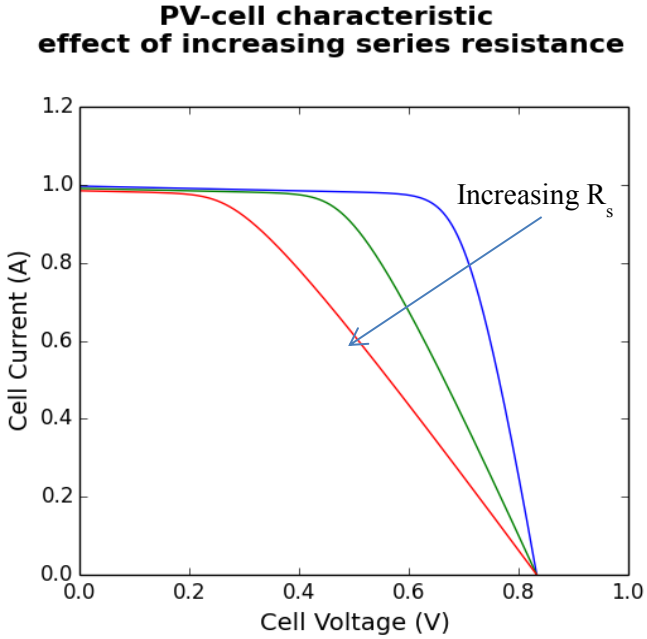

Figure 2-3: The effect of increasing series resistance, R_s, on the electrical characteristic of the PV cell. The greatest effect is visible in the constant voltage region of the characteristic.

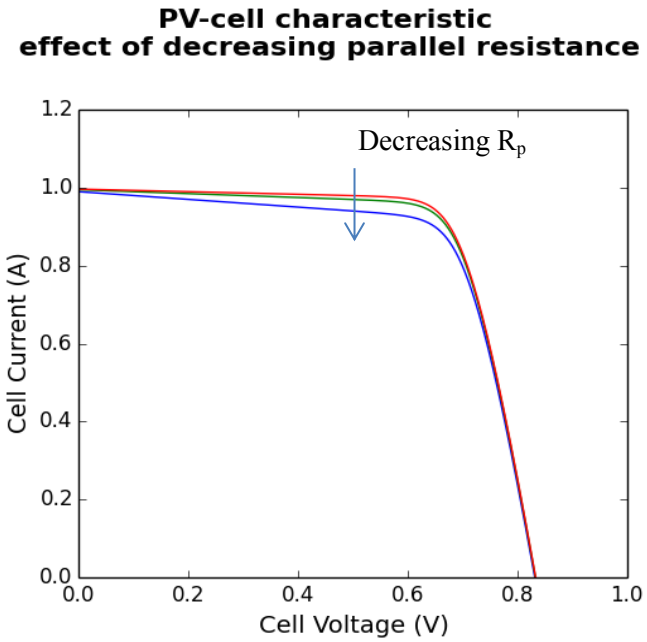

Figure 2-4: The effect of increasing parallel resistance, R_p, on the electrical characteristic of the module. The greatest effect is seen in the constant current region of the characteristic.

In practice, the value of R_s is often approximately constant throughout the operation of the module as it is primarily determined by the behaviour of the interconnection of the PV cells [30], a property which is not affected during operation. The value of parallel resistance, however, is highly dependent on temperature [13].

In Figure 2-5, the basic model (neglecting the parasitic components) for an illuminated diode is presented. This model is then used to form a dual series-connected PV module under uniform illumination conditions. It is evident from this figure and accompanying equations that a single cell model can be used additively in series combinations to derive models for series-connected modules. Because parallel combinations are very rarely seen in practice, they are not discussed in this thesis.

In contrast to Figure 2-5, Figure 2-6 presents a case where the two series-connected cells in a module are non-uniformly illuminated. The resulting equation relating module voltage and current for this case is shown in the figure. This model highlights a difficulty for the analysis of these non-uniform illumination patterns, as the resultant equation mathematically tends to negative-infinity as the overall module-current exceeds that of the most poorly illuminated cell. This theoretical tendency towards negative infinity is non-practical, especially where a single quadrant load is used, as voltage and current can only exist in the same quadrant. In reality, this partial shading results in the sudden injection of a high impedance (resulting from the reverse biased diode) resulting in the current falling to zero in practice, where it will remain unless the module is driven into an adjacent operating quadrant by the connected 'load'.

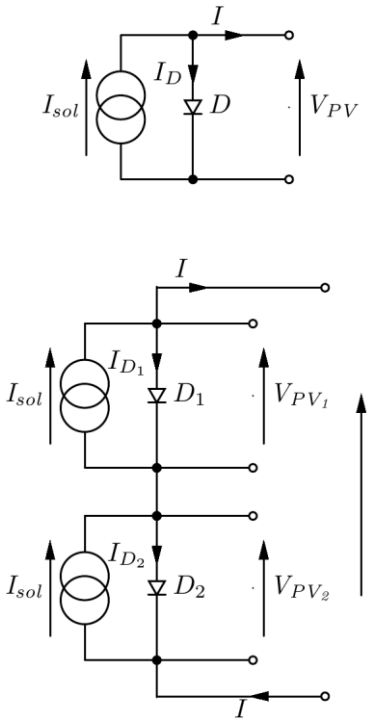

$$V_{PV} = V_T \ln\left(\frac{I_{sol} - I}{I_{sat}} + 1\right)$$

$$I_{D_1}, I_{D_2} = I_{sol} - I$$

$$V_{PV_1} = V_T \ln\left(\frac{I_{sol} - I}{I_{sat}} + 1\right)$$

$$V_{PV_2} = V_T \ln\left(\frac{I_{sol} - I}{I_{sat}} + 1\right)$$

$$V_{PV} = 2V_T \ln\left(\frac{I_{sol} - I}{I_{sat}} + 1\right)$$

Figure 2-5: Extension of a single cell to a dual cell module (under uniform irradiation). The individual diode voltage drops are added linearly such that the module voltage is double the cell voltage. The series current is the same in each cell. It is assumed that the diode parameters are equal for each cell.

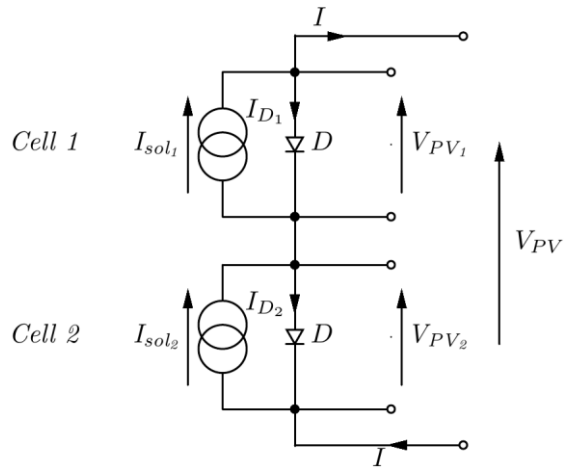

$$I_{D_1} = I_{sol_1} - I$$

$$I_{D_2} = I_{sol_2} - I$$

$$V_{PV_1} = V_T \ln\left(\frac{I_{sol_1} - I}{I_{sat}} + 1\right)$$

$$V_{PV_2} = V_T \ln\left(\frac{I_{sol_2} - I}{I_{sat}} + 1\right)$$

$$V_{PV} = V_T \left(\ln\left(\frac{I_{sol_1} - I}{I_{sat}} + 1\right) + \ln\left(\frac{I_{sol_2} - I}{I_{sat}} + 1\right)\right)$$

Figure 2-6: A dual cell module with non-uniform irradiation causing a variation in insolation current. In this case, the module voltage is affected by the irradiation in both cells.

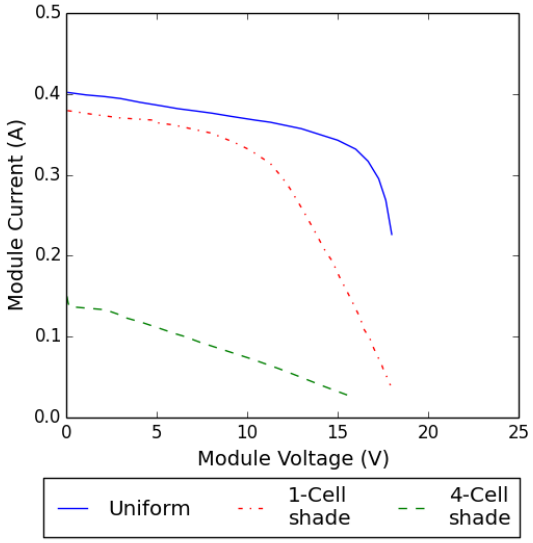

Figure 2-7: Three PV voltage-current characteristics for a uniform and two partially shaded events. The partial shading events shown are for 1-cell and 4-cells shaded respectively, within a series-connected module of 36 cells under identical ambient conditions in each case.

Furthermore, the presence of multiple maxima during partial shading will cause many problems for linear search based MPPT techniques [17], [21], [22]. The local maxima often cause false indication of maximum power point (MPP) which can lead to further degradation of power availability.

The partial shading phenomenon has resulted in extensive study in literature. The effect is often partially mitigated with the inclusion of reverse-parallel diodes[17], this is indicated in Figure 2-8.

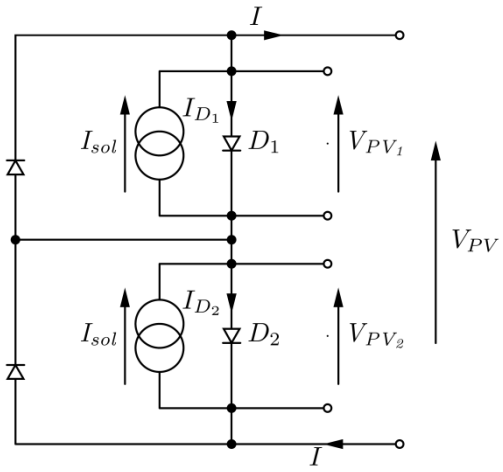

Figure 2-8: A 2-cell example of the application of reverse-parallel diodes to mitigate partial shading problems.

A common approximation to the standard model for PV characteristics is the use of an incremental conductance approximation at a standard operating condition; a Thévenin or a Norton equivalent circuit. These equivalent circuits are common for use in this kind of characterisation because of their simplicity and the limited number of calculations needed for an analysis of their dynamic behaviour. However, because the incremental conductance is calculated from a tangent to the curve at a specific operating point, the range of voltage and current over which the models hold accuracy is limited. These kinds of approximations are only suitable for small signal analyses such as the stability analysis of a power converter connected to the modules.

The incremental conductance is calculated as the derivative of the cell current with respect to the cell voltage. The basic Shockley equation based model is expressed mathematically in (2-3), in (2-4) the incremental conductance slope of the PV curve is calculated for this basic model. From these equations, an expression of the operating point (large signal current and voltage) along with the incremental conductance at that point and Thévenin or Norton model can be produced [79–81]. The solution of this problem is, however, non-trivial. The equation can easily be solved in a forward fashion with knowledge of the operating point; however, the need to generate a universal solution for all values on the curve increases the problem considerably. For the majority of regions on the PV

curve, two solutions will exist, unless the problem is first constrained by the calculation of both the current and the voltage at the operating point.

$$I = I_{sol} - I_{sat}\left(e^{\frac{V_{pv}}{V_T}} - 1\right) \tag{2-3}$$

$$\frac{dI}{dV} = -\frac{I_{sat}}{V_T}e^{\frac{V_{pv}}{V_T}} \tag{2-4}$$

2.2 - Characterisation methods

2.2.1 - Static methods

Static characterisation methods are those which feature continuous PV cell illumination. This continuous illumination is required for long term testing, often where environmental factors are to be considered. Additionally some tests require longer periods of illumination than might be available due to ambient sunlight.

2.2.1.i - Comparison of illumination sources

The various illumination sources must be compared on both their suitability as an illumination source for PV applications, but also in terms of the relative measurement uncertainties they introduce. Two important factors arise from these considerations: the stability of the illumination source with time—that is, temporal stability—and more rapid variations due to power source variations and radiation emission mechanism, flicker.

Temporal stability

The temporal stability of the illumination describes the very low frequency variations of the available illumination. This low frequency variation is typically caused by long term variations of the power source or long term degradation of the light source. This effect is rarely a problem for short term tests, but can present problems if a characterisation is to be repeated. The temporal stability can be a key consideration in the selection of a light source for tests. Most equipment powered directly

from the electric mains is susceptible to variations caused by the variation of mains voltage. The variation of mains voltage is frequently in excess of 10% of nominal throughout a day, and at certain times, can traverse the whole range in only one hour.

The best solution which mitigates the problems of to mains voltage variations is to use a stabilised power source; for incandescent and halogen lamps, this can be a DC supply. It is also possible to use a stabilised AC supply; for example, modern high frequency electronic ballasts for fluorescent often perform a degree of stabilisation. In some instances, however, it is sufficient that if the AC line voltage is set before a test commences using a variable auto-transformer or similar equipment, the line voltage will be sufficiently stable for short tests, say of around thirty seconds' duration.

An artificial light source is required as the time-varying stability of natural sunlight is sufficiently poor that an accurate characterisation of a solar cell cannot be performed before the illumination level has changed. This matter is confirmed by data gathered by the *National Oceanic and Atmospheric Administration (NOAA), National Climatic Data Center* [82], which finds that the number of entirely cloudless days during which characterisation could be reliably performed using natural illumination is less than 50 per year for climates similar to Britain.

Flicker and high frequency effects

The majority of electric light sources considered in this section can be supplied by AC mains power. The use of an AC power input produces high frequency variations at multiples of the line frequency. Despite the relatively long thermal time constant of most incandescent sources, there is still a high degree of flicker due to variations in the AC power frequency. These problems are in addition to fluctuations in the mains voltage. The problem of flicker is much stronger with sources where the light emitting medium has shorter time constant, such as with gas-discharge and fluorescent lamps.

As, for the majority of cases presented here, the presence of flicker in the light source is a disadvantage since it results in variation in the output power of the PV module, which is undesirable.

A light quality factor is therefore defined as the ratio between the mean illumination intensity and the peak-peak repetitive flicker amplitude. This quality factor has been measured for a number of light sources, using a photodiode (BXP-61) biased to operate in the linear region. This arrangement produces a voltage directly proportional to the illumination incident upon it. These factors are summarised in Table 2-2.

Technology	**Flicker crest factor (peak/average)**
Fluorescent	1.148
Halogen incandescent	1.026
Standard tungsten incandescent	1.048
Sodium discharge	1.545

Table 2-2 Review of flicker crest factors for various lighting technologies

Spectral response

To reflect practical use of PV cells, the properties of light sources are considered relative to those of the sun, which they emulate. The temperature of the sun ranges from 15 MK at the core to approximately 5 800 K at the surface. Radiation from the sun is in the form of both bosonic and fermionic radiation. Fermionic radiation, consisting predominantly of high energy protons and electronics rarely penetrates the atmosphere of earth and thus has little effect on PV cells. The bosonic radiation, which consists primarily of low energy photons, does penetrate the atmosphere and is the primary source of radiation incident upon the earth. The photons are generated from phosphorescent and fluorescent interactions at the surface of the sun and have an energy distribution following that of the Plankian distribution [83], shown mathematically in (2-5). This distribution forms the classic black body radiator model, which describes the distribution of frequency, wavelength or energy of photons emitted from a perfectly radiating surface. This is shown graphically in Figure 2-9.

$$B_\nu(T) = \frac{2h\nu^3}{c^2}\frac{1}{e^{\frac{h\nu}{kT}} - 1} \tag{2-5}$$

Where:

$B_\nu(T)$	The spectral intensity at temperature, T, and wave frequency, ν
h	Plank's constant
c	The speed of light in an vacuum
ν	The wave frequency of interest ($c = \nu\lambda$) where λ is the wavelength
k	Boltzmann's constant
T	The temperature of the emitting surface

The spectrum of daylight according to the AM-1.5 [84] spectrum standard for sunlight incident on the earth surface is shown alongside the 5 800 K black body curve. 5 800 K is the standard assumed temperature of the surface of the sun [83].

A xenon flash lamp is used for some of the characterisation processes. The xenon discharge characteristic consists of both black body radiation, due to the intense heat of the gas during ionisation, and atomic spectra due to the impact ionisation process by which the discharge occurs. This characteristic is demonstrated in Figure 2-10 [83]. The illumination sources used for the characterisation process, as demonstrated, have been selected for their spectral similarity to that of natural daylight. All the spectra differ from natural daylight, because the characteristics are difficult to emulate using easily implemented sources with the required intensity.

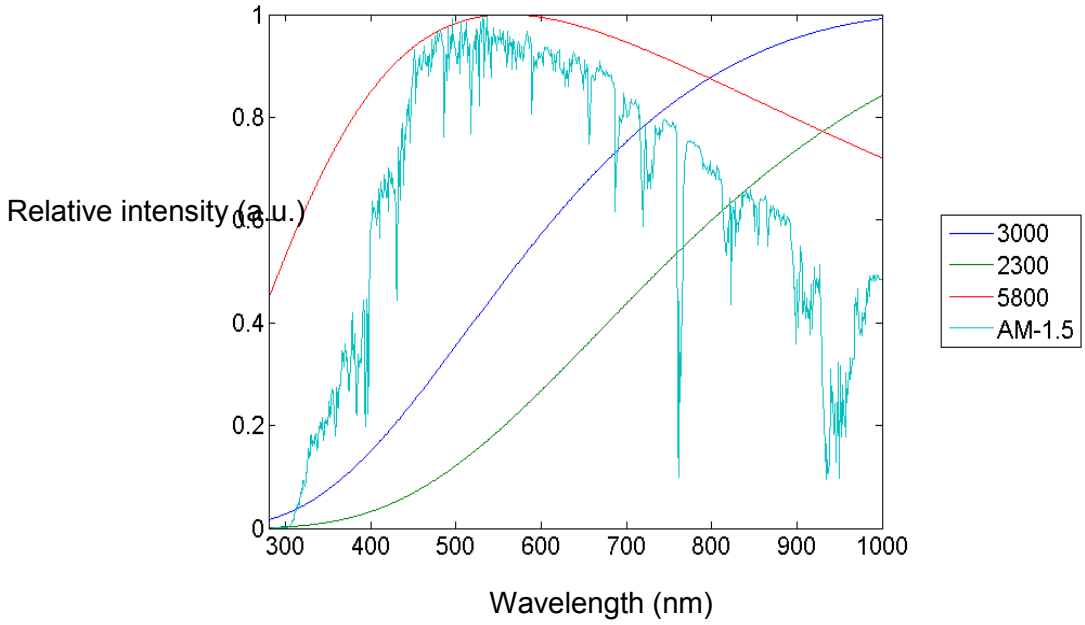

Figure 2-9: Three black body radiation curves for 3 000 K, 2 300 K and 5 800 K calculated from (2-5). Shown in addition is the AM-1.5 standard sunlight spectrum (standard curves from ASTM E927-10 standards).

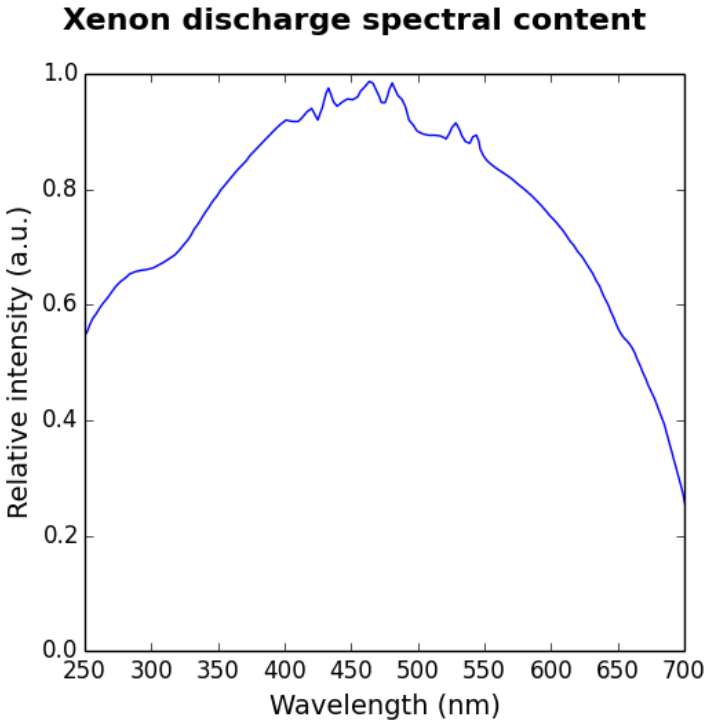

Figure 2-10: The spectral content of a high intensity xenon flash

2.2.1.ii - Load considerations

In order to develop a curve describing the voltage and current characteristics of the PV module, a variable electric load must be applied to the PV module so that the current and voltage can be varied and measured, respectively.

The most basic electric load is the resistor. Resistors are available in a wide range of resistances and power ratings. They are also low cost. However, with a PV module, a wide range of resistance and power is required. An example of the selection of resistors for power requirement and resistance has been calculated for a specific case, described in Figure 2-11. The resistors are calculated by assuming the PV module to be a constant current/constant voltage source in the two distinct regions, a square approximation. An approximation is necessary because the accurate characteristic is unknown at the time that the resistors required to generate it are chosen. It can be seen in Figure 2-11, that for a basic DC characterisation of a modest PV module, resistance ranging from 0 to 100 Ω is required. The power required for each resistance level also exhibits a wide range of variation. If the characterisation were to be performed with a single rheostat then the required power rating would be 2 W to 400 W, because at peak power occurs mid-travel for the rheostat. Whilst a truly variable resistor provides the greatest level of variation and flexibility in measurements, a sequence of discrete resistors can be used instead (Figure 2-11).

The load-line characteristic of an active load can take a number of forms. These are in general: constant current, constant voltage, constant resistance and constant power. Electronic loads are available which can act in these modes. These loads contain a mechanism which exercises the control law in each case. Such controllers are imperfect and will introduce a number of non-idealities such as finite response time between load levels, noise (additive white Gaussian) and vestigial effects of internal oscillations (which are correlated, specific frequency noise).

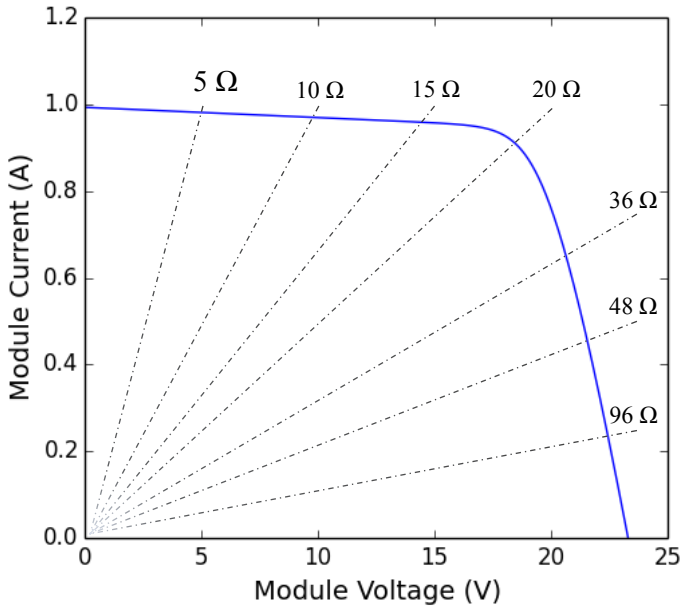

Figure 2-11: PV characteristic for calculation of resistances, the key element is the square assumption based on specified values

Recalling that the photovoltaic module can be considered to have two operating regions, the constant voltage and constant current region, it can be seen that both of these cases introduce a different requirement for the loading. Loading a PV module with a fixed voltage load in the current source operating region requires a very high degree of control in order to maintain a steady load condition. The same difficulty arises when the panel is loaded with a constant current in the constant voltage region. The solution to this problem is to either shift between constant voltage and current modes or use a constant resistance load.

2.2.2 - Dynamic illumination methods

Dynamic illumination methods can be applied to the characterisation of PV modules in a variety of ways. Of greatest industrial significance is the flashed illumination method, where a short duration pulse of high intensity light is used to deliver sufficient energy for a sufficient time that a complete sweep of the electrical characteristic can be performed. This method has been primarily adopted in the PV cell fabrication and module production industries due to the short time required and the significant

energy reduction that results from using only low duty cycle illumination (low average power but high instantaneous power) [85–87]. Dynamic methods can be extended further to those which produce a slowly varying illumination to characterise the transient behaviour of both the modules, power converters and control methods.

2.2.2.i - Short duration flash

Whilst the industrial uptake of the short duration flash based methods is due to constraints of time and energy consumption, there are benefits which can be seen from a more scientific perspective. A typical radiation pattern of a unidirectional light source is shown in Figure 2-12. When the position of the PV module is close to the illumination source, there will be a significant variation in illumination intensity across the surface of the PV module. However, at increased distance there is a much better uniformity of illumination across the module. This improved uniformity is a matter that is best exploited with flashed illumination, an 80 J flash lasting 500 μs would be equivalent to a 160 kW illumination source, at close distances this would be too bright. The greater distance and therefore uniformity in illumination is unachievable with lower power illumination.

A typical pulse is caused by a short duration flash of 80 J, delivered for 500 μs, incident upon an 80 W PV module. The load conditions are consistent with the panel exposed to approximately 2 kW/m^2 of solar radiation (approximately twice the nominal short circuit current from standard test conditions). An example waveform of the PV voltage response to flashed illumination is shown in Figure 2-13, measured using the BXP-61 photodiode as before and recorded using a DSO. Figure 2-14 shows the results of characterisation by flashed illumination, each data point is obtained using a single flash by recording the peak voltage and current, occurring at the same instant as the peak in illumination demonstrated in Figure 2-13.

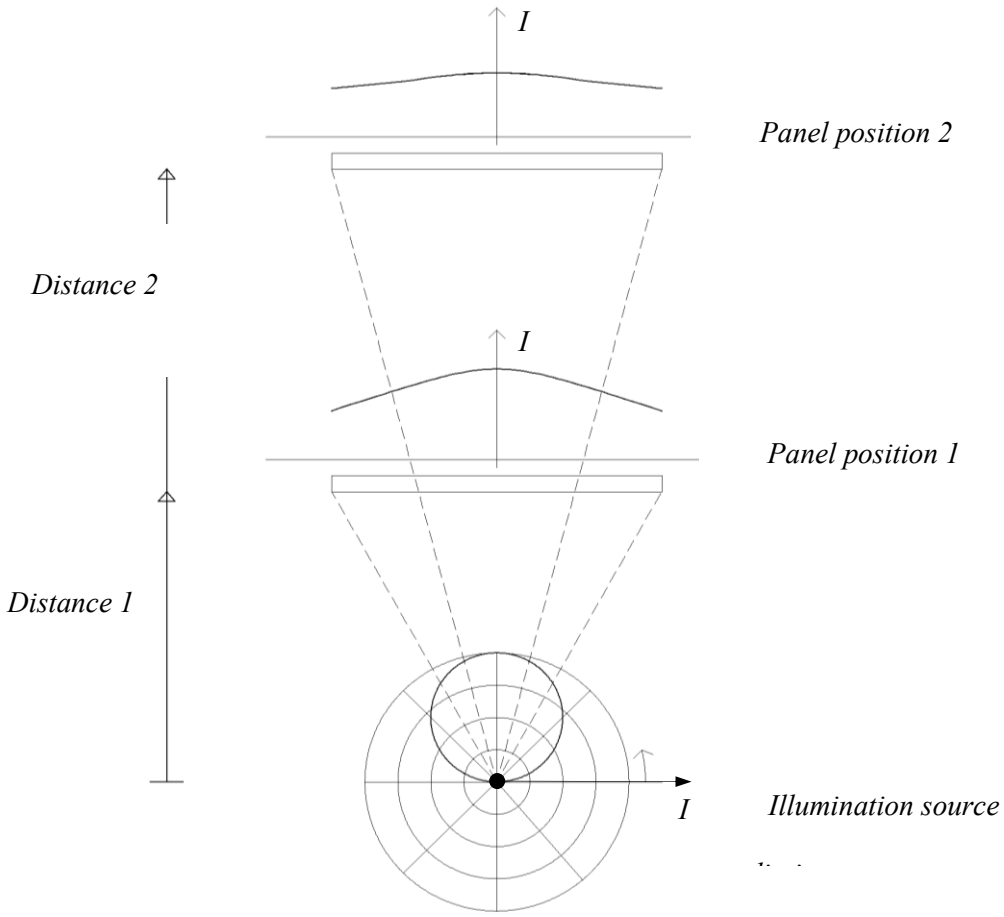

Figure 2-12: Variation of illumination pattern from a unidirectional light source, better uniformity is achieved at greater distance at the cost of decreased illumination

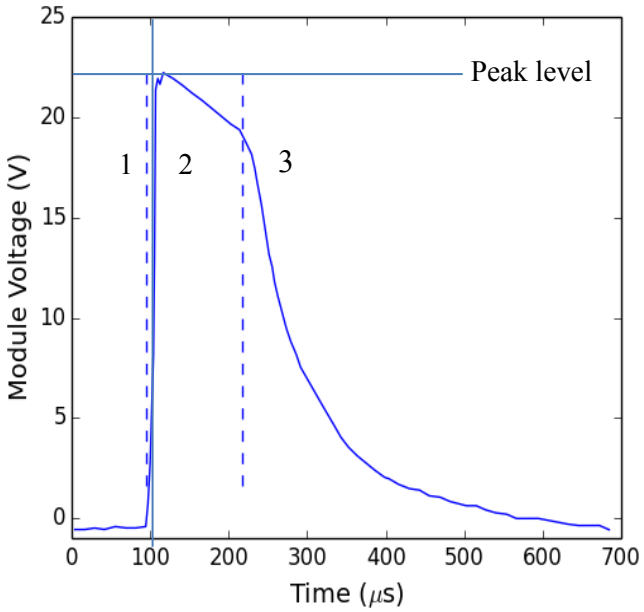

Figure 2-13 Pulse response from a PV module exposed to a high intensity flashed illumination

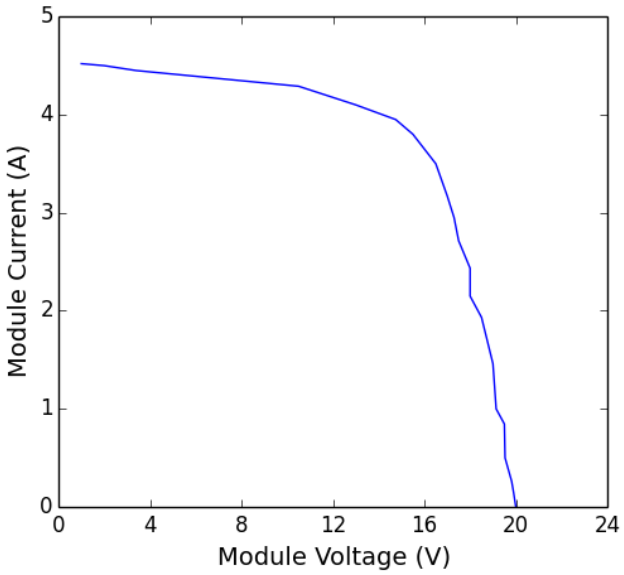

Figure 2-14: A PV voltage-current characteristic obtained for an 80 W nominal PV module using a flashed illumination technique. Some deviations from a smooth curve are apparent; these are caused by variations in the intensity of the light pulse.

Figure 2-14 and Figure 2-13 shows an example of the output voltage response following a short duration flashed illumination pulse. The response on the PV module exhibits three distinct regions, a pre-pulse region (numbered 1), a high intensity region (number 2) and a settling region (number 3). Region 1 is the period before the pulse; this region is the response of the PV module in ambient conditions. Region 2 is the period where the discharge has occurred in the flash lamp and light intensity has reached a peak. There is a linear decay that is related to the loss of energy from the main storage capacitor within the flash unit. Region 3 is the period where the primary discharge within the lamp has ceased and the PV response is a combination of the decay of charge stored in parasitic capacitances within the cells and afterglow from the ionised gas in the flash tube.

2.3 - A PV module evaluation rig

For the purposes of characterisation of PV modules and attached power converters, a PV module under controlled illumination is required. A test rig was developed for the specific requirements of this work. The rig consists of a 40 W PV module with halogen illumination. One of the goals was flexibility, so that various measurement parameters could be varied whilst maintaining the ability to reconstruct previous experimental set-ups with ease. It was decided to employ a simple method of supporting both the illumination source and PV module, on freely moveable stands to maximise flexibility in the test rig. There remains the possibility of using an electronic load, passive resistor load or arbitrary power converter as the load on the cell under test.

The layout of the evaluation rig is shown in Figure 2-15. This arrangement gives maximum flexibility to alter the illumination intensity upon the module. This experimental setup is used throughout the thesis for the experimental validation and characterisation of modules.

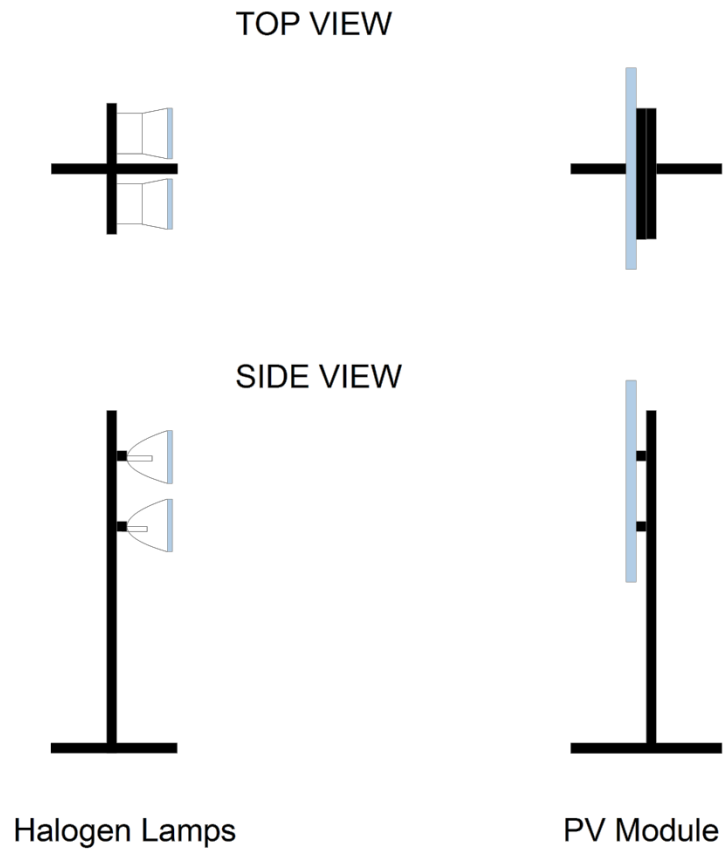

Figure 2-15: Layout of the PV characterisation rig

2.4 - Chapter Conclusions

This chapter has outlined the basic models which have been used to represent PV modules and cells in previous literature. The models presented are used extensively in the remainder of this thesis, both for the appraisal and for the optimisation of MPPT power converters. Much research has been undertaken into these models and, in general, they require very little modification to be employed for accurate results in the majority of applications. In Chapter 4 analysis will be shown which highlights the effects of some of the parasitic elements and the deviations from the simplified model with increasing frequency of current and voltage perturbations.

Characterisation methods discussed in this chapter and evaluated using both practical measurement and mathematical analysis to predict the performance and permit optimum selection of a characterisation method for a particular application. Characterisation for the purpose of the evaluation of PV modules does not require the same degree of spectral control as is required for the prediction of efficiency. However, in contrast to the direct evaluation of semiconductor materials, certain perturbations, such as flicker and poor stability, can have their own impact on the controlled evaluation of MPPT algorithms and power converters.

Chapter 3 - Design of PV solar emulator for the evaluation of MPPT algorithms

In Chapter 2, methods of extracting parameters from photovoltaic cells were examined. Chapter 2 is crucial to the development of a PV characteristic to be used in a PV emulator as discussed in this chapter. The typical design process would encompass analysis of the design in the computational domain (simulation) to verify expected operation of power converter designs and MPPT algorithms. Once evaluated by simulation, both power converters and MPPT algorithms should be practically validated against the results from simulation. As discussed in the previous chapter, PV modules under natural illumination do not provide sufficient repeatability in order to validate simulated results. To perform experiments under repeatable conditions, either a PV characteristic emulator, or an artificially illuminated PV module is required. As discussed in Chapter 2, artificial illumination setups can provide sufficient stability and repeatability but does not permit the evaluation against arbitrary PV characteristics. Arbitrary characteristics may be required when the practical system is not easily accessed for testing.

A photovoltaic characteristic emulator is fundamentally a DC power supply with a strict relationship between output voltage and current programmed, which in this case would be programmed to that of a known PV characteristic. In this chapter, a design for such an emulator is presented.

3.1 - Requirements for a PV characteristic emulator

As with any emulator, the PV characteristic emulator will not be a perfect representation of an actual PV module as its characteristics will contain discrepancies compared to an actual module. These will in turn affect its ability to provide meaningful results during the testing of a power converter or MPPT algorithm. However, the repeatability of the PV characteristic emulator, allows accurate comparison between power conversion topologies and MPPT algorithms, and is therefore very useful.

Common methods of MPPT include open-circuit voltage monitoring, short-circuit current measurement, perturb and observe techniques, and hill-climbing methods [16]. The open-circuit and short-circuit methods rely on the measurement of static parameters from the PV module, and therefore demand accurate knowledge of the maximum power point with respect to either the open-circuit voltage or short-circuit current. In comparison, the 'perturb and observe' method (derived from the hill-climbing method) is a dynamic search-based method which demands consistency between slope of the measured and emulated characteristic curves. Furthermore, it should be noted that it is not only the voltage-current characteristic but also the power-voltage and power-current curves should be considered, in the construction of an emulator system to allow meaningful testing of MPPT algorithms and hardware.

3.2 - Review of the analytical PV characteristic model

The voltage-current characteristic of a PV module is commonly represented as an equivalent circuit containing both the body diode formed by the P-N junction of the solar cell, and the parasitic elements associated with cell [13], [77]. The current generated due to illumination is modelled as a perfect current generator placed in parallel with the body diode. This model is shown schematically in Figure 2-1 and has been extensively reported in literature on the modelling of PV cells and modules. The equation which determines the behaviour of voltage and current at the terminals has been derived as (3-1) [77]. This can be used to provide both the transient (AC response) and static (DC) responses of the PV module. The parasitic capacitance (C_P in Figure 2-1) is commonly neglected for simplification purposes. C_P is dependent on a number of factors (e.g. temperature, illumination and operating current) which cannot easily be predicted for the purposes of modelling; furthermore, its low value (~100 pF) means that it only has a significant effect at very large rates of change of voltage not usually experienced during normal operation.

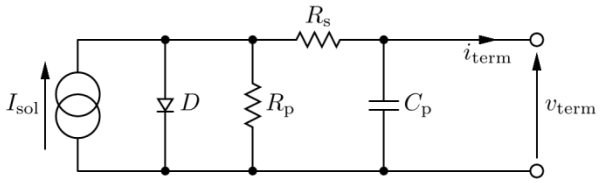

Figure 3-1: PV model equivalent circuit

$$0 = I_{sol} - I_{term} - C_p \frac{dV_{term}}{dt} - \frac{R_p}{V_{term} + R_s\left(I_{term} + C_p \frac{dV_{term}}{dt}\right)} - I_{D_{sat}} \exp\left(\left(V_{term} + R_s\left(I_{term} + C_p \frac{dV_{term}}{dt}\right)\right) \Big/ V_{D_{th}}\right) \quad (3\text{-}1)$$

Where:

I_{sol}	The current due to the illumination of the PV cell P-N junctions
C_p	The value of parasitic parallel capacitance
V_{term}	The magnitude of voltage developed at the terminals of the PV module
I_{term}	The magnitude of current flowing in the output terminals of the PV module
R_p	The value of parasitic parallel resistance
R_s	The value of parasitic series resistance
$I_{D_{sat}}$	The value of the reverse saturation current of the PV cell P-N junctions
$V_{D_{th}}$	The effective inbuilt-potential of the PV cell P-N junctions

3.3 - The emulator circuit development

The established voltage-current characteristic obtained as per the process described in Chapter 2 can be used to determine the topology of circuit used to perform the emulation.

3.3.1 - The output stage

In this section, candidate output stages which could be used to drive the output power to the circuit under test are considered. The potential output stages fall into two board categories: linear and switched mode. The switched mode output stages category encompasses any method by which the final signal is modulated to a dual-state (on/off) pulse train (e.g. PWM, delta-sigma modulation etc.)

which is then applied to a hard-driven switch operating conditions of greater current and/or voltage. In contrast, the linear category encompasses all output stages where output devices operate in a region other than hard-on or hard-off; however, in the linear operating area there are large losses in the switches which may lead to high power dissipation, and the need for heat-sinking

In most conventional switch-mode output stages, there is a residue ripple from imperfect filtering of the hard switched (square) waveforms. This 'ripple' in the output waveform can be filtered to low levels; however, the filtering is at the cost of system speed. Switched mode power converters used extensively for MPPT. These power converters, used on an emulator, would introduce a large ripple current. These effects would both interfere with the output stage control and be interfered with by ripple from the output stage. This matter would be undesired for the evaluation of such power converter ripple in the MPPT converter. For these reasons it was decided that the output driver of this emulator be of a linear (non-switched-mode) type.

3.3.2 - The VI controller- topologies

The use of digital control algorithms have been steadily increasing in popularity over the years since the production of microcontrollers to the point that the resulting flexibility of software reprogrammable algorithms have become an advantage over traditional analogue processing techniques [60].

One of the fundamental steps in the design of a digital control algorithm is to determine the required sampling rate and computational requirements. The sampling rate is commonly considered acceptable when it is an order of magnitude greater than the maximum frequency of fluctuations to be controlled, and at least twice that of the maximum frequency of any signal present (be that in the form of noise or any other form) [88]. The emulator will be used to examine MPPT systems based on switched mode power converter technologies operating at switching frequencies in the range between 20 kHz (typical minimum, being just above the range of human hearing) and 400 kHz. The maximum frequency of interest now determines the update rate of the controller, this places constraints on both

the sampling rate of the analogue to digital converter and controller processing rate. The required update rate will therefore be in the region of 4 million-updates per second (MUPS).

Analogue to digital converter technologies offer either high update rate or high resolution. Both high sample rate and resolution can both be met at greater financial cost. However, to maintain the high update rate, and solve the required IV characteristic equation at the rate required will require a large number of iterations, which could potentially increase the required iteration rate to nearly 40 MHz. Since each iteration will itself require a number of calculations, that would push the required processing power into the realm of a high-end DSP platform (400 MHz pipelined processor or parallel FPGA based processing). This kind of processor carries with it a high cost owing to highly optimised digital hardware. The digital process itself also carries with it a number of computational errors due to truncation and rounding of stored numbers during calculations. In contrast to these problems, a greater effort can be applied in the design of an analogue system used to generate the characteristic. Analogue methodology does, however, remove the re-programmability advantage of a digital system, but gives a potentially higher bandwidth system.

Given the above arguments, the proposed solution is to employ analogue computers to perform calculations since they do not suffer from the bandwidth limitation inherent with sampled data systems in digital computers. The performance of an analogue computer typically degrades gradually as frequency and dynamic range limits are reached, as opposed to a digital system where the transition from useful to meaningless results is abrupt. The fundamental variations are indicated by Figure 3-2. Because of this, the emulator was based on an analogue computation method.

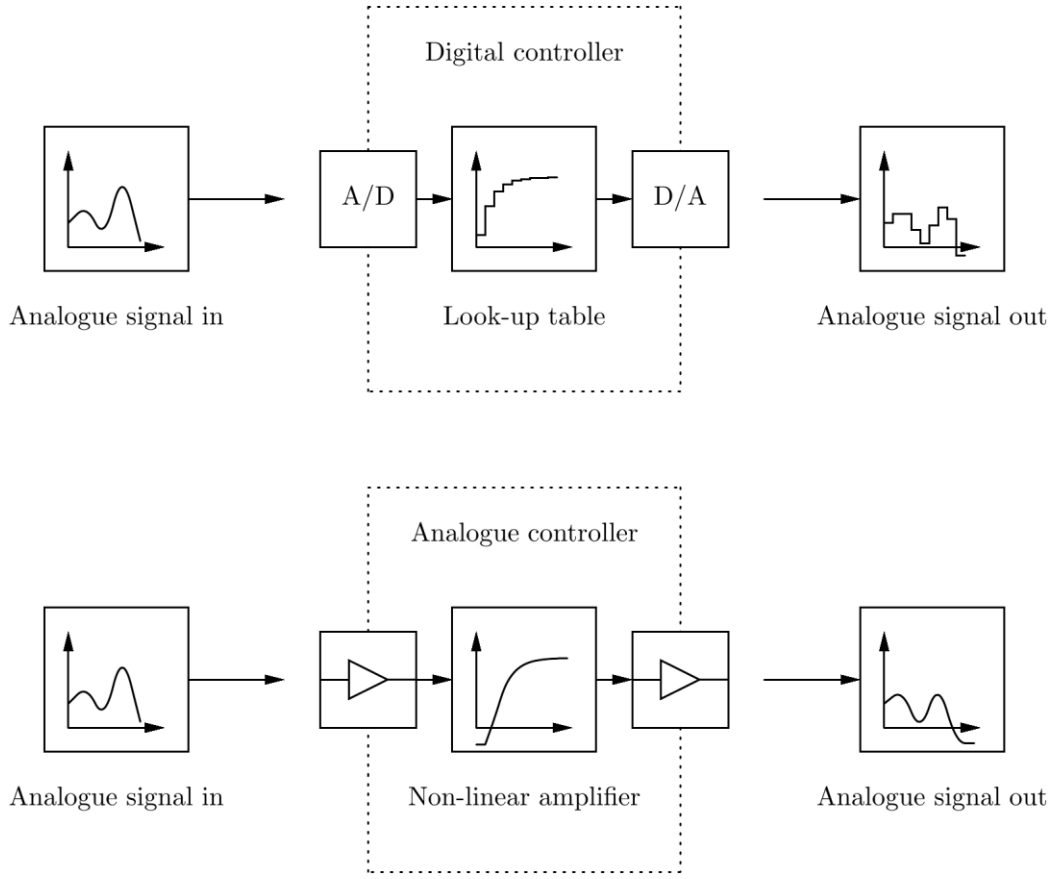

Figure 3-2: Digital and analogue controller comparison

3.3.3 - The VI controller, based on an analogue computer

Analogue computational methods have been used extensively where the equivalent digital system has failed to meet the requirements of speed or noise [63], [66], [67]. The popularity of analogue computer methods has declined significantly with the advent of modern digital computers and improved numerical solutions for differential equations. The original popularity of the analogue computer evolved from the ability of the operational amplifier to perform mathematical calculus functions such as integration and differentiation and the ease with which they could be scaled hierarchically to describe a complex physical system [66]. As such, the design of analogue computer systems is widespread in literature; however, there is little mention of the design of analogue computer systems for non-linear ordinary functions, such as the PV IV characteristic. This section therefore

presents a method employed for the design of the analogue computer solution for the IV controller in the PV emulator.

The intention of the emulator is to provide a repeatable means for assessing the performance of MPPT converters and their control algorithms. In this work, it is the generic behaviour of the system that is of interest rather than emulating the response obtained from a specific PV module. Therefore, to ease the development of the emulator, equation (3-1) is simplified by neglecting the direct effects of the parasitic series and parallel resistances and also the parallel parasitic capacitance previously discussed. The effects of these components will be assumed negligible and will be matched by comparison of the final circuit components with the characteristic obtained directly from the PV module. Removing the contributions leads to the following simplified model:

$$0 = I_{sol} - \frac{V_{term}}{R_p} - I_{D_{sat}} e^{\frac{V_{term}}{V_{D_{th}}}} \tag{3-2}$$

Where the symbols have the same meaning as in (3-1)

This equation, however simplified, still contains an exponential term which is in general not desirable in a circuit containing feedback. The exponential function has an incremental voltage gain which increases with operating point and will cause unwanted amplification of noise, and therefore requires feedback compensation which would make the circuit unable to operate at a bandwidth greater than the equivalent digital system. Equation (3-2) is therefore rearranged to its logarithmic equivalent as shown in (3-3).

$$V_{term} = V_{D_{th}} \log_e \left(\frac{I_{sol} - I_{term}}{I_{D_{sat}}} + 1 \right) \tag{3-3}$$

Where the symbols have the same meaning as in (3-1)

Now, equation (3-3) can therefore be represented using commonly available mathematical functions implemented with analogue circuits, more specifically implemented with operational-amplifiers. The system architecture approach is shown in Figure 3-3 where the terms contained within

log function brackets are first developed followed by the logarithmic function itself. The system was found to be stable by empirical evaluation and simulation.

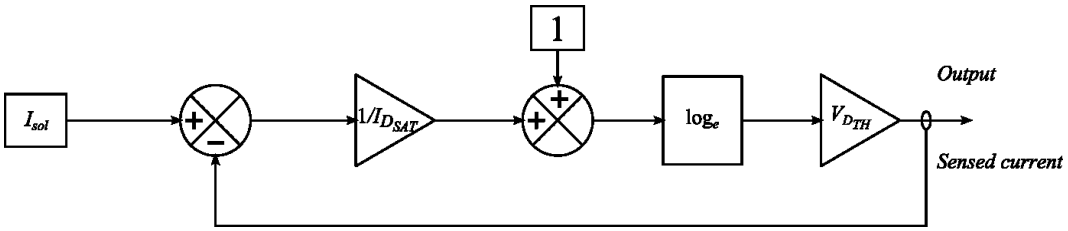

Figure 3-3: The proposed topology to solve the PV-characteristic equation

This topology was then implemented by employing commonly used operational amplifier circuit topologies which perform the required mathematical functions. The electronic schematic of the proposed solution is shown in Figure 3-4. The functions performed by the operational amplifier circuits are as described in Table 3-1. Further important considerations must be taken into account with the presence of the current sense resistor which is on the 'low-side' and is therefore in series with the output. The presence of the current sense resistor must generate a negligible voltage drop compared to the output voltage.

Operational amplifier	**Function**	**Assumptions for analysis**
A1	Differencing amplifier	Ideal amplifier
A2	Logarithmic amplifier	Ideal amplifier, no all diode considerations taken into account
A3	Precision half-wave rectifier	Ideal amplifier, ideal diodes
A4	Power amplifier	Ideal amplifier

Table 3-1: Operational amplifier function for the circuit shown in Figure 3-4.

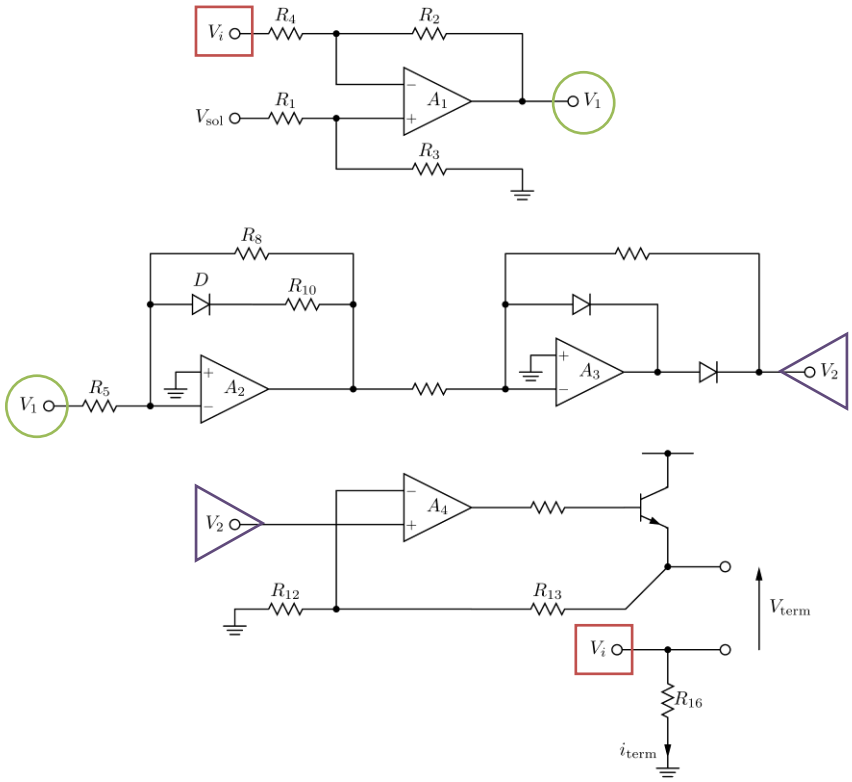

Figure 3-4: The electronic schematic representing the proposed analogue computer, the voltage signal representing illumination is shown as V_{sol}.

Using conventional analysis techniques, a model for the emulator can be derived allowing the circuit elements and quantities to be equated to PV module characteristics. Assuming the operational amplifiers (A1, A2, A3 and A4) are all ideal the circuit behaviour equation is shown in (3-4). The term, V_{sol} is introduced in Figure 3-4 as an arbitrary voltage signal proportional to module illumination, for simplicity it has been set at 2.5 V and is related to I_{sol} via the non-inverting gain of amplifier A_1.

$$0 = V_{D_T} \log_e \left(\frac{(G_1 V_{sol} - G_2 V_i)}{I_{D_{sat}}} + V_o \alpha_2 + 1 \right) + R_{10}(G_1 V_{sol} - G_2 V_i) + \alpha_1 V_o \quad (3\text{-}4)$$

Where:

R_x	is the corresponding resistor, $R_{1,2,3\ldots}$, in Figure 3-4
V_{D_T}	is the thermal voltage of the diode associated with the logarithmic amplifier in Figure 3-4
V_o	is the voltage developed at the output terminals of the emulator
V_i	is the voltage developed over the current sense resistor, $V_i = I_{term} R_{16}$, where I_{term} is the current flowing at the output terminals of the emulator, and
V_{sol}	is a voltage representing the illumination of the module
G_1, G_2, α_1, α_2	are lumped constants factored for simplicity, these are described in (3-5)

$$\left.\begin{aligned} G_1 &= \frac{R_3}{R_4 R_5}\left(\frac{R_4 + R_2}{R_1 + R_3}\right) \\ G_2 &= \frac{R_2}{R_4 R_5} \\ \alpha_1 &= \frac{R_{10}}{R_5} - 1 \\ \alpha_2 &= \frac{1}{R_8 I_{D_{sat}}} \end{aligned}\right\} \quad (3\text{-}5)$$

Where:

R_x	is the corresponding resistor, $R_{1,2,3\ldots}$, in Figure 3-4
$I_{\mathrm{D_{sat}}}$	Is the reverse saturation current on the diode associated with A2 in Figure 3-4

3.4 - Matching the emulator response to a given characteristic

Given that the purpose of the PV emulator is to replicate a given PV module characteristic (as opposed to one defined by model parameters), the next stage in the development of the PV emulator is to determine a method by which the component values can be selected to give a desired response. In this section a curve fitting methodology is described to obtain the emulator circuit component values by minimising the error between the predicted emulator response and the PV module experimental characteristic. The equation determining the output behaviour of the PV is both implicit and transcendental, and therefore no exact analytical solution to the equation exists, because given the large number of variables to be solved for this, it would also be prohibitively complex.

The equation of (3-4) is now of a similar form to (3-6), which is an expression for the error between the measured voltage and the voltage calculated from measured current for a single point on an IV curve. This kind of expression is used either to calculate the fitness of measured data to a known function or to evaluate the acuity of the function based on measured data.

$$V(I_n) - V_n \tag{3-6}$$

Where:

$V(I_n)$ is the function describing the relationship between $I_n$and V_n

$I_n$and V_n are measured data

The four isolated lumped constants in (3-4) (G_1, G_2, α_1, α_2) uniquely define the twelve variables, with the exception of $I_{D_{sat}}$& V_{D_T} which are determined by the characteristics of the diode in the circuit. A least squares approach will be used to form the cost function for later optimisation, as follows. Measurement noise terms have been minimised during the practical measurement stages and are therefore not included in the lead squares formulation.

$$\begin{aligned} &X\left(\langle V_{i_n}, V_{o_n}\rangle, G_1, G_2, \alpha_1, \alpha_2, V_{sol}, R_{10}\right) = \\ &= \sum_{n=1}^{N} \left[V_{D_T} \log_e \left(\frac{\left(G_1 V_{sol} - G_2 V_{i_n}\right)}{I_{D_{sat}}} + V_{o_n}\alpha_2 + 1 \right) + R_{10}\left(G_1 V_{sol} - G_2 V_{i_n}\right) \right. \\ &\qquad \left. + \alpha_1 V_{o_n} \right]^2 \end{aligned} \tag{3-7}$$

Where the variables have the same meaning as defined in (3-4) with V_{i_n} and V_{o_n} expanded for the case of N 2-tuples of data to form the curve to fit the equation to. X(…) is the cost function to be minimised

For the purpose of using a curve fitting algorithm to obtain values for the defined parameters in (3-5), numerical bounds must be defined to ensure only useable values are obtained. These are defined in (3-8) based on physical and practical constraints. Many minimisation methods do not intrinsically accept bounded parameters (those with a range of acceptable values). In this case, for simplicity they have been implemented as an additive quadratic penalty function. The generalised form of the penalty function applied is shown in (3-9), as the parameter drifts beyond its permitted boundary, the penalty function increases the value.

$$\begin{array}{ll} \{ & G_1 \in \mathbb{R}: \quad 0 \leq G_1 < \infty \quad \} \\ \{ & G_2 \in \mathbb{R}: \quad 0 \leq G_2 < \infty \quad \} \\ \{ & \alpha_1 \in \mathbb{R}: \quad -1 \leq \alpha_1 < \infty \quad \} \\ \{ & \alpha_2 \in \mathbb{R}: \quad 0 \leq \alpha_2 < \infty \quad \} \end{array} \tag{3-8}$$

Where: the symbols have the meanings previously defined in (3-5)

$$c(P) = \begin{cases} (P - P_l)^2, & P \leq P_l \\ (P - P_u)^2, & P \geq P_u \\ 0, & P_l \leq P \leq P_u \end{cases} \tag{3-9}$$

Where:

P_l is the lower bound of parameter P

P_u is the upper bound of parameter P

The resulting minimisation function then becomes:

$$\min\{X(\langle V_{i_n}, V_{o_n}\rangle, G_1, G_2, \alpha_1, \alpha_2, V_{sol}, R_{10}) + c(G_1, G_2, \alpha_1, \alpha_2, V_{sol}, R_{10})\} \tag{3-10}$$

Where:

$c(\dots)$ is the penalty function applied for the parameters

$X(\dots)$ is the original function to be minimised

The equation which defines the relationship between the voltage and current at the output terminals of the emulator can now be solved using a curve fitting routine. For this purpose, the 'Simplex method of Nelder and Mead' was used. The Nelder-Mead algorithm has frequently been used in literature and has implementations in many engineering mathematics software packages. The application of soft constraints as demonstrated in (3-9) requires the use of a non-gradient method. The Nelder-Mead algorithm has a wide area of convergence, which in this application is more important than its slow convergence rate.

Initial trials of the method were performed using synthetic measurement data from a simplistic PV characteristic generated by equation (3-11). The use of calculated data gives an initial certainty that the data is of acceptable quality for the curve fitting routine.

$$V_{term} = 2.5 \log\left(\frac{10 - I_{term}}{0.0001} + 1\right) \tag{3-11}$$

Trials of the solving algorithm initially showed a significant degree of competition between the variables and a general trend for the parameters to be 'saturated' at their limits, indicating that a solution for the configuration was unobtainable with any degree of repeatability or confidence. This matter was investigated by solving for the remaining parameters with a single parameter fixed over a range. The results of these investigations are shown in Figure 3-5 and Figure 3-6 which clearly show where the solution deviates significantly from the dominant trend in the data. This problem is undetectable without a-posteriori knowledge of the system as the error term does not fluctuate under this effect.

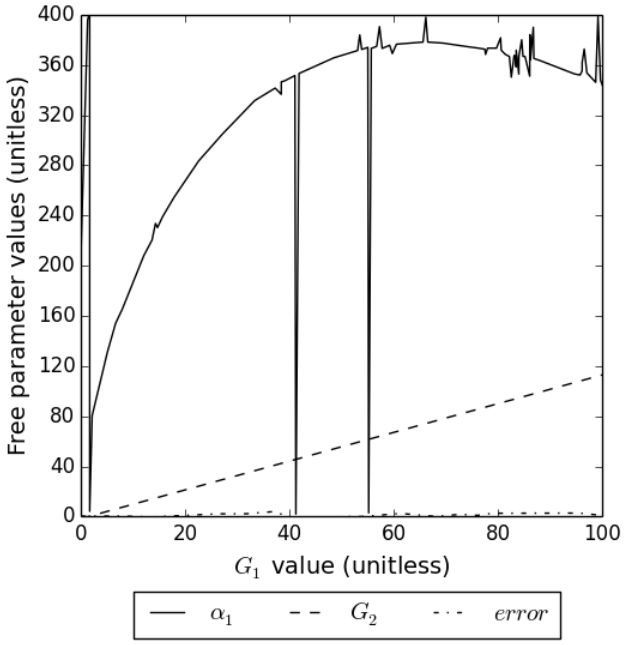

Figure 3-5: Parameter search results with G_1 swept - $V_{term} = 2.5 \log\left(\frac{10 - I_{term}}{0.0001} + 1\right)$ used as equation to match

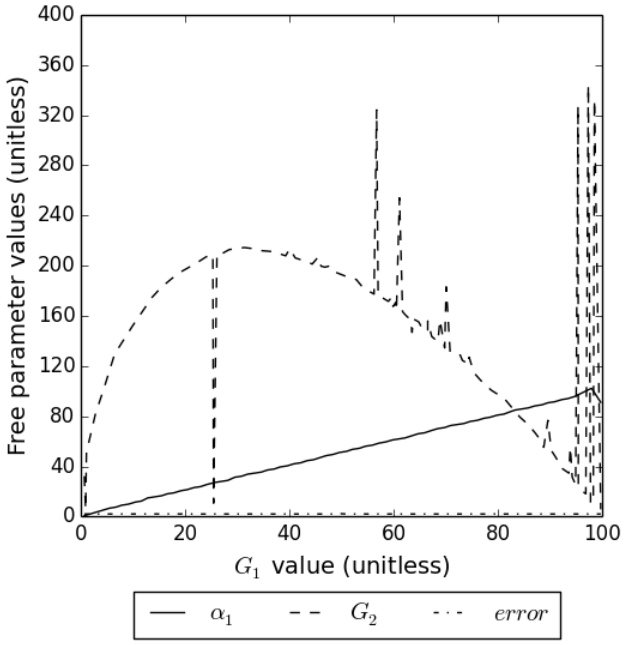

Figure 3-6: Parameter search results with G_1 swept; $V_{term} = 2.5 \log\left(\frac{5-I_{term}}{0.0001} + 1\right)$ used as equation to match

Noting that in Figure 3-5 and Figure 3-6, the parameter G_2 appears to be directly proportional to parameter G_1 and is unaffected by the apparent noise, its gradient was noted as being consistently equal to $\frac{V_{sol}}{I_{sol}}$ (I_{sol} being extrapolated by the supplied model data as the point where the voltage of the module falls to zero). With a parameter relationship implemented such that $G_1 = \frac{V_{sol}}{I_{sol}}$, the problems ceased, the results of similar parameter sweeps are shown in Figure 3-7 and Figure 3-8. It can be seen that there is significant improvement in the numerical stability by setting the parameter relationship as was obtained through inspection: there are no significant deviations from the general trend of the data points.

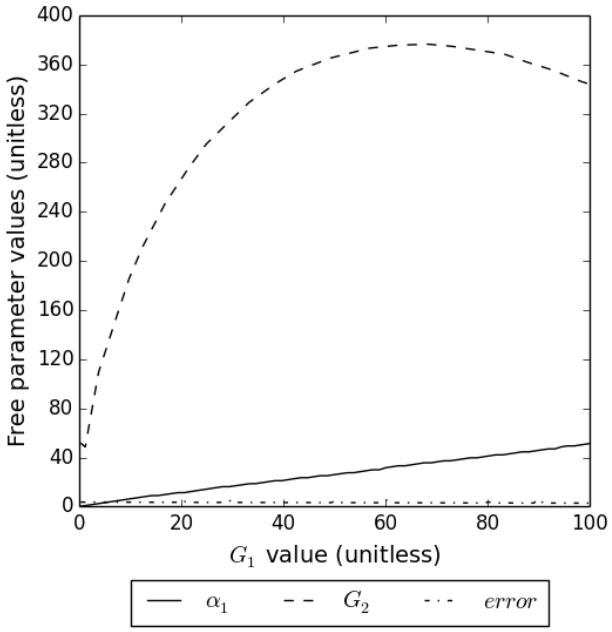

Figure 3-7: Parameter search results with G_1 swept - $V_{term} = 2.5 \log\left(\frac{10 - I_{term}}{0.0001} + 1\right)$ used as equation to match. A parameter relationship of $G_1 = \frac{V_{sol}}{I_{sol}}$ is defined.

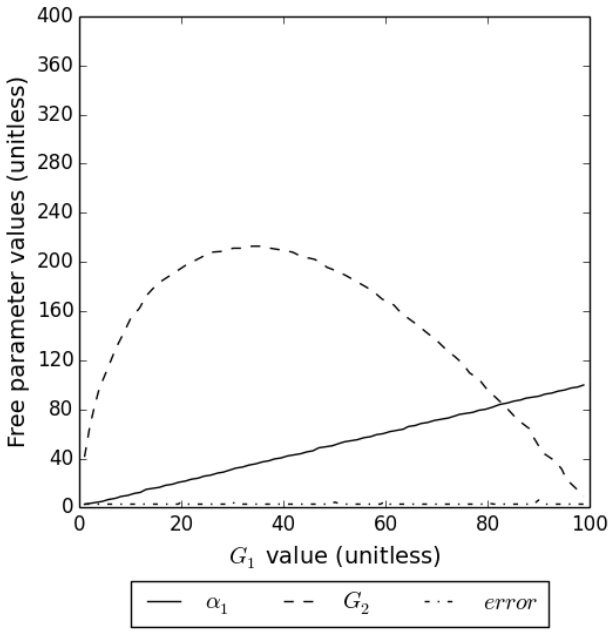

Figure 3-8: Parameter search results with G_1 swept - $V_{term} = 2.5 \log\left(\frac{5 - I_{term}}{0.0001} + 1\right)$ used as equation to match. A parameter relationship of $G_1 = \frac{V_{sol}}{I_{sol}}$ is defined.

3.5 - Determining emulator component values from a PV module characteristic

The presented circuit component calculation technique has so far only been demonstrated with an analytical model used to calculate the characteristic to be matched. Whilst this method remains valid in testing the ability of the algorithms to calculate the component values for the emulator; the system must also be tested for its ability to replicate a true PV module characteristic.

Data was collected from a nominally 12 W polycrystalline-silicon module. A variable resistance was used as load and illumination was provided by a high intensity flash as previously discussed. Twenty data points were collected over the range from open circuit to short circuit. The data was then used to determine the component values for the emulator. Practical results from the emulator are shown with the original data in Figure 3-9 and Figure 3-10.

3.5.1 - Calculated components

The diode element in the logarithmic amplifier was constructed from a serial chain of 10 1N4148 small-signal silicon diodes. By constructing a diode from a string of 10, reverse leakage is decreased and requirements for voltage amplification are reduced. The equivalent I_s and V_T of the diode string is determined from a voltage-current plot and fed into the component calculation algorithm. This string of 1N4148 diodes was found to have and I_s of 50 nA and V_T of 30 mV.

The op-amps used were Burr-Brown OPA445 devices which have a 90 V rail-to-rail supply voltage; the high supply voltage reduces the total number of power supply rails required for the circuit.

The lumped parameter values and the resulting calculated component values are shown in Table 3-2 and Table 3-3 respectively.

Parameter	Value
G_1	8.99×10^{-5}
G_2	9.10×10^{-5}
α_1	-0.90
α_2	74.10
V_{sol}	2.5
R_{10}	10 Ω

Table 3-2: The parameter values calculated for the emulator lumped parameters.

Component	Value
R_1	270 kΩ
R_2	270 kΩ
R_3	11 kΩ
R_4	11 kΩ
R_5	11 kΩ
R_{10}	10
R_8	270

Table 3-3: Calculated componants from the parameter values shown in Table 3-2

3.6 - Results

Figure 3-9 and Figure 3-10 show the results collected from the practical emulator once matched to the experimentally obtained PV module characteristic: real data from the PV module is denoted ‘real’ and data measured from the emulator is denoted as ‘emulator’.

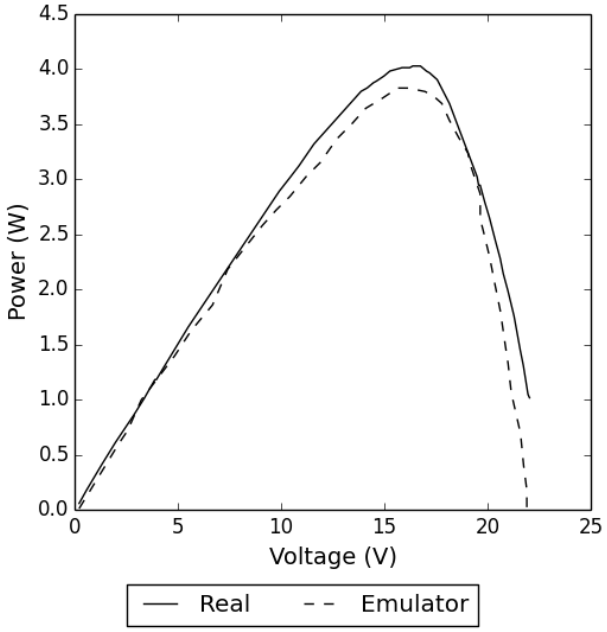

Figure 3-9: Voltage-power curves for the both original characteristic data and that obtained from the matched emulator

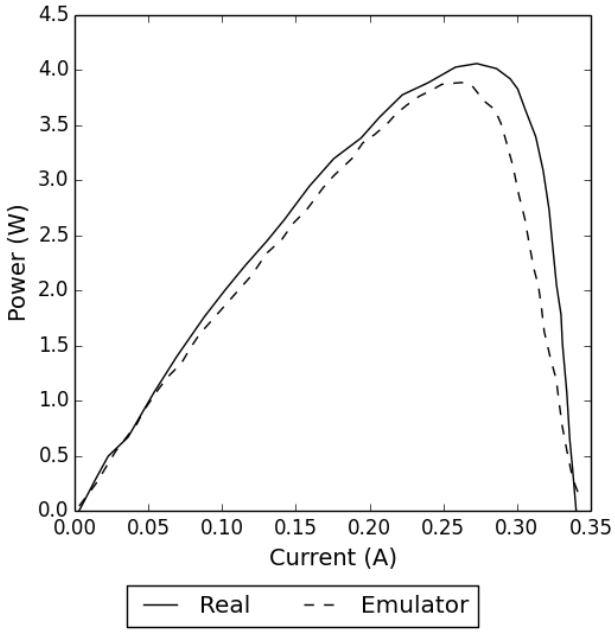

Figure 3-10: Current-power curves for the both original characteristic data and that obtained from the matched emulator

Both Figure 3-9 and Figure 3-10 show good agreement. In Figure 3-9 it is apparent that the location of the maximum power point is accurately matched, whereas in Figure 3-10 there is a 2.5% error in the current at which the maximum power point occurs. The location of the maximum power point is therefore within acceptable uncertainty for evaluation of the O/C and S/C MPPT methods previously described. The shape of both current-power and voltage-power also show good agreement: there are no local minima or maxima which would cause dynamic search-based algorithms, for example the 'perturb and observe' algorithm, to falsely indicate maximum power has been reached.

The proposed design is therefore seen to be and accurate PV module emulator.

3.7 - Chapter conclusions

This chapter has been concerned with the development of a PV module characteristic emulator. The merits of digital and analogue computing methods to perform the required tasks have been compared and contrasted justifying the final decision that the system be based on an analogue computer. The method used to design the practical circuit has been presented along with the necessary assumptions made. A practical method to determine required circuit values in order to programme a characteristic in to the emulator has also been shown along with various modifications to a 'straight-forward' approach which tailor the equation to be solved accurately by applying techniques (both analytically and by inspection) to reduce the number of parameters which must be solved for. Results have also been presented which indicate that the emulator mimics the PV-module characteristic with sufficient accuracy such that a range of MPPT algorithms can be evaluated.

In later chapters the emulator will be used to provide a stable platform for power converter testing.

Chapter 4 - Effects of power converter induced current ripple on PV module output power

Modern photovoltaic (PV) power generation systems demand the use of maximum power point tracking (MPPT) control algorithms that can only be efficiently implemented using switched mode power conversion techniques. The operation of switched mode power converters, in particular, hard switched converters, produces a significant ripple current due to both finite inductance and finite switching frequency within the converter. Control algorithms also impose a much lower frequency ripple current on the output of the power converter. This chapter is concerned with the effect of the generic switching frequency ripple produced within the power converter, and its effect on the operational efficiency of the PV generation system. This effect occurs regardless of additional current ripple caused by maximum power point tracking, controller instability and line frequency effects (in grid connected inverter systems), and is generic to the operation of the switched mode power converter in the MPPT system.

4.1 - Definition of transfer efficiency

A typical PV power system will consist of a number of individual components. Firstly, a primary source of power. In this case it is the electromagnetic radiation in the near-visible spectrum termed insolation. This insolation in incident upon the primary power conversion mechanism: the PV module. The module itself consists not only of PV cells, also a transparent layer, commonly made from glass, providing physical protection for the cells. A quantity of this insolation will be reflected or absorbed by this protective layer. The transmitted fraction of insolation (i.e. neither absorbed nor reflected) is then incident upon the PV cells. The insolation incident upon the PV cells is then subject to various mechanisms of loss within the silicon structure, and the fraction of the incident radiation flux which successfully converts to electrical power at the semiconductor junction of the PV cell is often termed the quantum efficiency.

For steady-state ambient conditions and incident insolation upon the module, power is generated at a fixed rate. For a fixed radiation flux (fluence of electromagnetic-quanta), an equivalent number of electrons are liberated in the semiconductor junction and produce a voltage difference at the electrical interconnects to the cells. This gives the potential to drive current in an external circuit. As discussed in Chapter 2, the voltage generated at each cell is largely dependent on the resistance of the external circuit. With a cell terminated with infinite impedance, the current generated by the insolation flows only within the internal circuit, which consists of a combination of bulk resistances and semiconductor junction diode itself. In this case, *power is generated but none is transferred to the external circuit*. A cell terminated by an impedance of zero suffers from the opposite effect that all current flows in the external circuit causing zero voltage at the terminal; thus, zero power is similarly transferred to the external circuit.

Transfer efficiency is thus defined here the fraction of power transferred to an arbitrary external circuit to that which could be delivered under ideal electrical conditions (i.e. those of perfect MPPT).

A reduction of transfer efficiency can be demonstrated to be apparent under a number of circumstances, most notably under conditions of imperfect MPPT and under a deviation from DC MPPT conditions. Conditions of DC MPPT and transfer efficiency are demonstrated in Figure 4-1 and Figure 4-2. The case of deviation from this DC case is shown in the remainder of the chapter. This analysis is not a solution for the optimisation of the entire system but specifically of the power converter and its effects. It is assumed that any external effects due to variation of illumination are sufficiently slow compared with any electrical variations and that a MPPT algorithm can track changes sufficiently quickly. Transfer efficiency can be represented mathematically as in (4-1).

$$\eta_{transfer} = \frac{P_i}{P_{MPP}} \tag{4-1}$$

Where:

$\eta_{transfer}$	is transfer efficiency
P_i	is the instantaneous or average input power to the external circuit
P_{MPP}.	is the power delivered by the PV module under MPP conditions

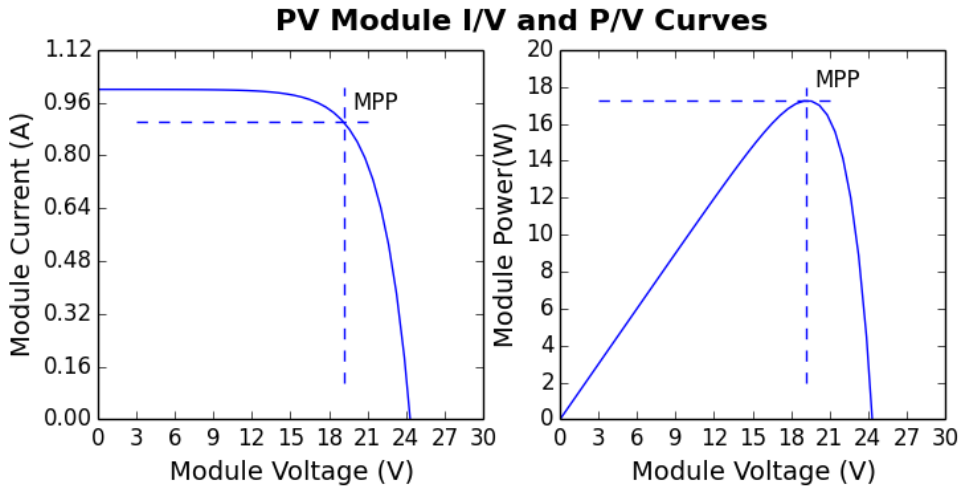

Figure 4-1: Typical PV module electrical characteristics shown in terms of both output current and power with respect to varying terminal voltage. Curves are shown for a constant I_{sol} = 1 A.

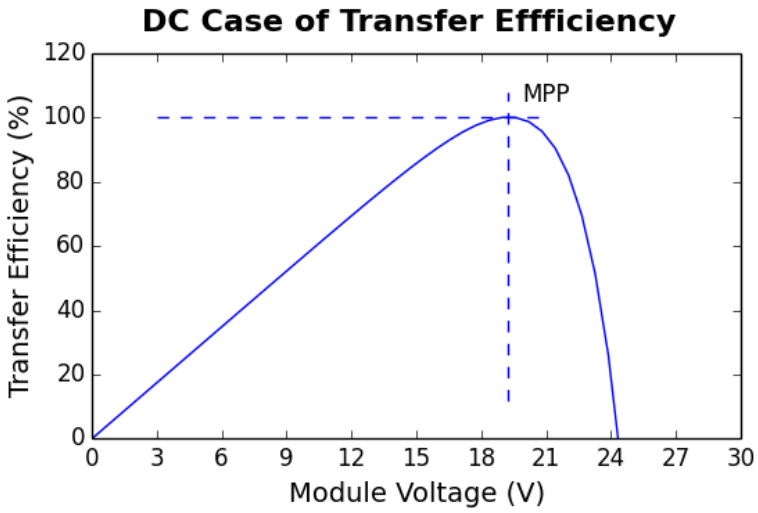

Figure 4-2: A graph showing the power response of a PV module with respect to varying terminal voltage. The graph has been scaled in terms of transfer efficiency, defined as the ratio of extract power to that at MPP. Curves are shown for a constant I_{sol} = 1 A.

4.2 - Theoretical analysis

The transfer efficiency is considered to be the ratio of the actual electrical power extracted from the PV module as a fraction of the power at maximum power point condition of the PV module. This only considers the condition where the voltage and current seen by the PV module are pure DC, whereas in reality due to the switching nature of the power converter there will be a significant ripple imposed on them. To address this problem, the response of the PV module under conditions of significant current ripple imposed on the DC conditions is now considered.

4.2.1 - Modelling a SMPC

In order to predict the behaviour of a PV module to varying current drawn, a mathematical model of the current drawn by a typical SMPC is required.

The selection of a SMPC for PV applications can be characterised by requirements for boost/buck performance and isolation requirements. A typical PV installation layout is shown in Figure 4-3. An intermediate DC bus exists in between the frontend power converter and downstream modules. The front-end power converter must primarily perform the voltage transformation from the PV module to the intermediate bus whilst providing MPPT functionality. Galvanic isolation must, in most circumstances, be provided somewhere in the system for protection of equipment and reduction of radiated noise. Isolation is not, however, a direct requirement in the front end power converter performing the MPPT. Typically, in mains connected power supplies, the front end (the active power factor correction stage) is un-isolated; isolation instead implemented later in the power chain. This approach is adopted here: the MPPT being un-isolated and isolation being gained at the inverter stage if required [53], [89–91]. A number of power converter topologies meet these basic requirements and have been previously described in literature for this MPPT purpose [77], the reduced set of single ended non-isolated converters is shown in Figure 4-4. This reduced set forms the basis for the following analysis.

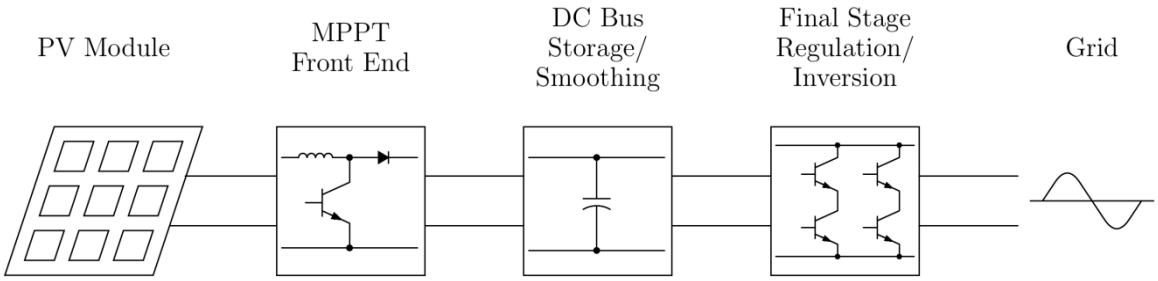

Figure 4-3: Typical PV generation system for grid in-feed applications.

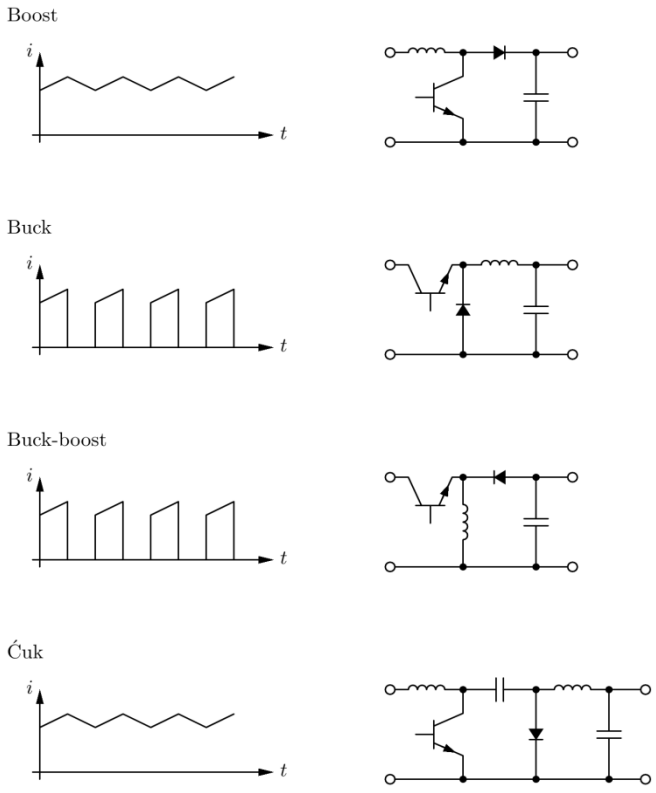

Figure 4-4: Various common SMPC topologies used in PV applications shown with their accompanying input current waveforms.

For initial simplicity, it is assumed that no electrical filtering of switching noise occurs before the front-end converter, and therefore appears at the input to the PV panel. The existence of a pre-filter can impact the efficiency, and thus in this case will be neglected until their requirements are better understood. Filtering is often considered from the basis of electromagnetic compatibility standards and serves to eliminate the effects of voltage- and current-induced noise. The SMPC waveforms previously reported are harmonically complex and, strictly, contain frequency components up to infinite frequency. In reality a certain degree of filtering is provided by both cable inductances and parasitic capacitances. Over the frequency range of 100 kHz to 3 MHz, CISPR standards dictate that a source impedance of 150 ohms (inductive) must be used to quantify the effects of conducted noise, stability and external disturbances in AC and DC power networks [92]. In a more PV orientated consideration, a 3 metre length of wire, with conductors separated consistently by 1 centimetre will have an inductance of approximately 2.25 microhenrys, which gives a differential mode impedance of

1.41 Ω at 100 kHz and of 141 Ω at 10 MHz. The presence of this series impedance will modify the spectral content of the waveform by reducing the amplitude of higher harmonics seen by the PV module. The fundamental and a small fraction of the lower harmonics (2^{nd} to 5^{th} harmonics) will remain, and will be considered as the main disturbance to the PV module. Figure 4-5 shows the typical spectral content for a continuous-mode triangle wave input current waveform, characteristic of a SMPS, at 100 kHz with harmonics extending up to 2.1 MHz (shown as the upper line in green). The spectrum is then modified by the inclusion of the impedance due to the cable inductance (2.25 µH) as previously stated. The resultant contains much-reduced high order harmonic content and a greater proportion of its energy is carried by the lower frequencies. Because of this filtering effect of the higher frequencies, a pure sine-wave excitation will be used to model the AC ripple drawn by the SMPS.

A pure sine-wave excitation will, during practical experiments where frequency-dependent effects are likely to occur, produce results that can provide more useful information on the high frequency behaviour of the PV module unaffected by non-uniform harmonic frequency effects.

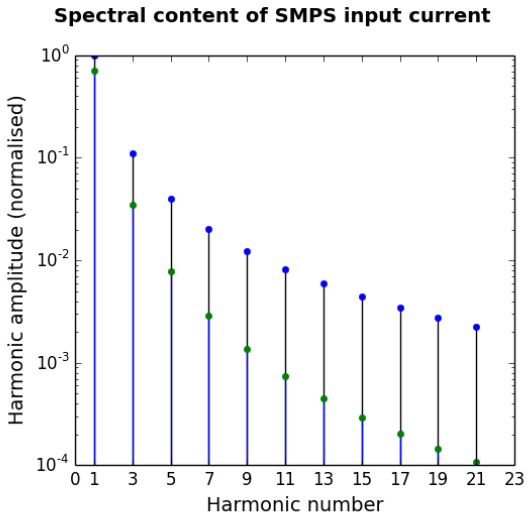

Figure 4-5: The harmonic content for a triangle wave, unfiltered in blue and filtered by a 20 dB/decade slope in green. This demonstrates the amount by which high order harmonics are reduced, justifying the calculation of high frequency transfer efficiency by pure sine-wave.

4.2.2 - Modelling a PV module

A model has been previously presented which takes into account various frequency-dependent factors in the PV model; this is shown in Figure 4-6. The primary frequency dependence of the electrical characteristics of the PV module comes from the module's junction capacitance which is caused by the combined effects of the individual cell junction capacitances. This capacitance is dependent on manufacturing variations in the cells along with their operating conditions. Further to the initial manufacturing variations, there is also a great difficulty in the characterisation of the junction capacitance due to the non-linear nature of the electrical characteristics of the cells. This non-linear behaviour becomes significant in the capacitance measurement of a PV module, as the DC currents must be close to the MPP conditions, typically above 1 amp. A perturbation current with a magnitude of two or more orders of magnitude below this DC 'bias' current must be injected such that the response can be assumed linear. A signal of this magnitude is within the noise floor of RF-pickup and 'noise' from varying ambient conditions makes measurements impractical. Because of the combined uncertainty in the measurement of the parasitic capacitance, it has been chosen to initially neglect it from the model. The model thus simplifies to that shown in Figure 4-6. The equation determining this behaviour described by the circuit is shown in (2-3). Which in turn simplifies to (4-3) based on the assumption that the series resistance is negligibly small.

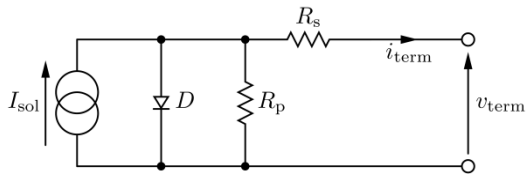

Figure 4-6: PV model used

$$0 = I_{sol} - I_{term} - \frac{V_{term} - R_s I_{term}}{R_p} - I_{D_{sat}} \left(e^{\frac{V_{term} - R_s I_{term}}{V_{D_{th}}}} - 1 \right) \quad (4\text{-}2)$$

Where:

I_{sol}	is the current due to the illumination of the PV cell P-N junctions
V_{term}	is the magnitude of voltage developed at the terminals of the PV module
I_{term}	is the magnitude of current flowing in the output terminals of the PV module
R_p	is the value of parasitic parallel resistance
R_s	is the value of parasitic series resistance
$I_{D_{sat}}$	is the value of the reverse saturation current of the PV cell P-N junctions
$V_{D_{th}}$	is the effective inbuilt-potential of the PV cell P-N junctions

$$0 = I_{sol} - I_{term} - \frac{V_{term}}{R_p} - I_{D_{sat}} \left(e^{\frac{V_{term}}{V_{D_{th}}}} - 1 \right) \quad (4\text{-}3)$$

4.2.3 - Mathematical approach

The process of analysis in this case takes the form of a numerical solution to the PV equation of (4-3) for the DC plus AC ripple current excitation. As previously discussed, the current waveform is modelled as a pure sine wave with amplitude and arbitrary frequency, as shown in (4-4). The analysis is performed for constant illumination.

$$I_{term} = I_{MPP} - \left(\frac{A}{2}\right) \sin(t) \quad (4\text{-}4)$$

Where:

I_{term}	The excitation current applied to the PV module (indicated in Figure 4-6) [A]
I_{MPP}	The maximum power point current of the module [A]
A	The peak-to-peak amplitude of the sine wave excitation [A]
t	A 'time' parameter where $t = [0, 2n\pi], n \in \mathbb{N}$, where *n* is an arbitrary integer to which the resulting (periodic) function is invariant

$$P_t = I_{term} V_{\text{term}}(I_t) \tag{4-5}$$

Where:

P_t	The instantaneous power from the PV module at time *t*
I_{term}	The instantaneous current drawn from the module at time *t*
$V_{term}(I)$	The numerical solution of the PV voltage for a value of *I*

The equation for instantaneous power transferred at any time is determined from (4-5). The expression for the module voltage is determined from the numerical solution of (4-3). The instantaneous power equation is then averaged over an integer number of sine wave cycles as shown in (4-6).

$$P_t = \frac{\int_0^{2n\pi} I_{term} V_{term}(I_{term})\, dt}{\int_0^{2n\pi} dt} \tag{4-6}$$

Where:

P_t	The instantaneous power from the PV module at time *t*
I_{term}	The instantaneous current drawn from the module at time *t*
$V_{term}(I)$	The numerical solution of the PV voltage for a value of *I*
n	An integer such that the integration is performed over an integer number of cycles : $n \in \mathbb{N}$

Numerical data from a characterisation of a PV module under constant illumination from halogen illumination, as described in Chapter 2, was reduced in order to model parameters which could be used in a mathematical model to perform the analysis. This process of reduction to model parameters was performed using a least-squares curve fitting process of the measured data to the equation describing the PV equivalent circuit model, shown in (4-3). With the equation in the form presented in (4-3), replacing the equality to zero instead to an arbitrary error, ε, as shown in (4-7) and by replacement of the terminal voltage and current with tuples, (V_i, I_i), representing pairs of measured voltage and current. The model can be solved in a least squares fashion as shown in (4-8) such that the resulting parameters, $\{I_{sol}, V_{D_{th}}, I_{D_{sat}}, R_p\}$, form the set required in the model. The minimisation was performed using the Nedler-Mead simplex algorithm [28]. Figure 4-7 shows a comparison the original measured data and that generated by the model, Table 4-1 shows the model parameters extracted from the original data used in the modelled data curve of Figure 4-7.

$$\varepsilon(V_i, I_i) = I_{sol} - I_i - \frac{V_i}{R_p} - I_{D_{sat}}\left(e^{\frac{V_i}{V_{D_{th}}}} - 1\right) \tag{4-7}$$

Where: (V_i, I_i) are tuples of measured voltage and current pairs for the PV module under characterisation. The remaining variables have the same meaning as in (4-3).

$$\min_{\left(I_{sol}, V_{D_{th}}, I_{D_{sat}}, R_p\right)} \sum_{i=1}^{N} \{\varepsilon^2(V_i, I_i)\} \tag{4-8}$$

Parameter	Value
I_{sol}	635 mA
$V_{D_{th}}$	1.01 V
$I_{D_{sat}}$	1 mA
R_p	17 kΩ

Table 4-1: Model parameters extracted from PV data for the numerical analysis

A solution for $V(I)$ (that is voltage as a function of current) can only be found by numerical means given the transcendental and implicit nature of the equation. Voltage was calculated in terms of current using the Van Wijngaarden-Dekker-Brent root finding method. Equation (4-5) can be used directly with error term, in the form $\varepsilon(V_i, I_i)$, replacing the initial zero of equation as shown in (4-7), which produces an equation with a unique root (zero crossing) at the values of V_i and I_i that satisfy the equation. This produces an equation as shown in (4-9).

$$V(I) = \text{VWDB}(\varepsilon(V, I), V) \quad \text{for} \quad I \tag{4-9}$$

Where: $\text{VWDB}(f(x), x)$ denotes the application of the Van Wijngaarden-Dekker-Brent method to find the root of function $f(x)$ with respect to x.

In order to solve (4-6) in a numerical domain (as opposed to analytical), the equations to be solved must be digitised with respect to time, *t*. This is performed as shown in (4-10).

$$t = [0, \delta, 2\delta, \ldots, 2\pi]$$

Time is represented as a discrete series from 0 to 2π such that t_i represents any discrete instant in time where i is any integer between 1 and N, where N is the number of time intervals and $N = 2\pi/\delta + 1$

The excitation current is calculated as:

$$I_i = I_{MPP}\left(\frac{A}{2}\right)\sin(t_i)$$

As thus consists of N elements. (4-10)

$$V_i = V(I_i) = \text{VWDB}(\varepsilon(V, I_i), V)$$

And power is calculated as

$$P_i = V_i I_i$$

The average power over the 2π period is thus calculated by the trapezium rule as:

$$P_t = \frac{1}{N}\sum_{i=1}^{N} P_i$$

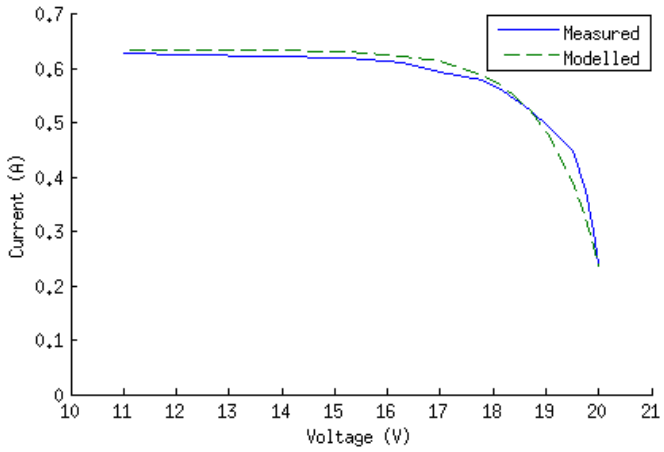

Figure 4-7: A comparison of the measured and modelled PV module characteristic used in the theoretical analysis of transfer efficiency presented.

4.2.4 - Theoretical results

Presented in Figure 4-8 is the result of the numerical analysis applied to the PV model shown previously. There is a clear degradation in transfer efficiency with increased current ripple. The

current ripple has been normalised to the maximum power point current of the module under the test conditions, which was 420 mA in this case.

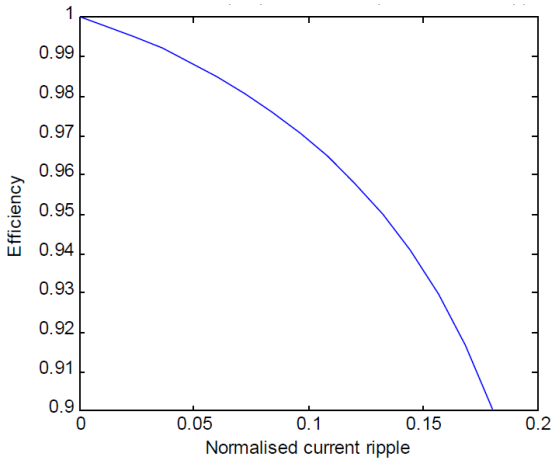

Figure 4-8: Transfer efficiency results for the theoretical analysis

4.3 - An experimental test rig for evaluation of PV module small signal behaviour

A PV test facility, previously described in Chapter 2, will here be used to validate theoretical results. A number of considerations were raised during the work described in this chapter that prompted modifications to the experimental rig, such as the adoption of a stabilised DC power supply for the lighting, rather than mains supply, as the voltage and current measurements are highly sensitive to variations in insolation, and could be affected by small variations in light output due to the mains supply frequency if AC powered lights were used. Both noise due to ripple in illumination and mechanical vibration in the physical supports were sufficient to cause large variations in the measurements, therefore, the mechanical integrity of the test system was also increased.

4.3.1 - A high speed electronic load: a power supply emulator

Previous research has employed power amplifiers to provide a perturbation that is capacitively coupled to the DC loading of the illuminated PV module. In previous literature, it has also been stated that for this purpose an audio frequency power amplifier was used, explaining certain difficulties in

producing excitations in the frequency range more typical of SMPCs (>20kHz) in these works. In the amplifier-capacitor method of signal injection, over a wide frequency range, the AC coupling capacitor becomes prohibitively large to operate at low frequency and high ripple current amplitude. Furthermore, the isolation of the loading condition becomes difficult, which prohibits the use of electronic loads which have poorly defined high frequency impedance. These two problems set both upper and lower frequency limits of the system.

Problems encountered by previous researchers on this topic provided sufficient impetus to produce a custom electronic load for this purpose [45]. The electronic load is capable of providing both DC bias and AC perturbation to the PV module. This arrangement eliminates the requirement for AC coupling capacitors in the power circuit. The proposed topology for the electronic load is described in the schematic in Figure 4-9. The load is, in essence a cascode pair of BJTs. Bipolar technology was chosen over MOSFETs because of the generally lower Miller capacitance that increases the effectiveness of high frequency (HF) bypassing on the cascode bias generator, increasing the system bandwidth.

The practical load was verified by a DC linearity test, time-domain step response and by examination of the pure sine-wave response. The DC linearity was tested by sweeping the DC control signal over a range from 0 to 1 A, which is the expected operating region of the load. The control voltage and load current were measured over this sweep with results shown in Figure 4-10. The linearity of the control voltage with current is poor below 50 mA but over the remainder of the range shows good agreement.

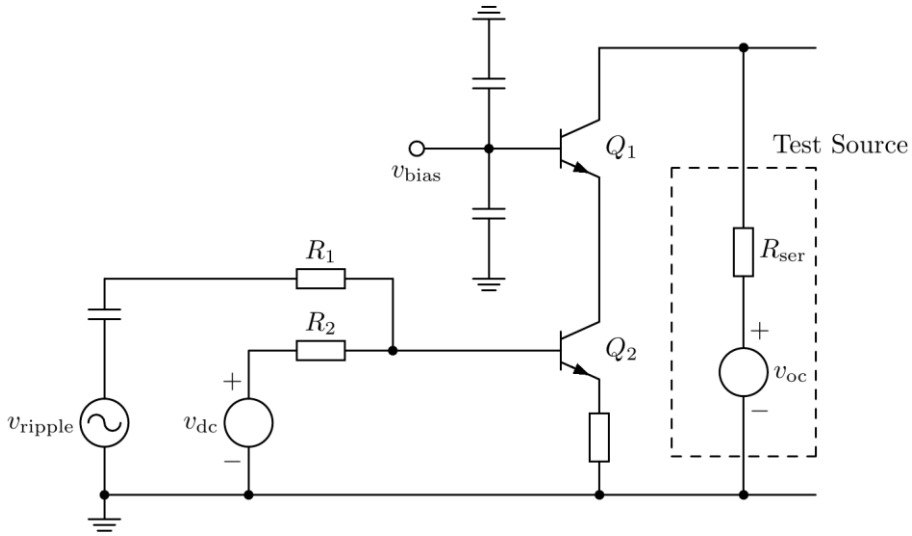

Figure 4-9: The schematic outline of the high-speed electronic load. The cascode bias generator generates the voltage labelled v_{bias} on the base terminal of Q1. DC load-point setting is performed by v_{dc} and the AC perturbation is delivered by v_{ripple} via a DC blocking capacitor. The test source indicated was used as the basis of the performance tests.

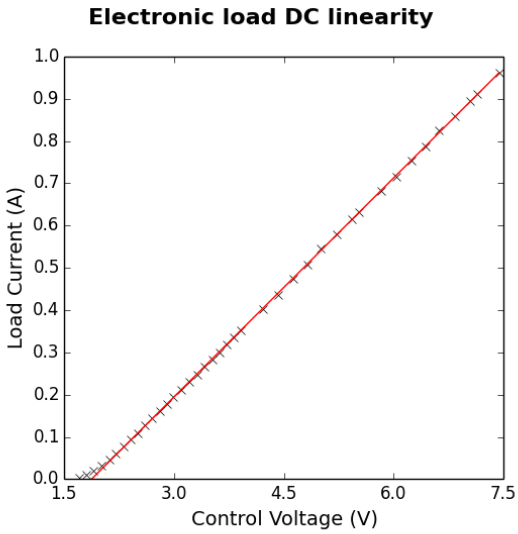

Figure 4-10: The DC response of the high-speed load. Measurement points are indicated by the (x) markers and a linear regression line is shown by the continuous line.

The frequency response of the electronic load was measuring using a step-response method as this would also indicate problems due to slew-rate limitation and other undesired limitations. The results shown in Figure 4-11 Show the response of load current to a fast edged square wave pulse-train control voltage causing a 105 mA step change in load current. The 10-90% response time of the waveform is 139 ns which, by the first order relationship $t_{10-90\%} = 2.2RC$, is representative of a 15.8 MHz bandwidth also no direct slew rate limitation is apparent.

For final verification of the load, Figure 4-12 shows the response of the load to a sine-wave perturbation. The perturbation was a 700 kHz, 120 $mV_{pk\text{-}pk}$ sine-wave, a high-frequency blip is apparent at the crest and trough of the excitation waveform (see Figure 4-12), this is indicative of the higher frequencies produced by the signal generator (Krohn-Hite 5300A). However, no great distortion is apparent in the output waveform. Quantitative measurement of THD is not possible to any meaningful resolution using the equipment available.

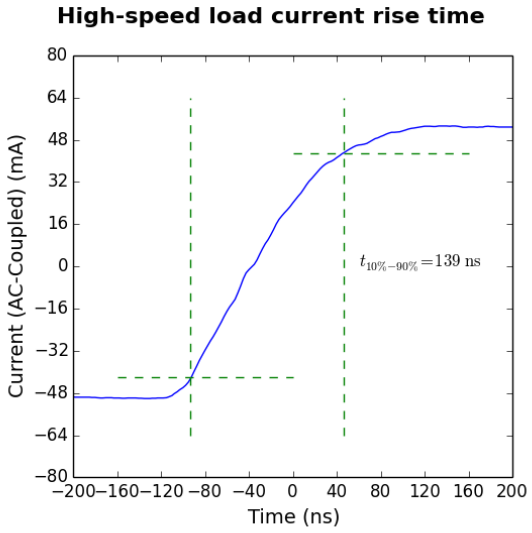

Figure 4-11: The response of the load current to a square-wave signal. The rise time is shown as 139 ns which is representative of a small signal bandwidth of 15.8 MHz.

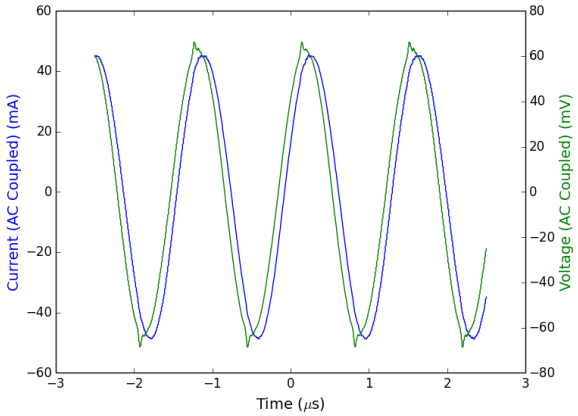

Figure 4-12: The response of the high-speed load to a 700 kHz, 120 $mV_{pk\text{-}pk}$ perturbation.

4.3.2 - A smooth artificial illumination source

As described in Chapter 2, the standard 50 Hz mains power supplied to the halogen lamps (providing the artificial illumination) proved impractical for this application because of the amplitude of the 100 Hz ripple caused by the pulsed heating of the lamp filament. For the noise sensitive measurements presented here, a DC source was utilised, providing the requisite 240 V_{rms} to power the filaments with a smooth DC power waveform, eliminating the ripple in the illumination.

4.3.3 - Experimental procedure

Figure 4-13 shows a schematic outline of the measurement setup. The measurement follows the same principals as the theoretical analysis. The multiplication of voltage and current along with the integer cycle averaging in order to calculate the average power over a number of whole cycles. The equipment utilised is stated in Table 4-2.

Purpose	Item
AC/DC current measurement	LEM PR50 – DC-50 MHz current probe
Oscilloscope – measurement and maths functions	Agilent 54624A – 100 MHz quad channel digitising oscilloscope
DC measurements	Hewlett Packard 34401A 6½ digit multimeter
DC Power supply for illumination	Sorensen Power DCR 300-9B
Function generator for excitation current	Krohn-Hite 5300A 2 MHz function generator

Table 4-2: Equipment used in practical measurement

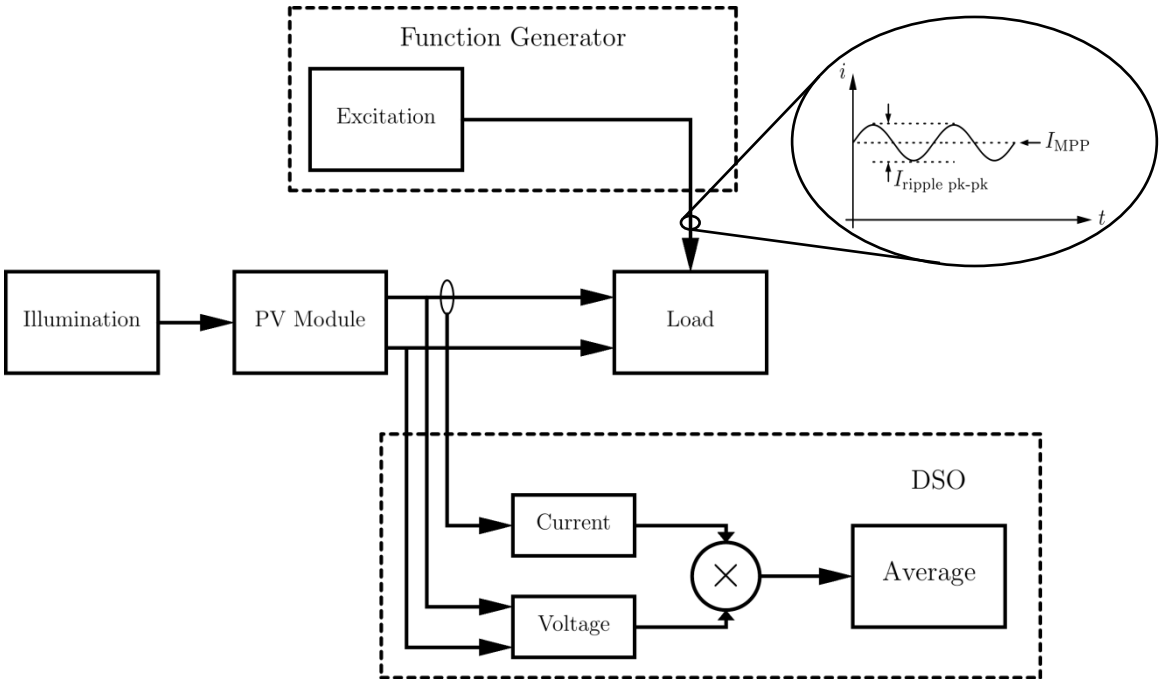

Figure 4-13: A schematic diagram outline of the experimental setup used to quantify the effects of transfer efficiency on a real PV module.

4.4 - Experimental results

Results are shown here from the experimental work performed. Figure 4-14 shows the response of the module to perturbations over a range of amplitudes at three individual frequencies for comparison. At each frequency, a clear trend can be seen in that the ratio of power extracted to power available (transfer efficiency) reduces with increased ripple amplitude. The trend is less pronounced at higher frequency, this efect is better shown in Figure 4-15. Figure 4-15 shows the transfer efficiency over a range of frequency for three individual ripple amplitudes.

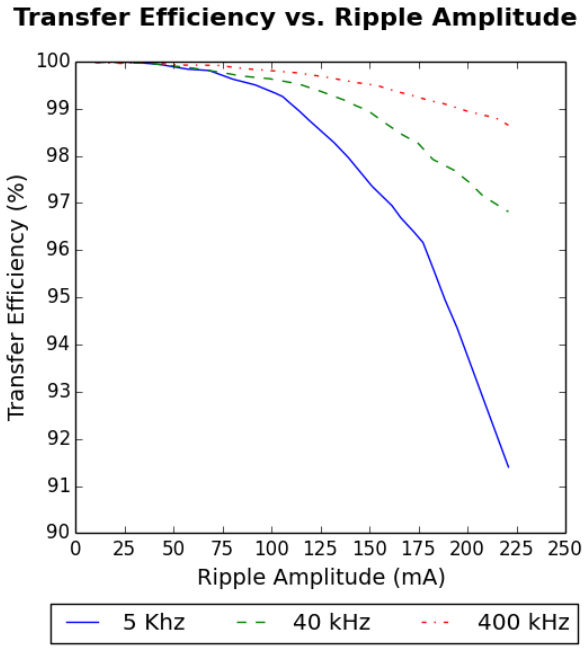

Figure 4-14: Experimental results showing the variation of transfer efficiency with increasing ripple amplitude at fixed frequency. The results have been repeated for three frequencies of ripple current indicated by the three lines. Amplitudes are quoted as peak to peak measurements.

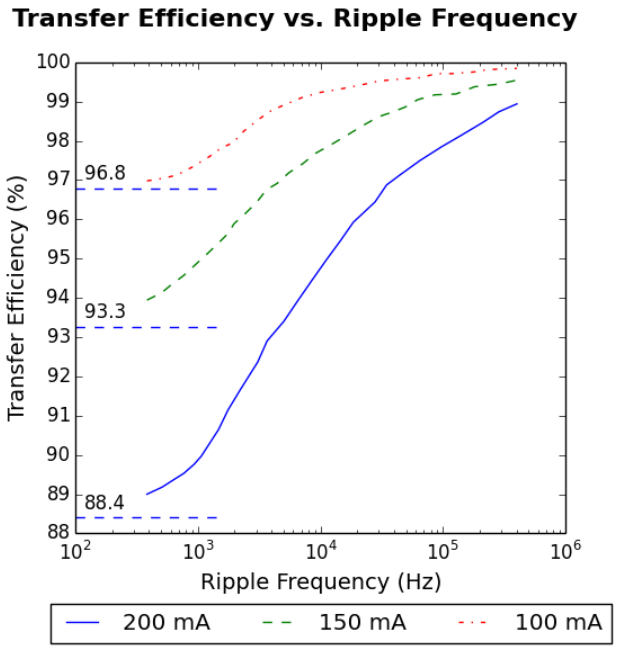

Figure 4-15: Experimental results showing the variation of transfer efficiency with increasing ripple current frequency. This frequency response is shown for three amplitudes of ripple current (shown in mA pk-pk). Theoretical values for ripple amplitudes corresponding to the curves are marked on the graph, the curves show a clear tendency towards them with decreasing frequency.

4.5 - Discussion

The results shown here demonstrate both that there is a significant degradation to transfer efficiency for both high amplitude and low frequency current ripple.

The frequency response of transfer efficiency is shown and forms two plateaus. At high frequency, the response tends towards maximum efficiency. The high frequency response can indisputably be due to the effects of the PV cell parasitic capacitance and the parasitic inductance of cables used in the experiment. The plateau at low frequency appears to converge towards the theoretical values. These theoretical values were based on an assumption of negligible frequency dependence, as described in earlier sections. This apparent tendency of the experimental result towards the theoretical therefore suggests a region of minimal frequency-dependent effects, which is consistent with the low frequency.

At 100 kHz, the transfer efficiency approaches 98% for a 200 mA ripple current amplitude. The PV module used in this investigation has a short circuit current of approximately 2 A, that is 200 mA ripple typical of a 10% current ripple used in the design criteria for the primary inductor of a SMPC.

4.5.1 - Impact on Power converter efficiency

Basic analysis of the results would lead to the conclusion that, by increasing the switching frequency and reducing the ripple current, it is possible to nearly eradicate the reduction in transfer efficiency under the conditions shown. In order to realise the advantage of high transfer efficiency, the constraints of high frequency and low ripple must be applied to the power converter design. These will affect design constraints of size, weight and efficiency. To understand better the impact of the results the transfer efficiency for conditions of frequency and current-ripple they must be considered alongside the associated power converter losses.

To evaluate the effects of the constraints applied to the power converter a simplified loss model of a boost converter has been prepared. The loss model only considers dominant effects of frequency and ripple by neglecting DC resistance and ON/OFF state losses in active components, and therefore only considers the switching losses and magnetics losses [89]. DC losses in active and passive components have been neglected as they are largely independent on the current ripple magnitude, and magnetic losses are strongly dependent on both frequency and magnitude of AC ripple. Similarly switching losses are solely dependent on switching frequency for constant ambient and drive conditions. Figure 4-16 shows a chart depicting the relationships between the various loss mechanisms affected by frequency and ripple. For modest values of ripple, the difference between the RMS and average value remains within marginal error and has minimal effect on the ripple-associated losses.

It is assumed that the magnetic components are constructed from litz-wire of a sufficient grade as to minimise AC-resistance losses due to that are associated skin effect with increased frequency.

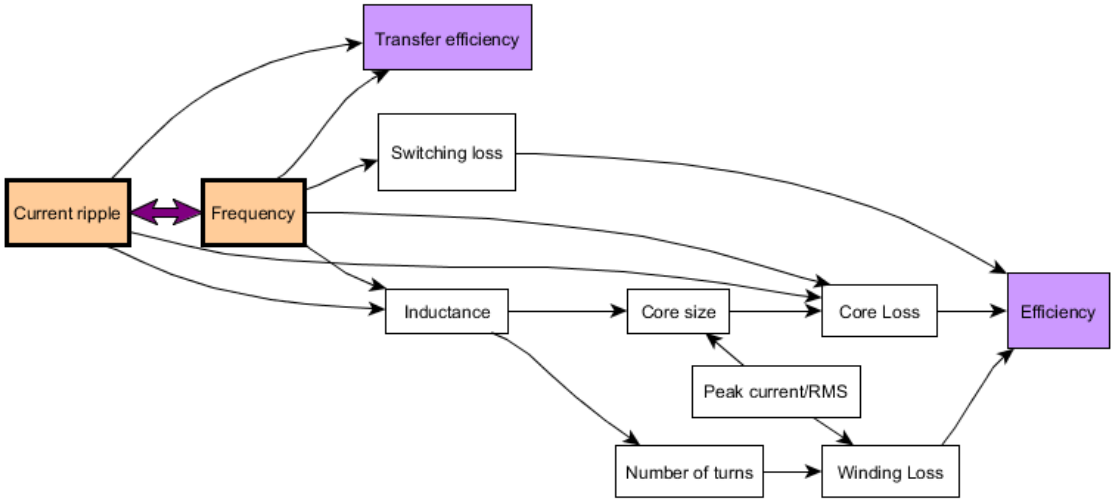

Figure 4-16: An overview of the frequency and ripple dependent loss factors for a boost converter

The specifics of the loss estimation are detailed in the following sections.

4.5.1.i - Magnetic losses

Magnetic core losses as previously mentioned dependent on both peak-peak flux density swing and winding losses. Winding losses are also a critical element in the efficiency calculation that whilst being strictly a DC loss the choice of inductance value determined from current ripple and frequency requirements determines the number of winding turns and therefore its DC resistance.

The design of the inductor follows a flux limited approach described by Mohan [34]. The approach set forth by Mohan et al is similar to many described in literature . Losses for the magnetic component are based on the winding resistance and specific core loss for a specific case of 3F3 material. In a more practical sense, ferrite material choices are the result of a trade-off between cost, efficiency, temperature stability of characteristics and availability in specific core forms. Because many of the selection criteria fall out of the scope of this analysis and only a single core material (3F3) is considered in this process.

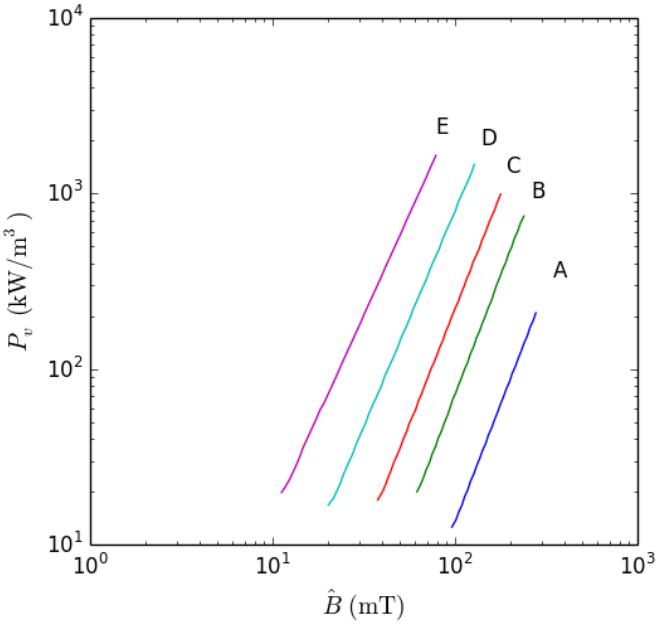

Figure 4-17: Loss curves for the 3F3, data taken from Ferroxcube

A: 25 kHz B: 100 kHz C: 200 kHz

D: 400 kHz E: 700 kHz

A curve fit is applied to this data in order to determine the Steinmetz equation parameters. The loss curve is shown in Figure 4-17 for five frequencies: 25 kHz, 100 kHz, 200 kHz, 400 kHz and 700 kHz, labelled A to E respectively.

$$P_v = k f^{\alpha} \hat{B}^{\beta} \tag{4-11}$$

Where:

P_v	is the specific loss power in the ferrite
k	an arbitrary constant of proportionality
f	is the frequency of the alternating flux-density, B
α	is the frequency associated loss parameter
$\hat{B}$	is the peak value of the alternating flux-density, B
β	is the flux-density associated loss parameter

The loss presented in the 3F3 data sheet shows a linear relationship between $\log(P_v)$ and $\log(\hat{B})$, for discrete frequencies. This implies a constant value for α, and agreement with the flux-density associated loss in the Steinmetz equation. By applying a logarithm (base 10) to both sides of the

equation, the results of (4-12) is produced which for individual frequencies can be related to the equation of the straight line as in (4-13).

$$\begin{aligned} &\log(P_v) = \log\left(k f^{\alpha} \hat{B}^{\beta}\right) \Rightarrow \\ &\log(P_v) = \log k + \log f^{\alpha} + \log \hat{B}^{\beta} \Rightarrow \\ &\log(P_v) = \log k + \alpha \log f + \beta \log \hat{B} \end{aligned} \tag{4-12}$$

$$[\log(P_v)]_{f_{A\ldots E}} = [\log k + \alpha \log f]_{f=f_{A\ldots E}} + \beta \log \hat{B} \equiv y = a + bx \tag{4-13}$$

Where:

$$\begin{aligned} a_{f_{A\ldots E}} &= [\log k + \alpha \log f]_{f=f_{A\ldots D}} \\ b &= \beta \\ x &= \log \hat{B} \\ y &= [\log(P_v)]_{f=f_{A\ldots D}} \end{aligned}$$

The values for the *y*-intercept from the initial curve fit for each frequency of the form of (4-14), can then be subject to a second curve fit in order to disseminate the value of *k* and α.

$$a_{f_{A\ldots E}} = [\log k + \alpha \log f]_{f=f_{A\ldots D}} \tag{4-14}$$

The curve fit is applied to the data of the form shown in (4-15).

$$a_{f_{A\ldots E}} = \log k + \alpha \log f \equiv y = a + bx \tag{4-15}$$

Where:

$$\begin{aligned} a &= \log k \\ b &= \beta \\ x &= \log f \\ y &= a_{f_{A\ldots E}} \end{aligned}$$

This process produced a value for $\alpha = 1.35$ for f in kHz; a value for $\beta = 2.7$ for $\hat{B}$ in tesla producing a specific loss in units of W/cm^3.

4.5.1.ii - Switching losses

Considering the peak current and voltage for the power condition of the PV module operating at 20W with MPP voltage of 17 V at 1.18 A, and a constant switching transition time, the switching loss is calculated as in (4-16).

$$P_{sw} = f_{sw}\frac{1}{2}V_{out}\left(I_{in_{ave}} + \frac{\Delta I}{2}\right)t_{sw_{off}} + f_{sw}\frac{1}{2}V_{out}\left(I_{in_{ave}} - \frac{\Delta I}{2}\right)t_{sw_{on}} \quad (4\text{-}16)$$

Where:

P_{sw}	is tteady state switching loss
f_{sw}	is converter switching frequency
V_{out}	is steady state output voltage of the converter
$I_{in_{ave}}$	is average steady state input current to the converter
ΔI	is steady state peak-peak inductor ripple current

The resulting power converter efficiency over a range of frequency and ripple current is shown in Figure 4-18. A clear degradation in efficiency is apparent as the frequency of operation is increased. There is little variation in efficiency with varying ripple current. The greatest influence on the high frequency losses are the switching losses. These results have been combined with those of the practical transfer efficiency to produce a speculative complete system efficiency as shown in Figure 4-19.

Figure 4-19 shows that the increased transfer efficiency at increased frequency is practically eradicated by the reduced efficiency of the power converter. The most apparent benefit is that total system efficiency can be increased by a reduction in the current ripple whist maintaining either constant or reduced frequency. This can only be achieved with a greater inductance, or alternative power converter topologies. Furthermore, the losses demonstrated in Figure 4-19 are consistent with the findings of Beltrame et al [93] who provided a comprehensive overview of the losses mechanisms of a boost converter for PV applications by theory and experimental validation.

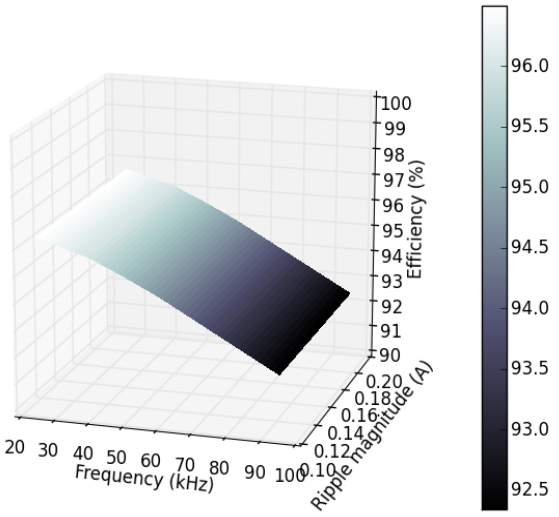

Figure 4-18: Modelled power converter losses.

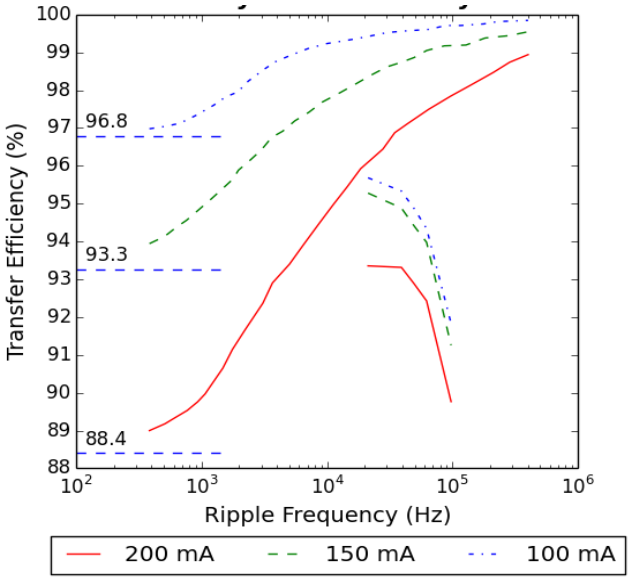

Figure 4-19: Modelled power converter losses.

4.6 - Chapter conclusions

The concept of transfer-efficiency has been introduced and explained from a position where pure DC voltages and currents are considered for the PV module. This concept has then been analysed in a computational basis and experimental validation of the matter has successfully indicated conditions where transfer efficiency is maximised.

The experimental methodology required to perform such measurements under controlled conditions has been presented with details of specific modifications to the experimental rig described in Chapter 2. Results gathered from the experiment show agreement only at low frequency, as predicted. The effects of frequency dependent-factors such as parasitic elements within the module can act to improve the transfer efficiency of the module when presented with loads containing significant current ripple.

The apparent constraints that one must apply to a power converter in order to gain optimal performance, i.e. use of high frequency switching and low current ripple, are further investigated. The constraints are investigated with the analysis of a basic loss model of a boost converter, the loss model takes into account the factors of current ripple and switching frequency to expose the effects on the power converter's efficiency. The effect of increasing frequency has been shown to degrade the total system efficiency whereas benefits can be had by increasing the inductance, (reducing the current ripple for fixed frequency). Increasing the inductance for a fixed frequency will pose greater problems to the system designer in that power density and cost can be decreased. The equivalent effect of cost reduction and power density would also be seen by the inclusion of an input differential mode power filter.

The explored effects of switching converter induced current ripple on the efficiency of a PV module now leads to the primary constraint that to optimise the performance of the system and preserve design constraints including cost, weight, material usage which are key in low carbon and 'green' energy; alternative converter topologies must be explored to maximise transfer efficiency.

Chapter 5 - A wide operating range zero ripple SEPIC converter

Chapter 4 demonstrated how the average output power from the PV cell or module is affected by the current ripple superimposed on the DC average current drawn from the device.. This effect was shown to diminish at conditions of either high frequency (above 200 kHz) or as the current ripple approaches zero. If these constraints are imposed during the design of a SMPS for a PV system, whilst improving the transfer efficiency in the PV unit, the SMPS efficiency and thus total system efficiency is severely degraded. It was therefore proposed in the conclusions of Chapter 4 that a converter topology other than a classic boost converter should be used to maximise overall system efficiency. Primarily, two options exist from established technologies. Either resonant power converters, which can operate efficiently at high frequency, or low-ripple topologies such as the dual inductor circuits, namely the SEPIC and Ćuk converters, which can operate efficiently at low input current ripple.

Whilst there is an apparent advantage of resonant power converters operating at high efficiency at high switching frequencies, they require additional filtering to avoid problems with EMC. This filtering must be designed with knowledge of the particular PV characteristic of the module with which they will be used. This chapter therefore presents a design for a zero input current ripple SEPIC converter. The SEPIC converter has been shown in previous literature [41]to operate successfully with near zero input current ripple; however, stringent operating limits and design constraints are required to realise this using a simple design approach. Presented in this chapter is a novel approach to the SEPIC converter design which includes a variable inductor which can compensate for variations in input ripple normally seen over wide operating conditions, typically required in PV applications.

5.1 - Introduction

A solution of the problem of reduced transfer efficiency is through the use of zero-ripple power converter topologies. The zero-ripple phenomena originally explored by Ćuk and Middlebrook [35],

and exists when the magnetic components of Ćuk and SEPIC converters are coupled. SEPIC converters are often favoured for their ability to operate at near-zero input current ripple [41], [94–97]. However, in a practical power converter, a true zero-ripple condition cannot be met because of dynamic variations of components and the effects of parasitic elements. In the presented designs, the zero-ripple condition can be best met at a single operating condition [96]. However, the power generated by a PV module is largely dependent on environmental conditions, and varies widely during operation: this limits the direct benefits gained by using a SEPIC converter for PV applications. Deviations from the ideal zero-ripple condition are compounded by variations in practical component values, which not only due to initial manufacturing tolerances, but are also dependent on environmental conditions such as temperature and ageing. In this chapter, a modification to the classic coupled inductor s SEPIC converter is modified with the addition of a variable inductor such that the imbalance due to parasitic elements can be corrected. This variable inductor takes the form of a saturable inductor.

A controllable saturable inductor (in contrast to a saturable reactor) is a device which permits a progressively controlled change in inductance whilst maintaining linear behaviour. Saturable inductors have previously been reported in literature [98] primarily for matching of resonant circuit characteristics in induction heating applications. The construction of a saturable inductor is similar to that of a standard inductor with the inclusion of axillary (bias) windings to produce conditions of magnetic flux close to those at saturation where the reluctance of the core begins to change, thus changing the effective reluctance of the magnetic circuit and thereby the inductance of the main coil.

5.2 - The un-coupled inductors SEPIC converter

The schematic diagram of a classic, uncoupled inductor SEPIC converter is shown in Figure 5-1 [35], [99].

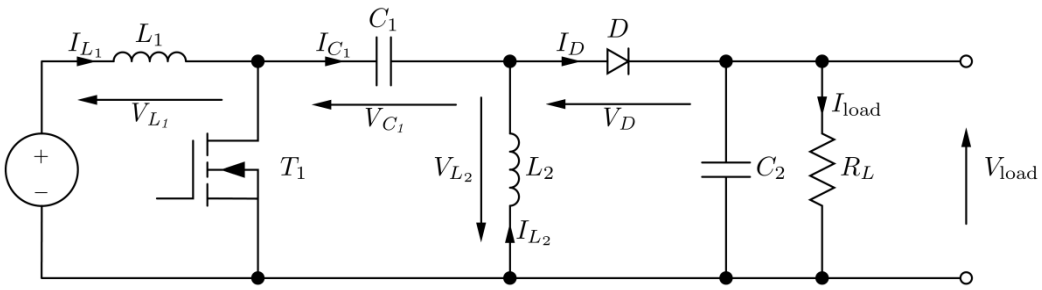

Figure 5-1: The uncoupled-inductors SEPIC converter.

Under steady state conditions, the voltage-time balance for L_1 can be shown as:

$$V_{\text{dc}} \cdot \delta T = \left(V_{LOAD} + V_D - V_{C1} - V_{DC}\right)(1-\delta)T \tag{5-1}$$

Given that the average value of V_{C1} is equal to V_{dc} then this equation reduces to:

$$V_{\text{dc}} \cdot \delta T = \left(V_{\text{LOAD}} + V_D\ \right)(1-\delta)T, \tag{5-2}$$

rearranging gives,

$$\frac{V_{LOAD}+V_D}{V_{dc}} = \frac{\delta}{1-\delta}, \tag{5-3}$$

which, is the relationship between the converter gain and duty cycle. This relationship is valid for both coupled and non-coupled inductor SEPIC converters operating under continuous capacitor voltage conditions [4] [8].

5.3 - The coupled inductors SEPIC converter

A circuit diagram of the coupled-inductor SEPIC converter is shown in Figure 5-2 . The main switch, T_1, is driven by a pulse width modulated signal of constant switching period T and variable on-time, δT, where δ is the modulation factor or 'duty cycle' [34], [35].

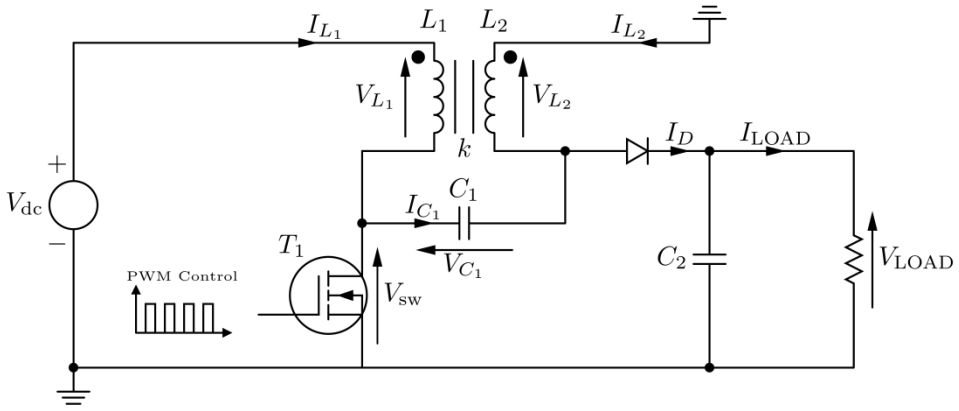

Figure 5-2: The basic coupled-inductors SEPIC converter. Inductors L_1 and L_2 share a magnetic coupling (coupling coefficient, k)

The coupled inductor variant of the SEPIC converter follows the same topology as the uncoupled inductor version, with the constraint of L_1 and L_2 share a common magnetic core. The main advantages of a shared magnetic core between L_1 and L_2 is a reduction in size, weight and cost of the converter.

The steady state analysis has previously been performed for the uncoupled inductors case. The steady state equations are, however, no different since the magnetic coupling affects only dynamic currents, principally of concern here, the ripple.

5.3.1 - The zero ripple condition

The magnetic coupling of the two inductors can be used to null the input current ripple (it is not possible to null the output current of a SEPIC converter as it is discontinuous by nature). The zero-ripple phenomenon was originally explored in the Ćuk converter [35] has also been applied to the SEPIC converter [41]. The coupled inductor SEPIC converter can be analysed by replacing the coupled magnetic element with a tee model equivalent circuit, shown in Figure 5-3 .

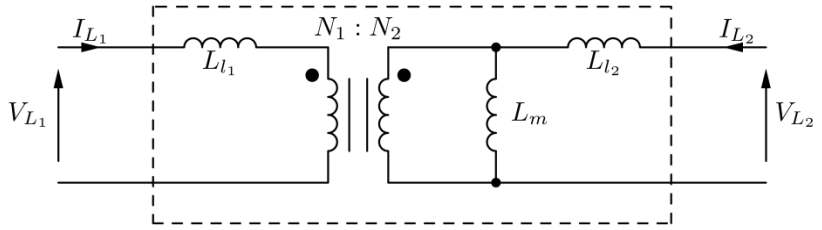

Figure 5-3: Tee model of a coupled inductor

The tee model of the coupled inductor produces the inductance L_1 and L_2 given by the following equations:

$$L_1 = L_{l(1)} + \left(\frac{N_1}{N_2}\right) \cdot L_m \tag{5-4}$$

$$L_2 = L_{l(2)} + L_m \tag{5-5}$$

Using basic circuit theory, the voltage across the mutual inductance can be expressed with respect to V_2 as:

$$V_m = \frac{L_m}{L_m + L_{l(2)}} V_{L2} \tag{5-6}$$

And the voltage across the $L_{l(1)}$ by:

$$V_{L_{l(1)}} = V_{L1} - V_m \left(\frac{N_1}{N_2}\right) \tag{5-7}$$

Under steady state operation with zero-ripple current, the voltage across the primary leakage inductance, $L_{l(1)}$ must be zero. This yields the relationship:

$$V_{L1} = V_m \left(\frac{N_1}{N_2}\right) \tag{5-8}$$

Substituting the previously found expression for V_m, the basic condition for zero-ripple can be found:

$$V_1 = \frac{L_m}{L_m + L_{l(2)}}\left(\frac{N_1}{N_2}\right)V_2 \tag{5-9}$$

Due to tolerances and parasitic components in a real circuit, the zero-ripple condition expressed in (5-9) cannot always be met. A scheme employing a 'compensation' inductance is therefore presented to overcome the problems due to physical realisation.

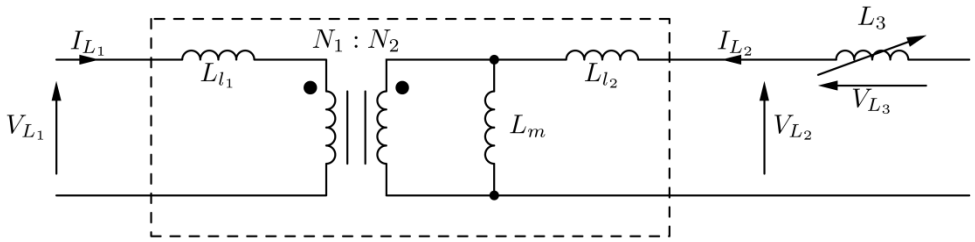

Figure 5-4: Tee model of coupled inductor with additional external variable inductance

The inclusion of the compensation inductor, L_3, in the zero ripple condition from equation (5-9) results in equation (5-10). This can be rearranged as shown in (5-11). The resulting relationship determines the required value of compensation inductance required to correct imbalances of voltages and inductances.

$$V_1 = \frac{L_m}{L_m + L_{l(2)} + L_3} \cdot \left(\frac{N_1}{N_2}\right) \cdot V_2 \tag{5-10}$$

$$L_3 = L_m \cdot \left(\frac{V_2}{V_1} \cdot \frac{N_1}{N_2} - 1\right) - L_{l(2)} \tag{5-11}$$

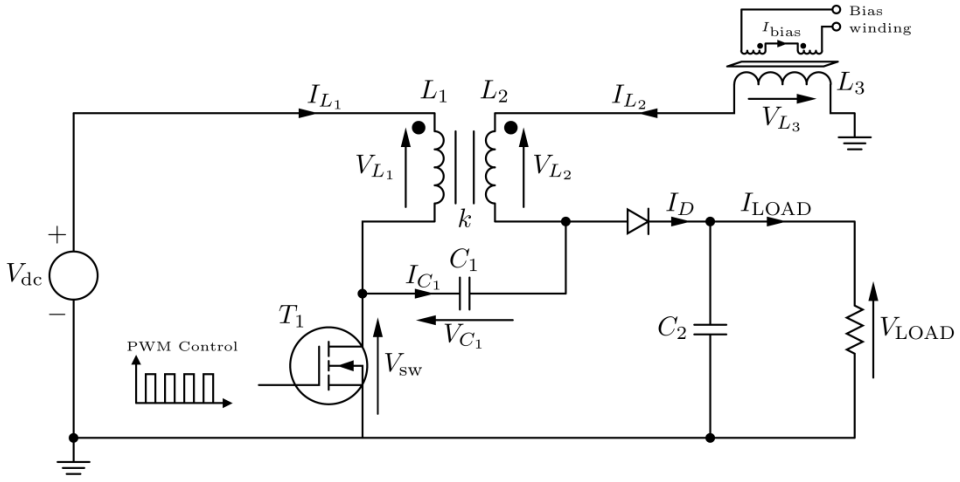

Figure 5-5: A coupled inductors SEPIC converter with additional external variable inductance

From (5-11), one can see that a negative value for L_3 may be required depending on the particular conditions, making the circuit unrealisable. Therefore, in order to ensure this situation does not occur, the turns ratio and mutual inductance can be manipulated to ensure a positive real inductance to meet required voltage conversion and inductance ratios, and therefore physically realisable, compensation inductor. The proposed layout of the SEPIC converter with saturable inductor is shown in Figure 5-5.

5.4 - An electronically variable inductor

To implement a system whereby the ripple can be reduced sufficiently, an inductor whose value can be varied in response to adverse ripple conditions is required. Variable inductors can be implemented using physically moveable cores to alter the magnetic reluctance of the core by physically adjusting an air-gap. A potential method has been previously explored by Sewell et al whereby limbs of the magnetic core are biased with a magnetic flux such that they operate in a non-linear region of their B-H curve.

A design of a variable inductor has previously been presented by Sewell et al [98] for impedance matching in induction heating applications. The physical form of the presented saturable inductor is based on an E-type core. With reference to Figure 5-6, the inductance is provided by a winding

formed on the centre leg of the core (light blue), the winding layout and expected flux pattern is shown in Figure 5-7. Further windings are formed on the two remaining legs (red); these form the magnetic bias for manipulation of the reluctance of the magnetic circuit. The bias windings are wound and connected to an external bias current generator such that no resultant EMF is inducted upon the bias generator, i.e. the induced voltages are equal and opposite. The resulting magnetic circuit is shown by the lumped reluctance model in Figure 5-8.

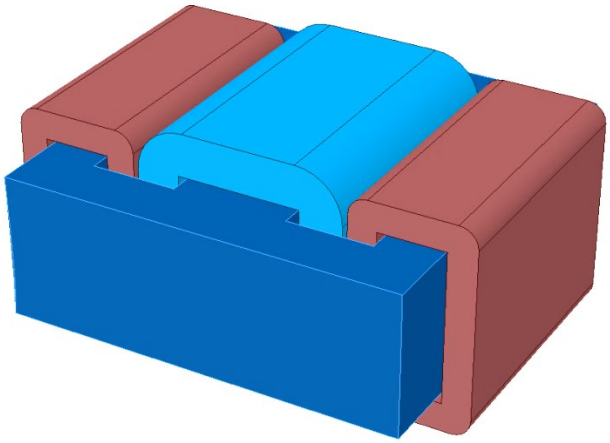

Figure 5-6: 3-dimensional representation of the saturable inductor, primary winding shown in light blue with external bias windings shown in red.

A lumped reluctance model of the E-core is presented in Figure 5-8. The elements MMF_{B1} and MMF_{B2} represent the core bias windings, and are designed such that the flux elements Φ_x and Φ_y are equal and opposite and therefore cancel in the primary flux path (the branch containing S_z). To validate potential designs for the saturable inductor, finite element analysis (FEA) simulations were performed using the FEMM software package. Typical FEA results are shown in Figure 5-9 and Figure 5-11 which were performed using a standard ferrite E-core using N87 material. N87 material was chosen as it is available in many common core-forms, is inexpensive and has acceptable loss characteristics at the frequencies of interest. The non-linear B-H curve of the N87 is shown in Figure 5-10, the non-linearity of this curve is critical to the behaviour of the saturable inductor. Figure 5-9 shows a flux-density plot of the inductor under a particular condition of primary inductor current and bias winding, of particular note is the variation of the flux density in the outer legs, on the left is seen a

reduction and on the right is an increase in flux density, this is due to the interaction of the flux due to the primary inductor adding and subtracting with the bias flux in the outer legs. For clarity, a plot of the flux density on a plane parallel with the air-gap is shown in Figure 5-11. For comparison, Figure 5-15 shows the response of the primary inductance to both bias winding current and primary inductor current, minimal variation due to the primary inductor current, which is key to maintaining the operation of the converter, with the assumed fact that inductance is independent of small variations of current through it.

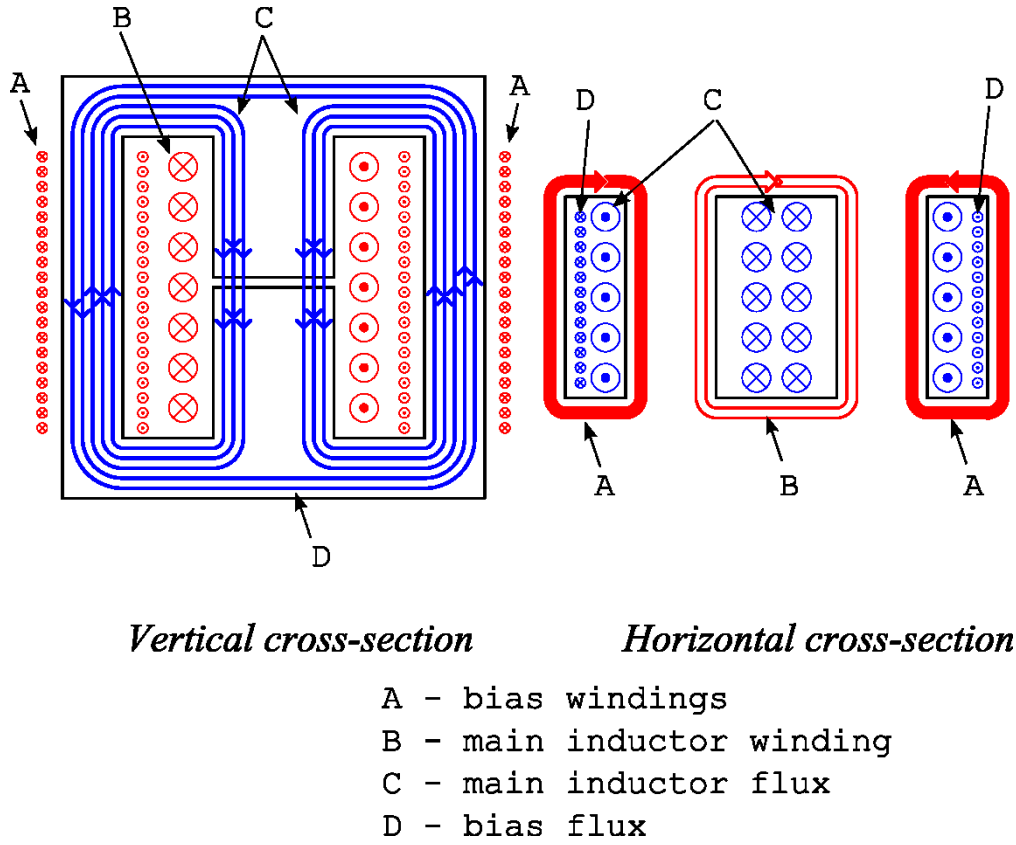

Figure 5-7: Schematic representation of the saturable inductor showing both horizontal and vertical cross sections, the directions of currents and flux are representative of the convention

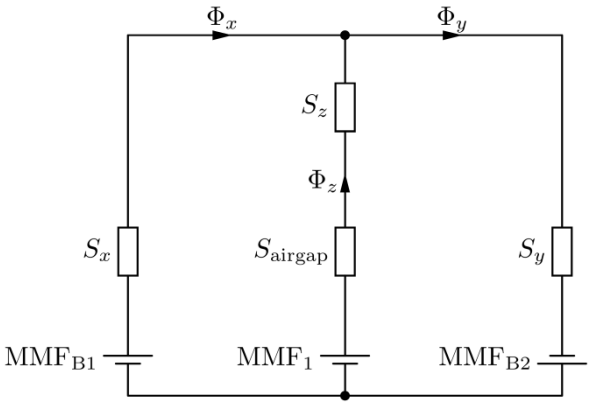

Figure 5-8: Lumped reluctance model of the saturable inductor

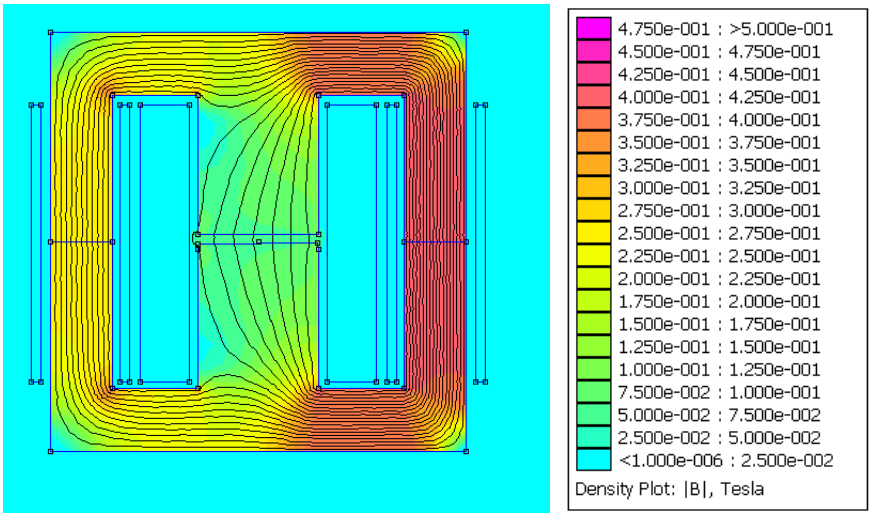

Figure 5-9: An image from one particular run of the finite element simulation, it is visually apparent with the addition and subtraction of flux in the outer legs. The bias windings are held at 100 A.*turns* and 5 A.*turn* is applied to the centre leg.

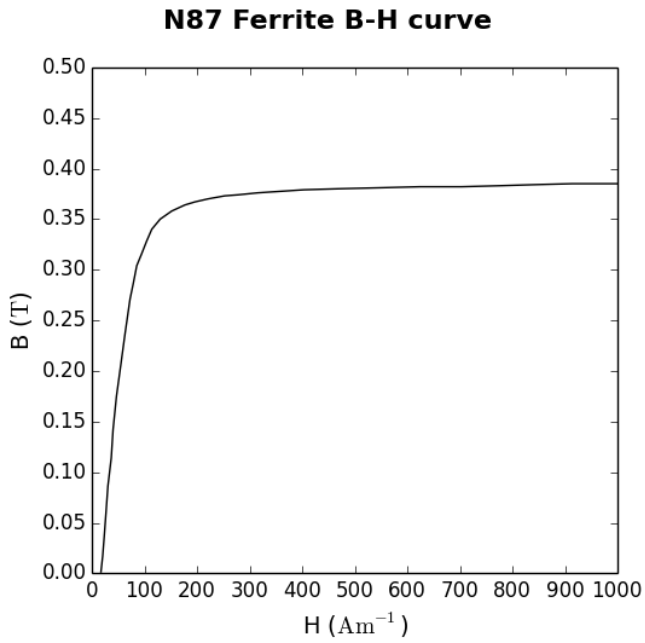

Figure 5-10: N87 ferrite material magnetisation curve

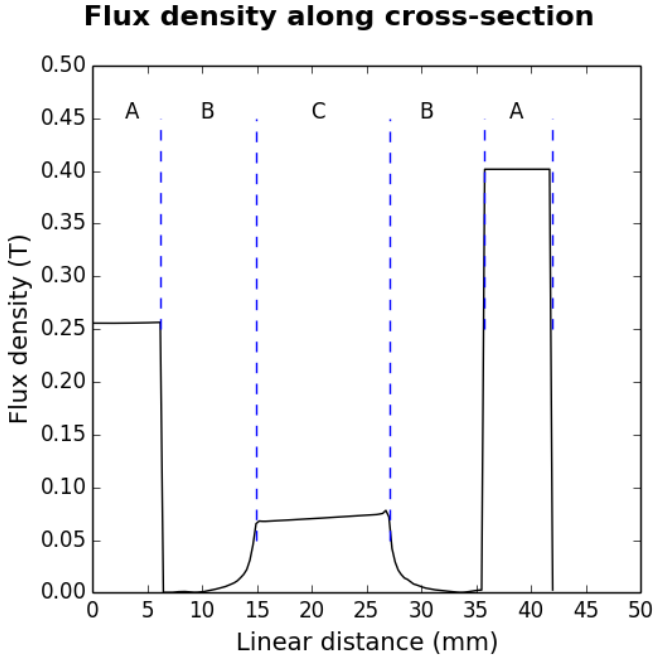

Figure 5-11: A plot showing the flux density along the cross-section, the outer legs, carrying the bias windings are denoted A, the winding window region is shown as B, and the centre leg is shown as C. The difference in the flux density in the two outer legs is consistent with the addition and subtraction of flux due to the primary winding given its direction relative to the bias flux circulating the outer legs.

5.5 - Design of a coupled inductors SEPIC converter for zero ripple operation

In this section, a design case study for a PV battery charger is undertaken to illustrate the design process. A nominally 12 V / 40 W silicon PV module is selected as the power source (the same module used in the transfer efficiency investigation) and two 12 V VRLA batteries connected in series as the load. Dependent on operating condition, the power from the PV module will vary from 0 W to above 40 W. However, to make the design realisable, a lower limit of useable power must be assigned; in this case it is chosen as 10% of the nominal module output, which is 4 W. Known characteristics of the PV module indicate that for the established operating range the power will be produced at a voltage between 10 V and 24 V and a current between 0.7 A and 2.5 A over normal conditions, thus forming the input specification for the SEPIC converter.

The design process for the SEPIC converter is first performed as design with uncoupled inductors; the constraint imposed by their coupling is later applied, noting that it is shown previously that steady state characteristics are independent of coupling. Conditions of continuous inductor current and continuous capacitor voltage must be guaranteed by design to ensure operation as previously calculated. The behaviour of the converter is further ensured with minimal variation (below 1%) in the capacitor voltage over a switching cycle [34].

The input inductance is calculated at the boundary-mode operation; maximum input voltage and minimum input current give rise to the worst case operating conditions.

$$V_{\mathrm{DC}} = L_1 \cdot \frac{dI_1}{dt}$$

$$\Rightarrow L_{2,3} = \frac{V_{\mathrm{DC}} \delta T}{I_{\mathrm{ripple(pk-pk)}}}$$

$$I_{\mathrm{ripple(pk-pk)}} \leq 2 \cdot I_{\mathrm{L1_{min}}} \qquad (5\text{-}12)$$

$$L_1 \geq \frac{V_{\mathrm{DC}} \delta T}{2 \cdot I_{\mathrm{L1_{min}}}}$$

The maximum operating current, which is transferred via the main coupling capacitor as an AC current, now must produce a voltage deviation that is only a small fraction of the DC voltages in the circuit. A peak-to-peak voltage that is no more than 1% of the average DC voltage on the capacitor is chosen: full analysis of the errors in circuit behaviour with respect AC perturbations of the capacitor voltage is presented by Mohan et al [34]. A capacitance of C_1 being 2.2 mF is thus chosen.

Inductance is calculated as shown in (5-12), with minimum input current of 0.7 A, input voltage of 24 V, 100 kHz switching frequency and 50% duty cycle. The result of this suggests a required inductance of at least 85 μH for L_1.

With the input inductance now determined, to ensure that the compensation inductance is a real positive value, an inductance ratio must be determined between L_1 and L_2. The practical value of inductance must be a fraction smaller than the ideal as to permit a realistic value of compensation inductance. The value for the inductance L_3 under ideal circumstances can therefore be calculated from (5-12). L_3 must therefore be within an achievable range of inductance. To meet the zero-ripple condition with this value of inductance the following must be met:

$$L_3 = L_m\left(\frac{V_2}{V_1}\frac{N_1}{N_2} - 1\right) - L_{l2}$$
$$\approx L_3 = L_m\left(\frac{V_2}{V_1}\frac{N_1}{N_2} - 1\right) \quad (5\text{-}13)$$

This ratio has been selected as L_1:L_2 of 1.7:1 which corresponds to a turns ratio of 1.3:1, the ideal condition would be met at a turns ratio of 1.4:1 and thus the proposed inductance ratio requires positive, real compensation.

Component values used calculated by the design process shown are shown in Table 5-1. The range of compensation inductance is to be calculated from SPICE design verification presented in Section 5.5.1 - because of its high degree of dependence on component tolerances that is not easily dealt with analytically.

Component	Value
L_1	84 µH
L_2	50 µH
C_1	2.2 mF

Table 5-1: Calculated component values for the SEPIC converter with coupled inductors and compensation inductance

As the saturation current for the main inductor winding will be dependent on the core bias applied, andto avoid non-linear inductance affecting the behaviour of the converter, the peak-to-peak flux swing of the converter is set at 10% of the saturation point of the unbiased core. A design consideration presented by previous works on the design of saturable inductors presented by Sewel et al [98] shows the maximum variation of inductance as a function of the air-gap size.

5.5.1 - Design verification and calculation of compensation inductance

To verify the design process, a SPICE simulation was performed using Monte Carlo based parameter adjustment to simulate component variations. A Monte Carlo process is used here to reduce

the total number of computations required for an evaluation of the search space. This process is particularly useful where the component values of interest are subject to Gaussian distribution when physically implemented. For each condition of parameter values, a parameter sweep of compensation inductance is performed. Magnetic component nominal values were subjected to a 2σ variation of 20% of nominal value and capacitors to a 2σ variation of 10% of nominal. The standard deviations were obtained from the component data sheets and show a representative figure common amongst many similar components.

The results of this verification and calculation process are shown in Figure 5-12, it shows the ripple magnitude plotted against the compensation inductance value for a selection of the Monte Carlo steps. This shows that over the range of component tolerances and operating conditions, there exists a compensation inductance within the controlled range of the saturable inductor.

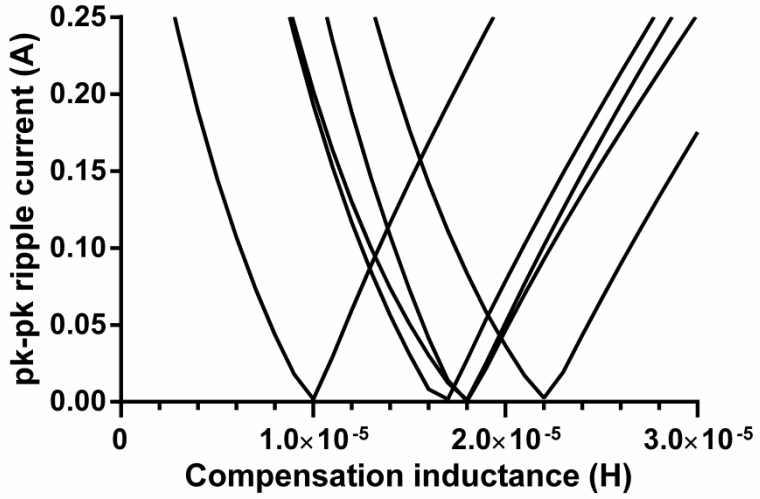

Figure 5-12: Results from SPICE Monte Carlo investigation to determine required range of compensation inductance

With the inclusion of the core bias windings, the saturation characteristics of the main inductance will not be dependent on the current flowing through it alone and to ensure linearity of the inductor under normal operation, a magnetic flux limit constraint is applied as the principal design goal. As the

SPICE verification of the remaining design showed that a required inductance range between 10uH and 22.5uH is required, this corresponds to a control range of 44.4%. According to Sewell et al [98], such a control range is available with a maximum air-gap of 2.5mm.

5.5.2 - Design of the saturable inductor

A sample of the spread-sheet used to calculate the inductors is shown in Table 5-2, showing the optimum inductor solution, which resulted as an E 42/21/15 core with 0.5 mm airgap, populated with 9 turns.

As can be seen in Table 5-2, the solution taken as optimum was not indeed that of least loss. Whilst being attractive for low loss in this application; the concave face in the outer legs of an ETD form core severely reduces the window utilisation, making it a poor choice when using external bias windings. This is clarified in Figure 5-13 which shows outlines of the core forms and the closest possible path which can be followed by a copper winding. Whilst windings could potentially be formed to follow these faces, this requirement demands unconventional manufacturing methods and has as such been neglected for practical implementation.

The available window area is filled with 80 bias winding turns per external leg of the inductor (total of 160 turns). The achievable control range is shown in Figure 5-14; the inductance is measured using a Hioki 3522 LCR meter and current to bias the coils by a standard bench power supply and measured with a HP34401A multimeter.

Figure 5-13: A visual comparison of E and ETD core forms. The E core is shown on the left (hatched cross-section) with the closes possible formation of windings to the body of the core (solid black). The ETD form is shown on the right, there is a region of redundant space between the winding and the concave face.

Parameter ↓ / Core type →	ETD34 with 0.5 mm airgap	E 42/21/15 with 0.5 mm airgap
Inductance factor/Al (H/turn)	2.51E-07	4.54E-07
Core reluctance (H^{-1})	3 984 064	2 202 643
Required inductance (uH)	30	30
Peak current	2	2
Number of turns to meet inductance requirement	13	9
Ampere-turns product for rated current	26	18
Total flux at rated current (μWb)	6.34	8.52
Flux density at rated current (mT)	65	49
Peak current required to saturate the core (ϕ = 200 mT)	6.13	8.35
Core volume (mm^3)	7 630	17 300
N87 loss at 200mT 100kHz (kW/m^3)	7 630	7 630
Core losses at rated current (mW)	58	130
Winding window area (mm^2)	40	60
Packing factor (to accommodate bias windings also)	0.2	0.2
Single turn copper CSA (mm^2)	3.17	6.39
Length per turn (m)	4.8	4.8
Total length, for *n* turns (cm)	60	45
Resistance (mΩ)	3.21	1.18
Winding loss (mW)	13	4.7
Core loss (mW)	58	130
Total loss (mW)	71.0	136

Table 5-2: A sample from the saturable inductor design process spreadsheet

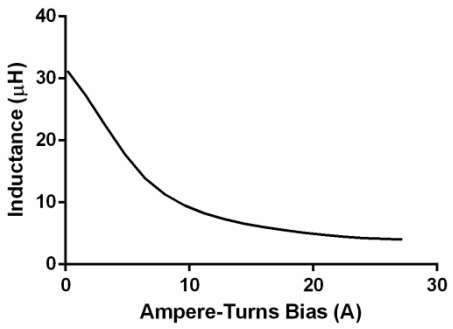

Figure 5-14: Variation of compensation inductor with increasing Ampere-Turns bias (160 turns total bias winding)

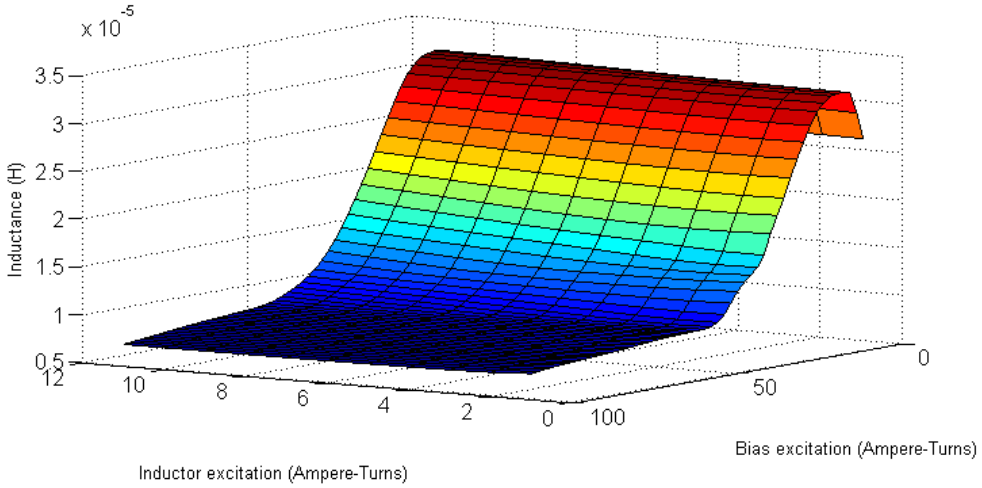

Figure 5-15: A surface plot showing the response of the inductance seen in the primary coil of the saturable inductor in response to current in the bias windings and in the primary coil itself generated from finite element analysis

5.5.3 - Zero-ripple control with the saturable inductor

To ensure zero-ripple operation over the operating range of the converter the compensation inductance, L_3, must be dynamically varied. Ideal behaviour of a SEPIC converter stipulates voltages V_1 and V_2 will be constant . Deviations from ideal behaviour will be present in a real circuit due to parasitic elements and due to manufacturing tolerances, for example, the turns ratio and coefficient of coupling between the coils. Voltage imbalances will be caused by current flowing in parasitic elements such as internal resistance of the coils and are thus dependent on the power supplied from the PV module and will not be static throughout the course of operating of the converter.

A proposed dynamic zero-ripple tracking scheme, similar in structure to a MPPT scheme, using the compensation inductance as the control input to the system and sensed current ripple as an input to the controller. To avoid altering the dynamics of the converter significantly, the time required to 'null' the ripple is chosen to be much slower than the cut-off frequency of the converter. A flow chart for the desired behaviour of the compensator is shown in. The algorithm forms a hill climbing method for the minimisation of ripple in terms of the bias winding current parameter.

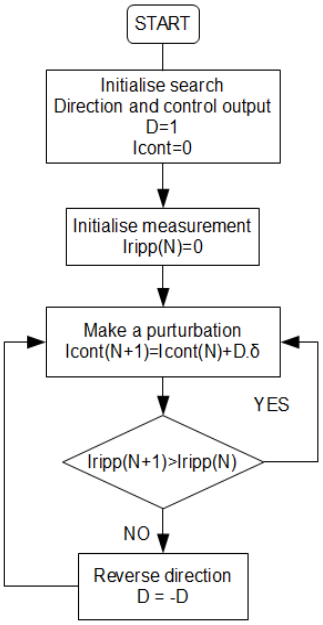

Figure 5-16: Control mechanism for zero-ripple, reminiscent of a perturb and observe algorithm

5.6 - Results

Shown here in Figure 5-17, Figure 5-18 and Figure 2-1 are cases of the input ripple current to the prototype SEPIC converter, when supplied with a variable voltage source. The cases are shown for extremes of operating voltage for a PV module. For each case, the ripple current is shown for an insufficient, excess and adequate value of compensation inductance provided by the saturable inductor.

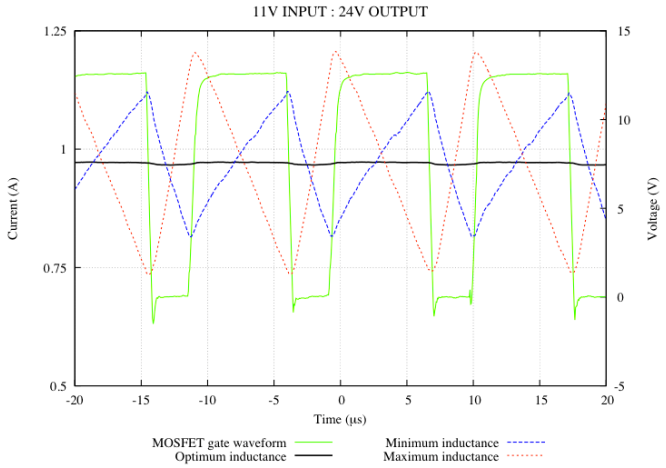

Figure 5-17: Input current ripple waveforms for 11V input 24V output

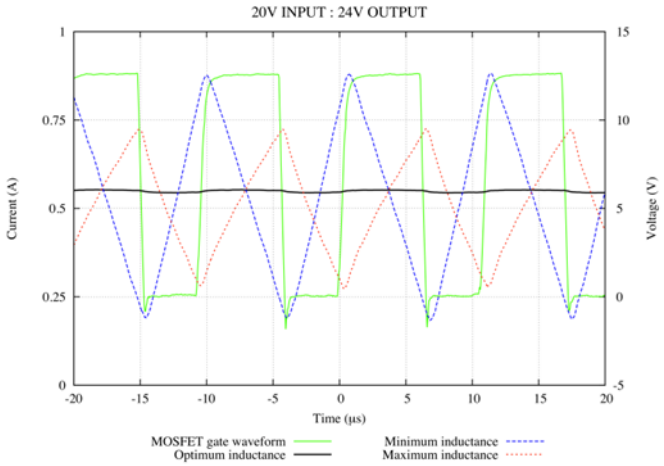

Figure 5-18: Input current ripple waveforms for 20V input 24V output

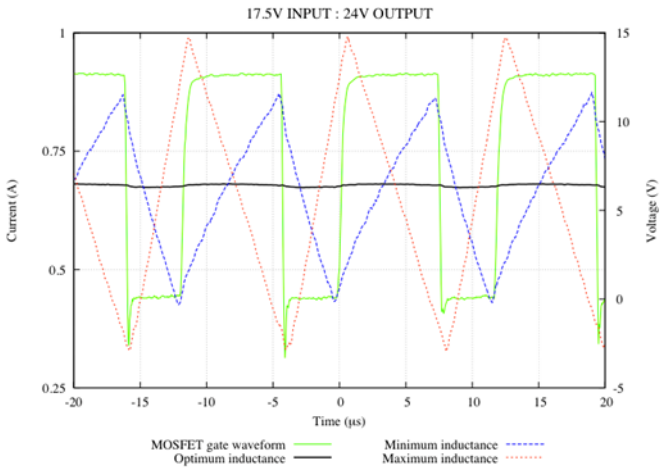

Figure 5-19: Input current ripple waveforms for 17.5V input and 24V output

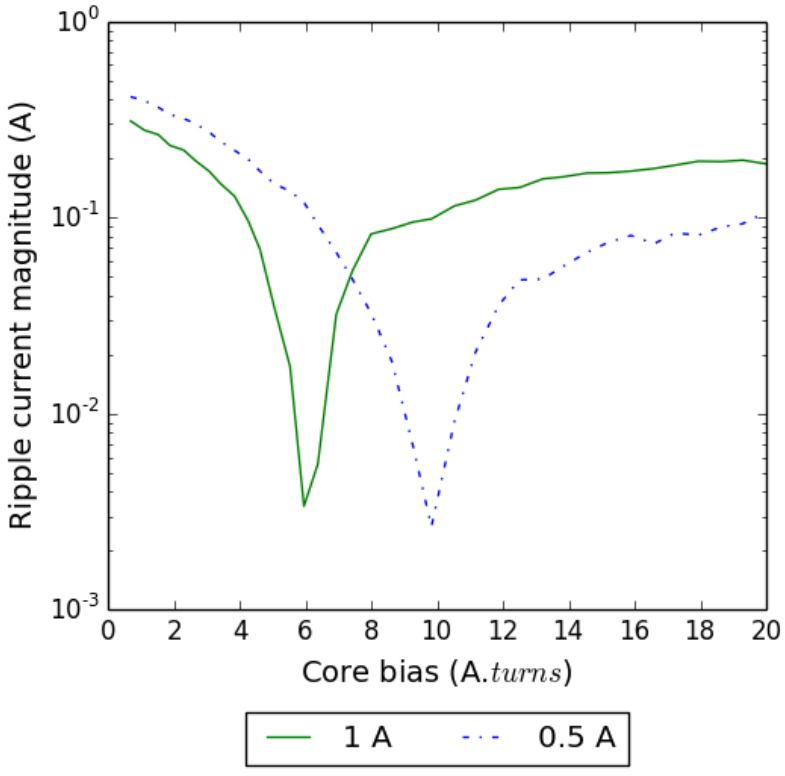

Figure 5-20: The variation of input current ripple with varying core bias. This shows that for the two cases, 0.5 A and 1 A input DC current, there is required two different values of compensation inductance.

Shown in Figure 5-20 is the variation in the input current ripple with changing core bias. This demonstrates that for different conditions of input current a different compensation inductance is required to minimise the effects of stray voltages (parasitic effects) due to different input currents.

The results here show that for each of 11 V, 17.5 V and 20 V input to the SEPIC converter there exists an inductance within the range of the variable inductor which can provide sufficient compensation to the losses in the circuit to reduce the ripple current to negligible levels. In this case, the minimum value of ripple is in the order of 1 mA. Specifically, for the 1 A and 0.5 A case they are 3.1 mA and 2.5 mA respectively.

5.7 - Chapter Conclusions

This chapter has shown the design, construction and evaluation of a SEPIC converter modified to provide low ripple over a wide range of input voltages and currents. The modes under which the ripple voltage strays from zero has been found to be different based upon an imbalance of voltages on the coupled inductors, the solution for this is to provide a low loss method of correcting this imbalance. The design presented here utilises a variable inductor to correct the balance of voltages. The variable inductor has been previously discussed in literature for impedance matching for situations where operation at or near resonance is important, for example, induction heating. Results have been shown for this application demonstrating that this method provides the sufficient improvement towards the improved transfer efficiency conditions (either increased frequency or decreased ripple) discussed in Chapter 4.

The solution presented in this chapter shows one method by which a special optimisation or alternative power converter topology can be used to mitigate the problem of reduced transfer efficiency. The problem of reduced transfer efficiency was discussed in Chapter 4 and it was demonstrated that operation at improved transfer efficiency conditions impacted negatively upon the efficiency of the power converter. The saturable inductor method shown in this chapter, used to restore the zero ripple condition requires power to be dissipated in the bias windings. This will have

an impact on the total efficiency. Considering the results of Chapter 4, specifically, Figure 4-19, the increase in transfer efficiency in moving from 400 mA ripple to 3 mA ripple represents a near 2% increase, from 98% to almost 100%. The efficiency of the boost converter considered at that operating point is 93% which is the minimum efficiency of the proposed SEPIC converter before it can be considered the optimum solution. The case presented in this chapter has been designed for low power, 40 W easily. The design for 40 W was decided upon for the ease with which a repeatable PV source could be set up in a laboratory setting. Further investigation of actual transfer efficiency and full system efficiency is recommended for further work.

Chapter 6 - Reuse of ATX Power Supplies by repurposing for PV applications

Previous chapters have dealt with the design and optimisation of power converters for PV applications. All of the previous mentioned solutions require the construction of dedicated hardware. Some applications, in particular the generation of electricity in developing countries, requires a solution that does not require as much specialist expertise. For these kinds of applications, not only the cost of specialist hardware but also the expertise required for its production form a block to the adoption of such technologies in developing countries. This chapter therefore proposes a method by which minimal specialist hardware must be developed in order to produce a MPPT capable PV battery charger.

This section deals with developments made in the understanding of the requirements and challenges in the reuse of computer power supplies for PV applications. Generally, reuse falls into two categories, returning the whole unit to operation in its original function or, use the use of the whole or part of the system in a different function. This Chapter specifically targets the use of ATX power supplies, that are commonly used in personal computing equipment [100]. This can be performed in a number of ways. First, the reuse of the computer with power supply as it arrived for recycling; this method does not work if either the power supply or the computer unit arrived in a non-working condition. Secondly, reuse by new combinations of computers or power supplies to make a single working computer. Alternatively the power supply can be reused for a purpose other than it was originally intended. This has been seen in colloquial cases where computer power supplies have been reused as laboratory power supplies and for mobile-phone charging.

The scope of the work presented here is primarily to reduce the number of power supplies dispatched for the final stages of recycling. The final stages recycling typically involve the extraction of precious and hazardous materials, this is performed to enable the remainder can be disposed of by

classic landfill methods. Destructive recycling is usually performed regardless of the operational status or remaining operational life of the power supplies. The process of recycling itself does not generate any net revenue, money flows from those initiating the recycling process to those performing the process, small gains are to be had from the sale of extracted commodities, but generally, money is only made on the cost of the service of collection and processing [74]. Furthermore, the disposal of WEEE is in essence an unsustainable process as a large quantity of non-recyclable material is produced and once the hazardous material is dealt with effectively, economic powers dictate how the remainder is dealt with, whether it be by landfill, incineration or an alternative processes.

There already exist community centric schemes revolving around the reuse of redundant IT equipment. An example of these companies, based in Sheffield, is Aspire [101]. Companies such as Aspire perform a free-of-charge collection of WEEE and resell reusable electronics at heavily discounted prices so long as they require minimal servicing and repairs. The majority of this function is paid for by money gained from precious metals released by recycling and the minimal sale price of serviceable equipment. These such systems can easily operate with subsidised premises, charitable tax benefits and volunteer labour, and as such do not scale for wide spread implementation.

Repurposing forms an alternative route to recycling and the like-for-like reuse as previously mentioned. Repurposing encompasses both the reuse of both components from within the power supply, and the modification of the power supply to perform alternative functions. In general, repurposing, is characterised by the reuse of the power supply hardware for purposes outside of its original functional envelope. The functional envelope for an ATX computer power supply is, *a power supply which transforms power from a mains electricity source to the range of DC voltages demanded by the ATX specification* [100]. The ATX specification is a standard originally introduced by IBM to permit widespread and diverse production of power supplies for PC components produced to an IBM specification.

Discussed in this chapter is the potential for repurposing of power supplies for PV applications. These applications are primarily targeted towards developing countries. The term ‘developing

country' is a label defined by the International Monetary Fund to describe a country characterised by a lower than average standard of living, poor infrastructure and little industrial base. Developing countries, in general, rely heavily on portable and self-contained electricity generation due to lack of electricity distribution infrastructure between communities. These communities would typically rely on generation and lighting by means of diesel generators and kerosene lighting. Persistent reliance on consumable commodities, such as oil, places a great burden due to lack of economic sustainability. Economic sustainability may never be obtained in these communities due to scarce resources and many other reasons beyond the scope of this thesis.

6.1 - Introduction

The 2004 EU Waste Electrical and Electronic Equipment directive (WEEE) intended to make manufacturers of electrical and electronic equipment responsible for the collection of waste equipment and their recycling. Driven by modern software and technical demands of IT equipment the ever increasing rate at which IT equipment is exchanged means that non-defective hardware is frequently disposed of. Some schemes have been operating to provide a second life for such redundant equipment through donations to charitable organisations. Computer Aid International, for example, has reused 200,000 computers to date. In contrast, the primary goal of recycling is the reclamation of precious metals and the safe disposal of harmful materials. The process of recycling, in general, does not retain useful components for reuse. This process currently forms a highly optimised system offering the current most economically viable process of disposal. The majority of components within a PC are very specific and interface requirements means it reuse is a non-trivial task. Computer power supplies and their components, however, are subject to standardisation and so are more generic, they could be more readily reused or repurposed given the correct infrastructure. In 2012 it was projected that worldwide sales of PCs (desktop, mobile and tablets) will be in the order of 390M units, with approximately 12M desktop PCs being sold in the UK. In 2009 it was estimated that 14,600 tonnes of waste electrical and electronic equipment was collected from the UK business sector, with IT and telecommunications equipment being the largest contributor accounting for some 5,900 tonnes.

Consequently, significant scope exists to improve the UK's recycling/reuse in this area while creating an opportunity for a new industry to operate alongside the current reuse and recycling practices.

In this work, two potential methods by which a PC power supply can be reused by reconfiguring as Maximum Power Point Tracking PV battery chargers are examined. Although literature exists on the design of PV MPPTs, minimal research has been undertaken on the reuse of existing power converter modules for deployment within PV converters. This chapter presents an analysis of the fundamental blocks of a standard ATX compliant power supply and presents an investigation into how compliant PSUs can be interfaced with MPPT controllers to form useable systems with the intention of proving the technical viability of power supply reuse in this field.

Maximum power point tracking is essential for the maximally efficient operation PV installations by ensuring the output load condition is always matched with the MPP condition of the PV module. In this work, a perturb and observe method (P&O) [15] has been implemented on a microcontroller and interfaced with the PFC boost converter and a combined PFC boost converter and half-bridge converter from an ATX compliant switched mode power supply, to form a MPPT PV interface for battery charging. Results are shown for the operation of the ATX power supply under a full load range and gate drive duty cycle range under MPPT control to determine the operational range over which this system can be effective. Further to these results, the full tests of the MPPT ability of the system are shown.

6.2 - The availability of reusable material

For resale in European countries it is a requirement that power electronic and electrical equipment meets with requirements of electromagnetic compatibility (EMC) [92]. EMC regulations demand that a power supply has minimal effect on its power source so to avoid interference between equipment. Active power factor correction (PFC) provides a means by which the heavily distorted full-wave rectifier input currents drawn from the mains can be corrected to a close approximation of a sine wave. Many older power supply units did not possess active PFCs and a manual changeover switch to allow

the user to select 110 V or 230 V operation, where a voltage doubling rectifier is switched in or out as required. The EMC directive was initially formally enacted in 1995 [100] and has seen a steady increase in its stringency of regulation and power of enforcement, most noticeably in 2009 where greater restriction on electronics imported from countries outside the scope of the European EMC directive was imposed [54]. More modern power supplies feature an active PFC circuit to ensure a unity power factor, sinusoidal current is drawn from the supply, which in turn means there is no requirement for manual change over for 110 V or 220 V operation, as the PFC boost stage is designed to operate over the common world input voltage range of 90 V to 250 V. Active power factor correction is discussed in more detail in section 6.4 - where the suitability of active PFC power stages for reuse is examined.

6.2.1 - Common power supply structure

A number of common features have been identified amongst a small sample of 20 power supplies investigated initially. A degree of design maturity has brought with it a number of common design features. The majority of common power supplies are designed first with the ability to achieve the design requirements and secondly with a focus on cost reduction. With minor differences in the exact implementation, initial work has revealed that regardless of manufacturer, all power supplies studied contain a half-bridge power converter stage used to drive a power transformer. In addition, the transformer by means of a number of 'taps', produces the range of voltages required.

Large design changes bring with them changes to the production line, implementing these changes requires both down-time and human interaction, both of which are costly to the manufacture, and as such in most cases it is cheaper to temporarily introduce the production of add-on boards and systems than to amend the main circuit board in a power supply. In the case of the introduction of active PFC, it was with the introduction of a daughter-board to provide the initial power stage which was later incorporated into the main board in more modern designs. The same is seen in older power supplies where the 3.3 V rail is either provided as supplementary supply, or by means of a mag-amp converter

powered by the existing 5 V rail. In the majority of modern power supplies, most of these elements are standardised and use a dedicated 3.3 V transformer tap.

Figure 2-1 shows a schematic of the common elements which are present in the modern power supplies investigated. The elements shown in Figure 2-1 are representative of the sample studied, regardless of manufacturer or precise model. Between models, only small variation in component ratings and values occur. Primary side, also known as off-line switched power converters operate on the mains side of the isolation transformer. These are common to reduce the number of isolating interface components between the primary and secondary (isolated) side. Gate drive for the main half bridge converter is provided by means of push-pull switching waveforms generated by the supply controller. The gate driver transformer, driven in this push-pull configuration, produces an alternating sequence of positive and negative gate drive pulses on its secondary. These are converted to the required positive pulses, separated by 180 degrees phase shift by alternating the polarity of one the two secondary windings on the gate drive transformer. This is a further cost reduction mechanism, and is representative of one of only a small number methods by which this can be effected with minimal components.

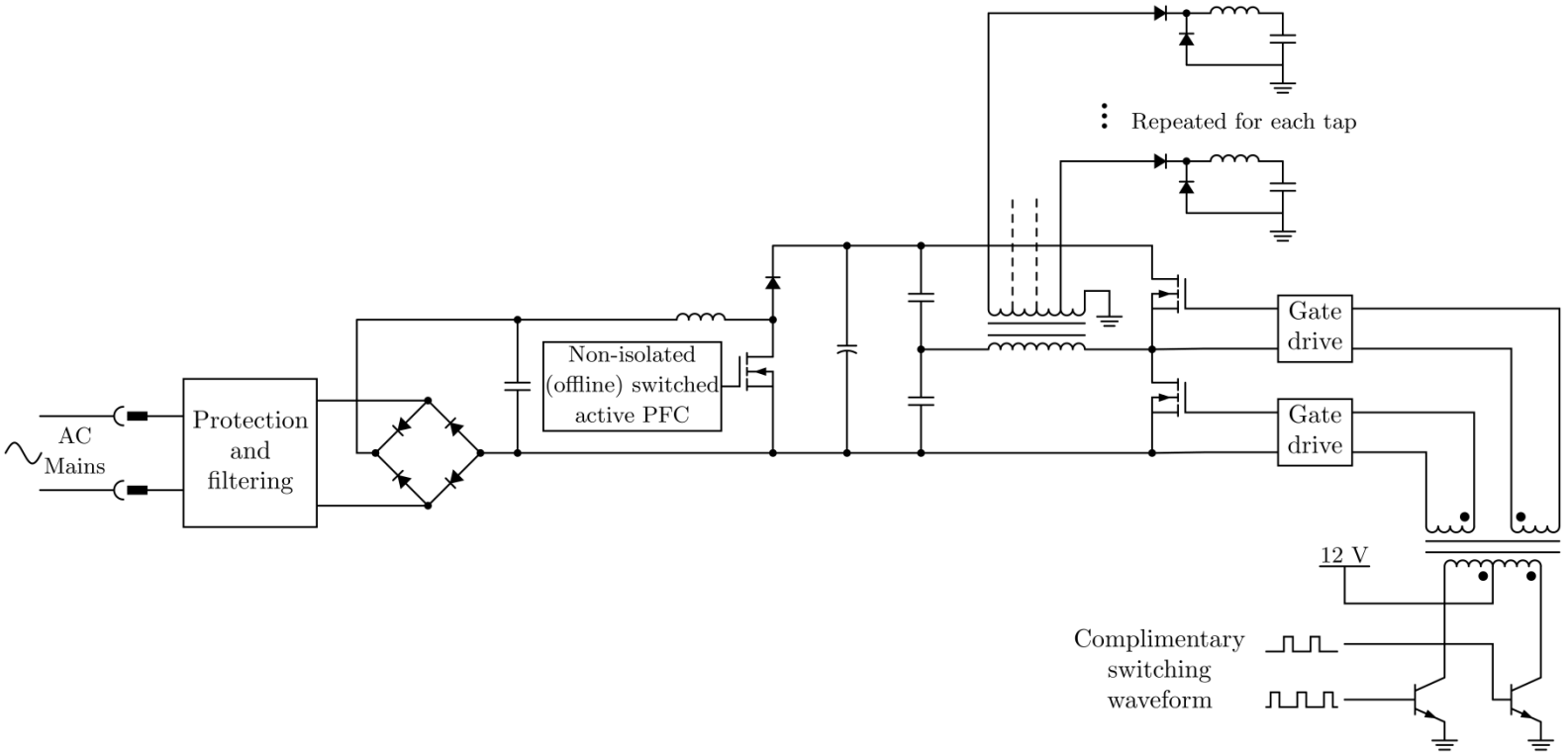

Figure 6-1: A simplified schematic of an ATX power supply with active power factor correction frontend

6.2.2 - Valuable components for reuse

The exact nature of the components was not required for the work performed for this chapter and as such only a short overview of the components is provided.

6.2.2.i - Switching transistors

A quantity of switching transistors, commonly MOSFETs are required for the switched mode power conversion. A minimum of three are required, two for the half-bridge and one for the active PFC front end. These are high voltage, low current, optimised models.

6.2.2.ii - Diodes

Two diodes are required per output voltage, these are low voltage, high current optimised models. A further high voltage and low current optimised diode is provided for the active PFC front end.

6.2.2.iii - Transformers and inductors

A high valued inductor (> 1 mH) is required in the active PFC front end because of the high voltage and low current ripple requirements. The output voltages are commonly smoothed by coupled inductors shared between multiple output voltages as to reduce the cost compared with dedicated magnetic cores for each inductor.

6.3 - Reuse strategies

6.3.1 - Multi-stage reuse

The structure of the power supply as previously shown could lend itself to becoming a complete MPPT-PV power supply capable of producing the necessary supply voltages for the operation of a PC or any other devices compatible with the voltages provided by ATX supplies. For a modified ATX supply to operate successfully in this manner, an additional power supply would be required to source or sink the required surplus or deficiency of power generated by the PV during the MPPT cycle in

order to ensure continued operation of the attached devices whose power demand is not necessarily equal to the MPPT power sourced from the PV array. This regime is demonstrated by Figure 6-2, power flow is indicated by the arrows, the front end PFC is unidirectional, as is the bulk power module (PM), an additional bidirectional power converter is required to provide regulated output voltage.

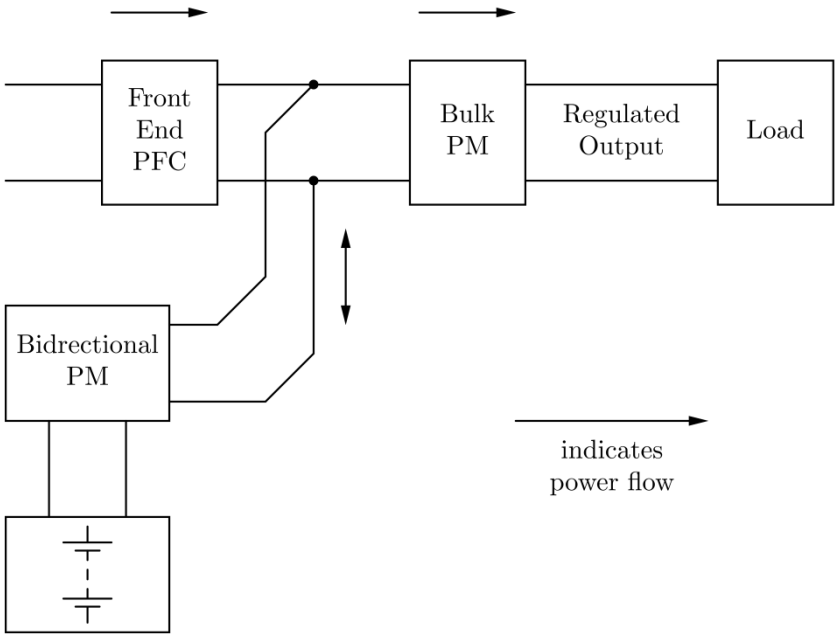

Figure 6-2: A multistage reuse regime where an additional bidirectional power converter is used to source or sink during power surplus or deficiency.

It is possible, however, to use the low voltage output of an ATX supply for the charging of 6 V (3 cell) lead-acid batteries. In this approach the PWM control to the step-down bulk power module is modified to a fixed duty-cycle. The duty-cycle provides a constant step-down from the DC bus voltage to the battery voltage connected on the output. MPPT is performed using the PFC boost converter. This regime is shown in Figure 6-3.

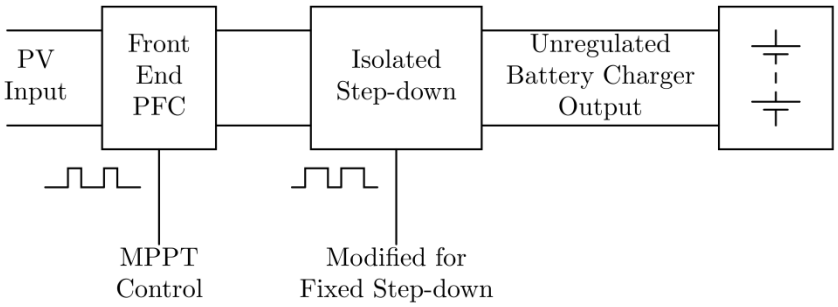

Figure 6-3: A multistage reuse regime intended for low voltage battery charging, only the unidirectional PMs within the computer power supply are required.

6.3.2 - Single-stage reuse

6.3.2.i - Bulk Power Converter

The bulk power converter module has been designed and optimised specifically for operation at either rectified 240 V_{ac} or the result of a voltage doubling rectifier on 110 V_{ac} and as such can only operate on a very narrow range of voltage. This makes the use of this module unsuitable for low voltage PV applications, however, the module could be applicable for use in higher voltage, multi-PV-module array installations.

6.3.2.ii - Front end PFC converter

In this case, the front-end PFC converter is used directly as a boost converter. The boost converter can be readily isolated from the remaining circuit by breaking traces. Direct control by an external gate-driver can be employed to interface from the MPPT controller.

6.4 - Operational limits of the PFC

A simplified diagram of this action of the power-factor correction (PFC) controller is shown in Figure 6-4 to demonstrate the original application for which the converter was defined [97], [102–105]. A rectifier circuit operates over a limited conduction angle when used to charge a reservoir capacitor. This matter is shown in TOP: the case where there is no active power factor correction

MIDDLE: the ideal waveform for a power supply with active PFC
BOTTOM: the realistic case for active power factor correction

Figure 6-5, which from top to bottom shows the current waveform for a large capacitor, for zero capacitance and for a modest/small capacitor. Classic power converters rely on a smooth rectified DC voltage without power fact correction. This extreme distortion of the current waveform prompted the introduction of active PFCs to minimise the effects of this distortion on the mains power supply. Ideally, an active power factor corrector should be able to operate over full cycle conduction on a full-wave rectified sine-wave, in practical terms this is not possible (the low voltages require extreme step-up ratios) and a compromise between an acceptable distortion and lower operating limit of the boost converter must be achieved. This matter is highlighted in TOP: the case where there is no active power factor correction

MIDDLE: the ideal waveform for a power supply with active PFC
BOTTOM: the realistic case for active power factor correction

Figure 6-5. In the case where there is no active power factor correction, the capacitor voltage must be made relatively smooth DC to in order to maintain a DC bus voltage that is always within the minimum/maximum bounds for the bulk power converter input, this requires a large filter capacitor and as such there is very distinct distortion in the current waveform. The ideal waveform presented in TOP: the case where there is no active power factor correction

MIDDLE: the ideal waveform for a power supply with active PFC
BOTTOM: the realistic case for active power factor correction

Figure 6-5 demonstrates the desired characteristics, the current is directly proportional to the input voltage, minimal distortion and noise is produced by the power supply. This idea case does however, require the active PFC to be able to operate from 350 V input down to zero, this is unachievable in practice. The realistic case in TOP: the case where there is no active power factor correction

MIDDLE: the ideal waveform for a power supply with active PFC
BOTTOM: the realistic case for active power factor correction

Figure 6-5 strikes a compromise between the input distortion and the operating span of the PFC converter. A common minimum voltage of approximately 50 V is used a minimum when stepping up to approximately 400 V, a 1:8 step-up ratio.

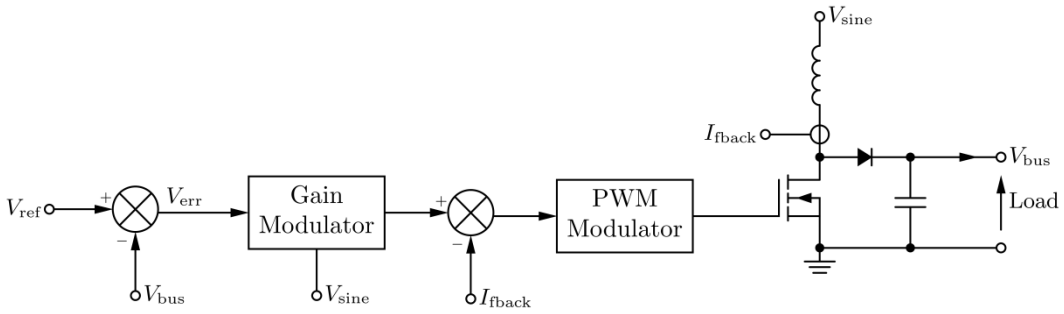

Figure 6-4: A simplified flow diagram of an active PFC control method that would typically be employed by an active PFC control chip.

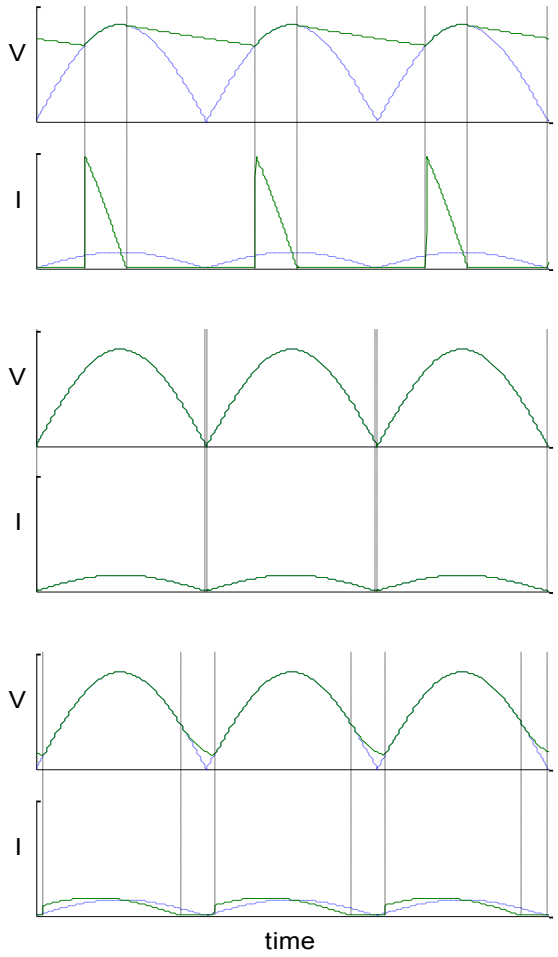

TOP: the case where there is no active power factor correction
MIDDLE: the ideal waveform for a power supply with active PFC
BOTTOM: the realistic case for active power factor correction

Figure 6-5: Rectifier-capacitor design compromises based on the operational limits of the PFC boost converter.

6.5 - Reuse case study – a prototype PV battery charger

6.5.1 - Single stage reuse – the PFC front end

This method involves the direct reuse of the active power factor correction front end unit. This power stage is a boost converter and is designed to operate over a 50 V to 350 V input range with a constant DC output greater than the maximum input and typically around 400 V_{DC}.

The candidate power supply was initially selected and the boost converter, which in this case was found to be a discrete module, is removed and studied prior to implementation as a PV battery charger. The study involved the estimation of the circuit's operational limits with particular focus on the range over which it would ideally be used. For the primary power source a 40 W PV module was selected. The 40 W module is the same as previously discussed in other chapters, and is of moderately low price and is easily transported; which would be suitable for a remote installation providing power for a small load. These factors make the 40 W module ideal for the potential target application of remote power in remote areas of developing countries.

A PFC boost converter was reclaimed from a 350 W ATX power supply manufactured by FSP Group to be used as a PV MPPT battery charger. A photograph of the reclaimed PFC module is shown in Figure 6-6.

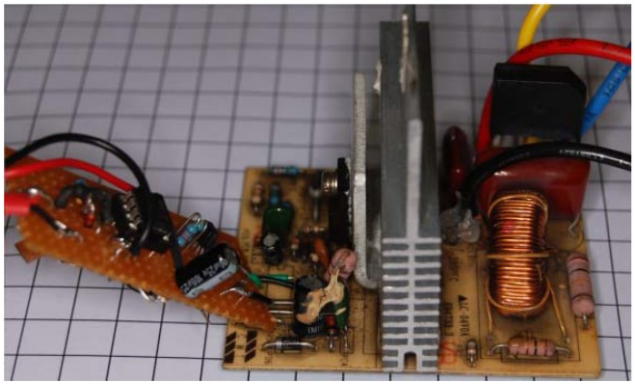

Figure 6-6: The PFC module used for the prototype MPPT battery charger.

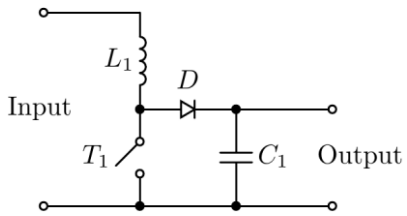

Figure 6-7: A simplified schematic of the PFC boost converter.

The PFC module was based on the boost converter topology; a (simplified schematic is shown in Figure 6-7. An ICE2PCS02 dedicated PFC controller IC was used to control the main switch T1 (n-channel MOSFET) using PWM to perform wave shaping on the power supply's input current. To utilise the boost converter for MPPT battery charging, only a PWM gate drive signal needs to be applied to the module with the control chip disconnected. To achieve this, the dedicated PFC controller was removed from the module and replaced with a MOSFET gate driver. This provides the necessary isolation and level shifting to interface the MPPT controller-PWM output to the module. This modification can be seen on the prototyping board to the left hand side of Figure 6-6.

The primary inductor in the PFC module (L_1) was implemented by the manufacturer as 66 turns of 0.78 mm^2 solid copper wire on a toroidal core (with a magnetic cross section area of 0.5 cm^2). An in-circuit measurement of inductance using a LCR meter showed that the inductance was approximately 500 µH. The reluctance of the core can be calculated using (6-1).

$$L[H] = \frac{N^2}{S[H^{-1}]} \Rightarrow S[H^{-1}] = \frac{N^2}{L[H]} = \frac{66^2}{500[\mu H]} = 8.71 \times 10^6[H^{-1}] \qquad (6\text{-}1)$$

Where: L is inductance (H)

S is the core reluctance (H^{-1})

N is the number of turns

Without performing an invasive test, it is not possible to estimate the inductor saturation limits because the core material remains an unknown. If it is assumed that the material is a variety of ferrite and 300 mT is a plausible saturation limit (ignoring any safety margin). This estimate of 300 mT is used to determine an approximate saturation current for the inductor using (6-2). This calculation gives the value of 1.98 A which is consistent with the full load operating current that is $\frac{350\text{ W}}{240\text{ V}} = 1.46$ A.

$$\frac{\Phi_{max}}{A} = 300\ mT < \frac{NI}{SA} \Rightarrow I_{max} < \frac{\left(\frac{\Phi_{max}}{A}\right) SA}{N} \qquad (6\text{-}2)$$

Where:

Φ_{max} is peak magnetic flux (Wb)

A is the core cross section area (m^2)

S is the core reluctance (H^{-1})

I is inductor current

I_{max} inductor current at onset of magnetic saturation of the core

N is the number of turns

The aforementioned 40 W PV module, used for the practical evaluation of the system, is a nominally 40 W silicon PV module. The voltage range of this module under normal operation is 7 V to 22 V, the output current for the test conditions within this investigation is between 0 – 2 A. For an output voltage range of 24 V to 28 V (two series connected lead acid batteries) a PWM gate drive duty cycle range of 8% to 75% is required. For this investigation the original switching frequency of the PFC controller is retained at 45 kHz and the same inductor and capacitor are used. To verify the suitability of the PFC repurposed as a PV MPPT its operating characteristics were examined by varying both duty-cycle and load for a range of DC input voltages (5V to 30V) to emulate a typical 24 V PV module under general operation. Figure 6-8 shows the PFC boost converter behaves as expected following the typical characteristic voltage gain for duty cycles below 75%. Above this value the output voltage reduces due to the onset of saturation in the inductor core and this restricts the maximum battery voltage that can be accommodated.

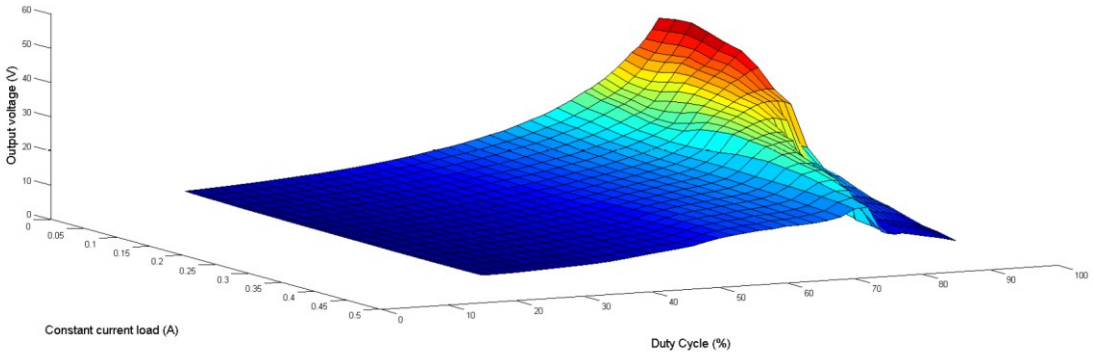

Figure 6-8: Experimental load and duty cycle characterisation of the reclaimed PFC boost converter, the maximum possible step-up ability of the converter is indicated by the ridge most dominant at high duty cycle and high load current.

Based on these results an MPPT converter was built around an ATX PFC boost converter. MPPT is achieved with the hill-climbing algorithm which was implemented on an Atmel ATMega328 microcontroller, shown in Figure 6-10. To evaluate the performance of the proposed PFC-based PV battery charger the nominal artificial illumination provided by four 500 W halogen lamps provided illumination were used to illuminate the 40 W (V_{oc} = 21.5 V, I_{sc} = 2.64 A) PV module connected to charge two series connected 12 V 50 Ah valve regulated lead acid batteries via the proposed MPPT converter. A block diagram representation of this set-up is shown in Figure 6-9. The variation in illumination was achieved by selectively switching off/on two of the halogen lamps to effect a sudden change in illumination.

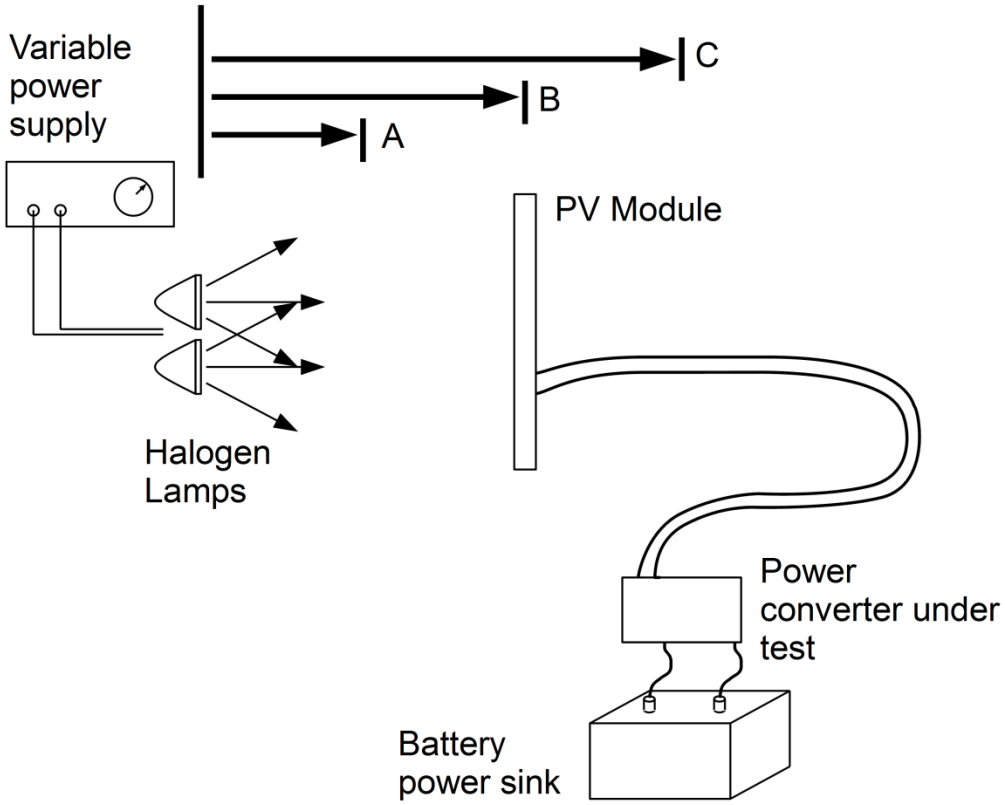

Figure 6-9: Block diagram of MPPT test-rig, the three lamp-panel distances (A, B and C) used for tests are shown offer coarse variation in illumination and the variable power supply offers gradual variation in illumination.

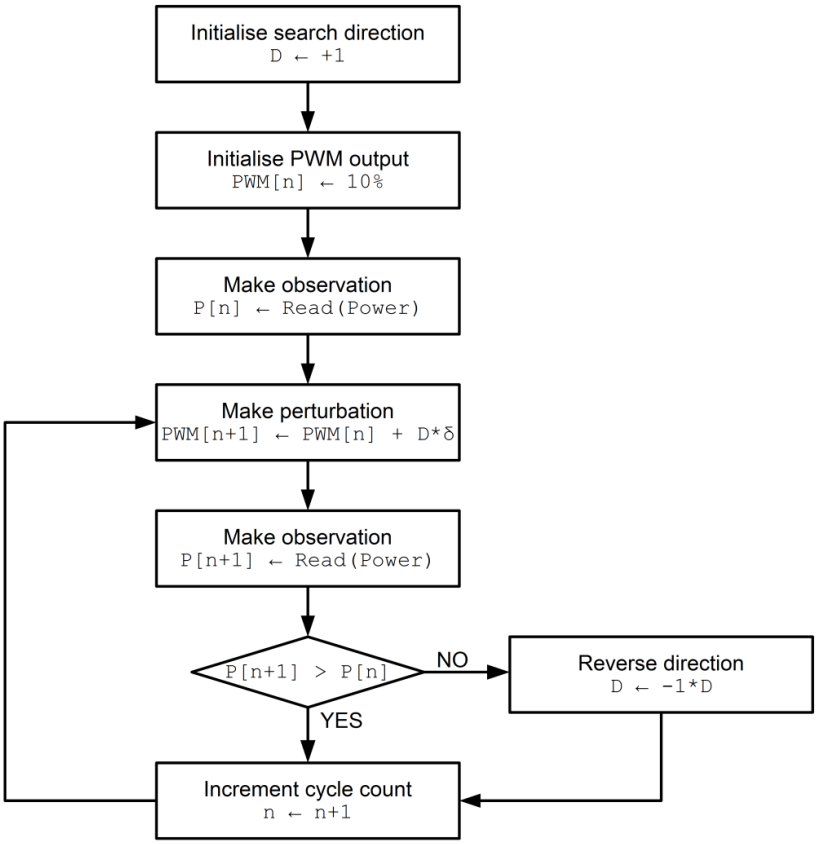

Figure 6-10: Flow chart of the hill climbing MPPT algorithm [8]

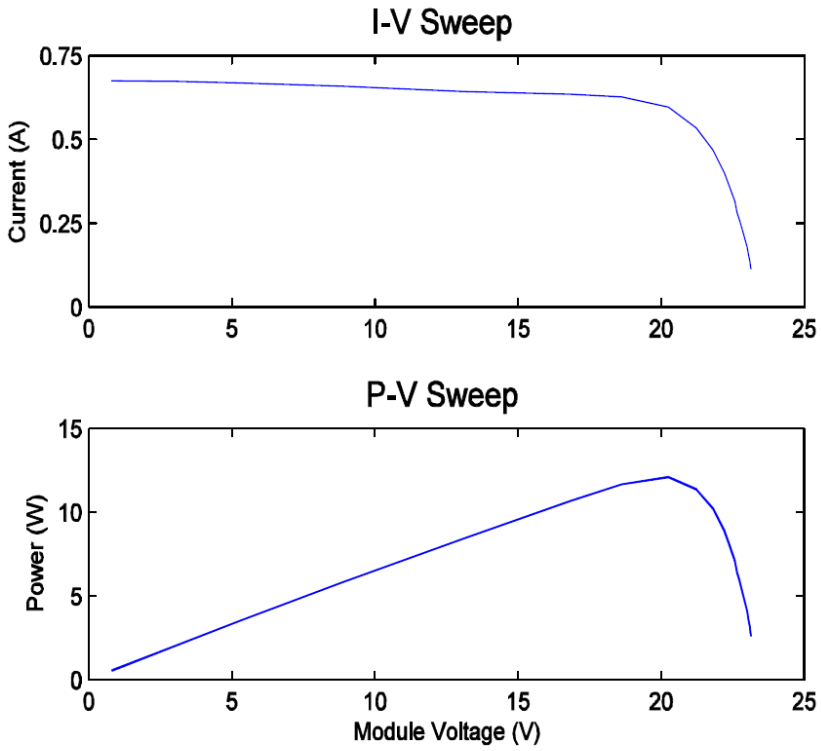

Figure 6-11: I-V and P-V sweep of the module used during the test

A controlled load was employed to determine the maximum power point for the PV operating under static illumination at the maximum intensity used. Figure 6-11 shows the voltage-current and voltage-power curves for PV module from this experiment and the maximum power point was found to be 11.83 W at 20.48 V.

To investigate the MPPT ability of the proposed converter, the illumination of the PV module was varied between 965-350 Wm^{-2} by switching on or off combinations of the lamps, Figure 6-12 (upper). As can be seen, the proposed PFC-based MPPT converter follows the illumination level without excessive deviation, Figure 6-12 (lower).

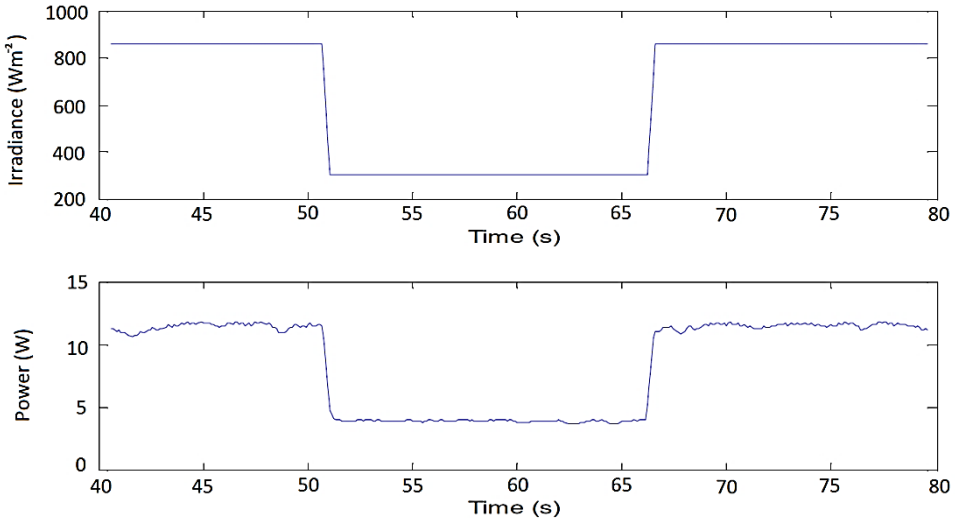

Figure 6-12: The behaviour of the PFC boost converter under MPPT control with PV power source and battery load.

6.5.2 - Multi-stage reuse – the PFC front end and bulk power converter

Extending the previous experiment, involving only the front end PFC boost converter, the bulk power conversion stage is now utilised. Following the ATX standard, the bulk power conversion stage provides voltage of both 12 V and 5 V; these lower voltages are more readily used by external equipment, for example, mobile phone chargers, portable radios and some computing equipment. Furthermore, by utilising a greater proportion of the total power supply the total WEEE output of the production line is reduced.

This experiment is performed with a power supply again manufactured by the FSP group, but this time a FSP300-60GLS. This model has on-board active PFC, but otherwise has near identical structure to the original FSP350 used previously.

The modification to utilise both PFC front-end and bulk power conversion stage involves constraining one of the supplies to operate at a fixed step up/down ratio. This is achieved by

transferring control from both the front-end PFC stage and the bulk PM. In this case, the bulk conversion stage has been constrained to use a fixed duty cycle and the PFC front-end is operated under MPPT control. The MPPT control is implemented on an Atmel ATMega328 microcontroller, the fixed duty cycle output which drives the bulk power converter is also produced by the microcontroller. The output voltage and current are used to measure the charging status the battery and to indicate whether a fault or open circuit condition has occurred. The MPPT algorithm employed is a perturb and observe algorithm, the use of which has been extensively analysed in the literature [5-8]. A flowchart for the control algorithm is shown in Figure 6-10, where the PV array voltage and current are measured to obtain the instantaneous power. The response of the power following a perturbation allows the direction of greater power to be determined.

Resistive potential dividers are used to scale voltage and current signals such that they can be easily read by an ADC on the microcontroller. The switching frequency of both the power converter stages was fixed at 110 kHz, the same frequency that was provided by the original controller for this power supply. Connections were made to monitor internal voltage and current and voltage measurements which were logged by the microcontroller. The input to the power supply used in this experiment is designed for similar operational characteristics as that used in the previous experiment into the real operating range of PFC optimised boost converter.

A series of stepped illumination changes are proposed for the evaluation of the battery charger. The proposed schedule of illumination is shown in Figure 6-14 of the results section. Variations of the power supplied to the illumination source were calibrated against the resulting MPP power under the test conditions. This calibration was performed at constant cell temperature of 30°C which was maintained by forced air cooling. The characteristic curve of the PV module was then measured using a variable resistance load and a pair of HP34401 6½ digit multimeters measuring the module's voltage and current.

Figure 6-13 shows the PV's maximum output power as a function of illumination source's control voltage, Figure 6-14 shows the control voltage profile used to validate the MPPT battery charger;

Figure 6-15 illustrates MPPT's dynamic response and in Figure 6-16 battery voltage under different charging levels is shown.

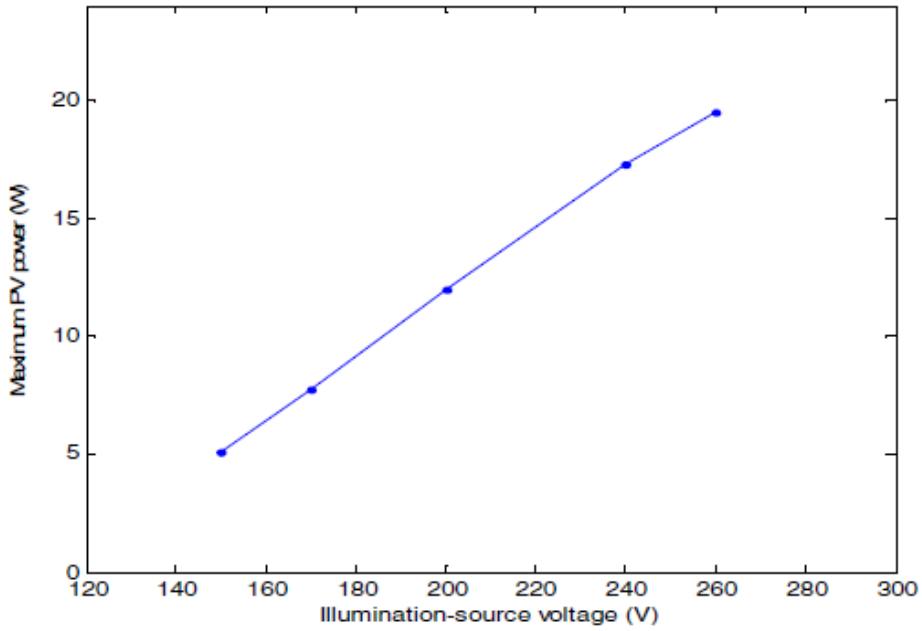

Figure 6-13: A calibration of illumination source voltage and PV output power (MPP conditions)

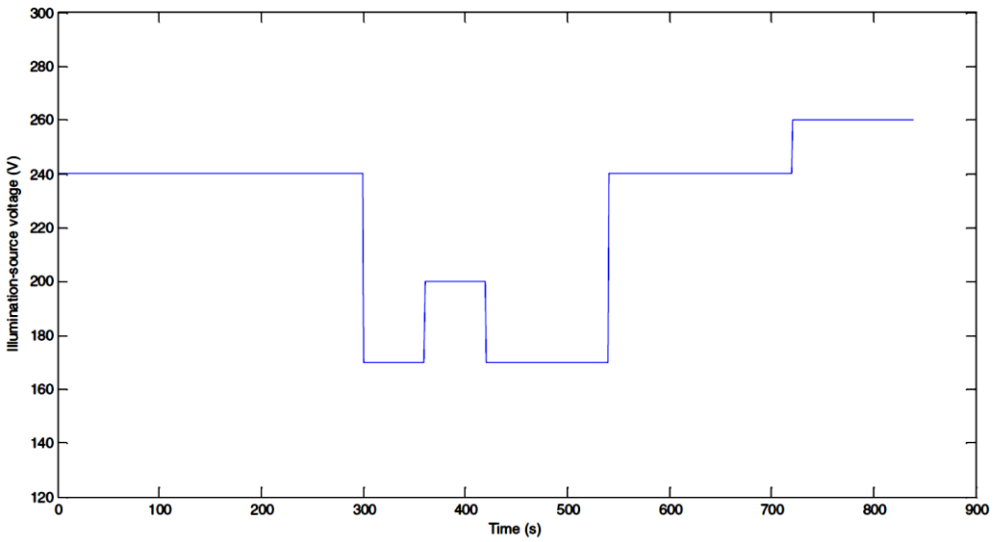

Figure 6-14: The schedule of illumination voltage used for the experiment

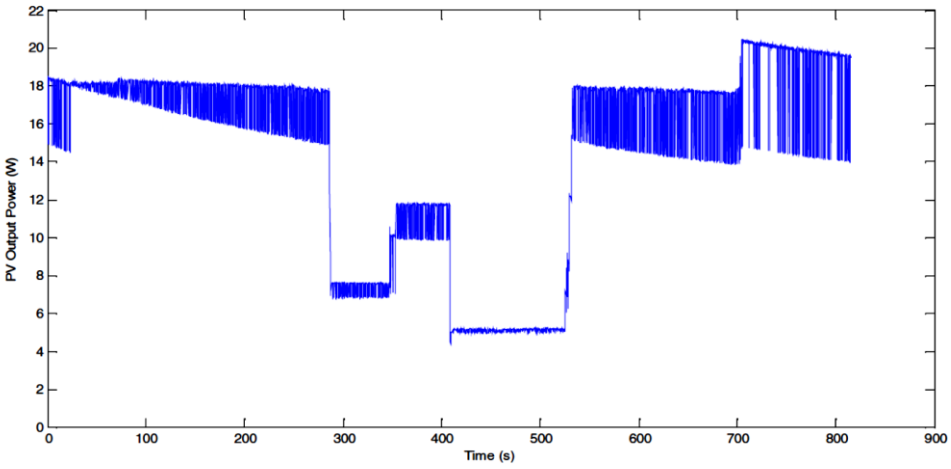

Figure 6-15: Instantaneous power output of the PV module during the MPPT experiment.

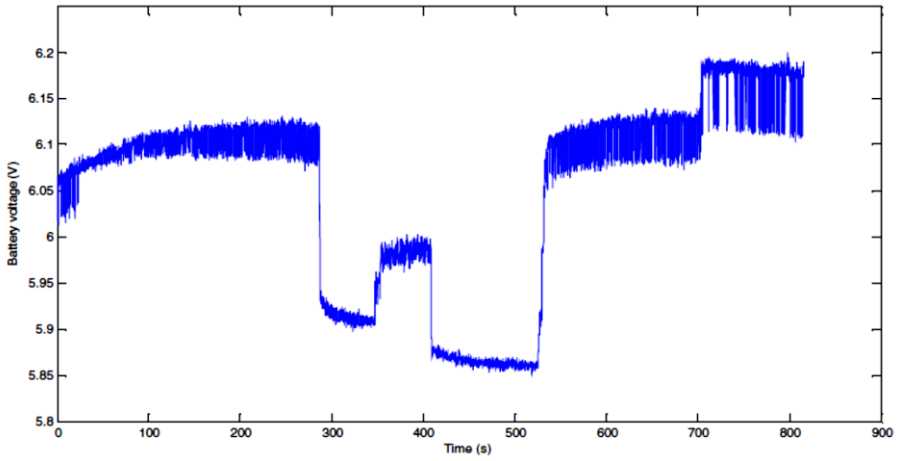

Figure 6-16: The battery charging voltage logged throughout the MPPT experiment, significant reductions are seen as the input power drops, this is due to battery internal resistance. The steady exponential decay during lower power periods is due to battery voltage relaxation.

In Figure 6-15 a number of observations can be made. A peak-to-peak perturbation can be seen superimposed on the static power levels and this is caused by the perturb and observe PPT algorithm hunting for the MPP. Related to this is the variation in the peak-to-peak perturbation level for the different power levels considered. Comparing the MPP level during the period 300-350 seconds to the MPP level during the period 350-400 seconds one may observe a near 3-fold decrease in the peak-to-peak perturbation caused by the MPPT. Furthermore during the period 400-550 seconds the amplitude of MPPT oscillation is almost negligible. These differences can be attributed to the finite resolution of the inbuilt ADC and the corresponding discretization effects that are imposed on PV voltage, current and power curves in the combined PV module/converter system. Furthermore, at input voltages near 20 V, the boost converter is operating at a 1:20 step-up ratio. At extreme step-up ratios, the duty-cycle voltage curve of the boost converter tends to reduce, increasing the non-linearity of the boost converter and adding greater complexity to its characteristic. For any PV module there is a pronounced peak of

the power-voltage curve at MPP. This MPP peak becomes less prominent and at lower insolation levels, thus any deviation from this peak has less effect in the power.

Finally, a pronounced increase in the peak-to-peak perturbation can be seen during higher power levels (i.e. period 30 to 300 seconds and 550 to 700 seconds). The most likely cause for this effect is due to the transient heating caused by IR radiation from the halogen lamps. A disadvantage of the halogen lamp PV testing is that heat is delivered through the PV array glass by radiation and removed by conduction through the surfaces, the discrepancy in these heating/cooling time constants resulting in profound effects at higher input power levels.

The time-plot of the battery terminal voltage shown in Figure 6-16, shows a steady increase throughout the experiment: typical of battery charging. Transient decreases in terminal-voltage are characteristic of a battery terminal voltage relaxing at lower power levels.

6.6 - Conclusions and impact on further work

This chapter has shown two methods by which an ATX power supply can be repurposed for PV MPPT applications. Both of the methods reduce the requirement for additional hardware to be constructed, but does not require the design of a complex power stages as would be required in one of the proposed reuse strategies. Both the results are useable for battery charging, this is beneficial because of the daily variation of PV power, and essential if a power reserve for night-time is required.

The common features amongst differing power supply designs has proven invaluable to the rapid understanding and modification of individual power supplies. With increasing requirement for low cost IT equipment, these levels of standardisation are unlikely to change.

Both methods demonstrated that a power supply can be reused have proven that MPPT performance is possible using the hardware supplied in a conventional ATX power supply. The power supply can be reused with minimal modification and the addition of only an external gate driver. The reduced parts cost of the resultant system can prove beneficial in cost driven applications.

Problems with the use of the low-resolution MPPT controllers and compound effects when the power supplies are used outside of their intended operational range have been shown. This matter warrants further investigation as a distinct advantage may be had in these applications by the use of a more expensive yet higher performance MPPT controller. Furthermore, advanced MPPT algorithms, for example variable step size algorithms, could have an advantage in these applications to reduce the increased power deviations at higher input power.

The reuse of individual components has not been discussed in this chapter but does however present a method by which components can be better utilised for increased efficiency. Whist there are no MOSFETs optimised for lower voltage and higher current applications, diodes form the secondary side of the power supply could be used to replace the higher voltage diodes in the front end boost converter when used for PV applications. Higher voltage diodes tend to have greater bulk resistance and thus increased relative voltage drop when operated at lower voltages and greater average currents, this is not the case with low rated voltage diodes.

Further potential lies in the facility that could be legislated to be included in the design to ease reuse. This could be performed without significant modification to the layout of the power supply and would make reuse a much more economically viable option.

Chapter 7 - Thesis conclusions

This thesis has presented a means by which a high performance PV power interface can be developed. This is achieved through the accurate characterisation of a PV module which can generate model parameters which accurately describe the PV module in the computational domain. The models can be used to facilitate advanced design methods. This characterisation is performed using a novel application of flashed illumination. Flashed illumination is typically used only in rapid evaluation of commercial PV modules post fabrication, however, the method presented here has been adapted for generation of a PV characteristics at high power levels, without the obtrusive heating effect of typical static illumination methods.

The use of an PV characteristic generated in such a method as the flashed illumination has then be utilised in the computational domain for study in the effects of current ripple in a PV module. Experimental validation of this analysis has demonstrated some of the operational characteristics of the SMPC demanded by the PV module for more efficient power transfer. The conditions of sub-optimal power transfer have been compared with a model of boost converter losses. Comparison with the boost converter loss model has shown that the conditions demanded by the PV module for greater efficiency cannot be met with a classical boost converter without severe degradation to the electrical efficiency of the boost converter. It has therefore been demonstrated that in order to maximise the efficiency of power transfer from the PV module, innovative SMPC topologies and optimisations are required.

A novel design for a SEPIC converter, based upon the classic coupled-inductors SEPIC converter, with the addition of an electronically variable inductor has been presented. This systems has been demonstrated to be capable of reaching the zero-ripple condition over the wide range of operating conditions demanded by PV applications. This system can operate at the conditions of high transfer efficiency highlighted in Chapter 4.

A new field of research of reuse and repurposing of redundant equipment has been introduced in Chapter 6. This method removes the requirement for the development of advanced power converters to exploit PV power in developing countries. By removing the barriers to use of PV technology in such areas, it is hoped that this will incite future development and growth of expertise in such areas.

7.1 - Further work

The design of a PV characteristic emulator presents a method by which a module with uniform illumination can be emulated. The characteristic emulated must be changed by the alteration of component values in the circuit. This method can prove cumbersome for the rapid evaluation of PV characteristics applied to a power converter. Work is proposed for the modification of the circuit, including the addition of programmable potentiometers to permit the easy variation of circuit parameters. This could indeed also be modified to provide a hardware-in-the-loop tuning system for component values.

The work presented on the analysis of the effects of ripple current is performed using only a single module under specific environmental conditions. It would be beneficial to the understanding of the methods by which the transfer-efficiency effects can be minimised to establish a dataset based upon a wider range of PV module and under a wider degree of environmental conditions.

Work has been performed on the development of a novel SEPIC converter, that can operate at ideal transfer-efficiency conditions. This method has only been implemented as a small scale prototype. In order to assess the impact of the addition of the bias coils on the efficiency. A prototype of greater power is proposed along with a full efficiency validation to assess the scalability of the sytem in terms of efficiency and power.

REFERENCES

[1] D. M. K. Schofield, M. P. Foster, and D. A. Stone, "Low-cost solar emulator for evaluation of maximum power point tracking methods," *Electronics Letters*, vol. 47, no. 3, p. 208, 2011.

[2] D. M. K. Schofield, M. P. Foster, and D. A. Stone, "Impact of ripple current on the average output power of solar cells," in *6th IET International Conference on Power Electronics, Machines and Drives (PEMD 2012)*, 2012, pp. D43–D43.

[3] D. Rogers, J. Green, M. Foster, D. Stone, D. Schofield, S. Abuzed, and A. Buckley, "Repurposing of ATX computer power supplies for PV applications in developing countries," in *2013 International Conference on Renewable Energy Research and Applications (ICRERA)*, 2013, pp. 973–978.

[4] D. M. K. Schofield, S. Abuzed, M. P. Foster, D. A. Stone, D. J. Rogers, and J. E. Green, "Second life of computer power supplies in PV battery charging applications," in *2013 15th European Conference on Power Electronics and Applications (EPE)*, 2013, pp. 1–10.

[5] D. Rogers, J. Green, M. Foster, D. Stone, D. M. K. Schofield, B. Alastair, and S. Abuzed, "ATX power supply derived MPPT converter for cell phone charging applications in the developing world," in *Proceedings of 2014 The 7th IET international conference on Power Electronics, Machines and Drives*, 2014.

[6] D. Rogers, J. Green, M. Foster, D. Stone, D. Schofield, S. Abuzed, and A. Buckley, "A low cost photovoltaic maximum power point tracking buck converter for cell phone charging applications," in *Proceedings of PCIM Europe 2014*, 2014.

[7] Aristophnes, "The Clouds (play)." 423BC.

[8] R. Williams, "Becquerel Photovoltaic Effect in Binary Compounds," *The Journal of Chemical Physics*, vol. 32, no. 5, p. 1505, Jul. 1960.

[9] A. L. Hughes, "Fundamental Laws of Photoelectricity," *Transactions of the American Institute of Electrical Engineers*, vol. 53, no. 8, pp. 1149–1153, Aug. 1934.

[10] W. Vanselow, G. P. Happ, J. Russell, and S. E. Sheppard, "An Einthoven String Galvanometer-Amplifier System for the Investigation of Photovoltaic Effects," *Review of Scientific Instruments*, vol. 11, no. 6, p. 202, 1940.

[11] M. B. Prince and M. Wolf, "New developments in silicon photovoltaic devices," *Journal of the British Institution of Radio Engineers*, vol. 18, no. 10, pp. 583–594, Oct. 1958.

[12] D. I. Black, "Fabrication of hybrid inorganic and organic photovoltaic cells," Demontfort University, Leicester, 2011.

[13] C. Sah, R. Noyce, and W. Shockley, "Carrier Generation and Recombination in P-N Junctions and P-N Junction Characteristics," *Proceedings of the IRE*, vol. 45, no. 9, pp. 1228–1243, Sep. 1957.

[14] U. Boke, “A simple model of photovoltaic module electric characteristics,” *Power Electronics and Applications, 2007 European …*, 2007.

[15] T. Esram and P. L. Chapman, “Comparison of Photovoltaic Array Maximum Power Point Tracking Techniques,” *IEEE Transactions on Energy Conversion*, vol. 22, no. 2, pp. 439–449, Jun. 2007.

[16] D. P. Hohm and M. E. Ropp, “Comparative study of maximum power point tracking algorithms using an experimental, programmable, maximum power point tracking test bed,” in *Conference Record of the Twenty-Eighth IEEE Photovoltaic Specialists Conference - 2000 (Cat. No.00CH37036)*, 2000, pp. 1699–1702.

[17] H. Patel and V. Agarwal, “MATLAB-Based Modeling to Study the Effects of Partial Shading on PV Array Characteristics,” *IEEE Transactions on Energy Conversion*, vol. 23, no. 1, pp. 302–310, Mar. 2008.

[18] L. Weiping and L. Miaoshan, “Research and application of high concentrating solar photovoltaic system,” in *2012 2nd International Conference on Consumer Electronics, Communications and Networks (CECNet)*, 2012, pp. 1187–1191.

[19] L.-M. Collin, O. J. Arenas, R. Ares, and L. G. Frechette, “Thermal Resistance and Heat Spreading Characterization Platform for Concentrated Photovoltaic Cell Receivers,” *IEEE Transactions on Components, Packaging and Manufacturing Technology*, vol. 3, no. 10, pp. 1673–1682, Oct. 2013.

[20] A. K. M. Zakzouk, M. Electrochem, A. Mujahid, and M. S. El-Shobokshy, “Performance evaluation of photovoltaic silicon cells under concentrated sunlight,” *IEE Proceedings I Solid State and Electron Devices*, vol. 131, no. 2, p. 66, 1984.

[21] S. Poshtkouhi, V. Palaniappan, M. Fard, and O. Trescases, “A General Approach for Quantifying the Benefit of Distributed Power Electronics for Fine Grained MPPT in Photovoltaic Applications Using 3-D Modeling,” *IEEE Transactions on Power Electronics*, vol. 27, no. 11, pp. 4656–4666, Nov. 2012.

[22] C. R. Sullivan, J. Awerbuch, and A. M. Latham, “Decrease in photovoltaic power output from ripple: Simple general calculation and effect of partial shading,” *2011 Twenty-Sixth Annual IEEE Applied Power Electronics Conference and Exposition (APEC)*, no. 1, pp. 1954–1960, Mar. 2011.

[23] N. Femia, G. Petrone, G. Spagnuolo, and M. Vitelli, “A Technique for Improving P&O MPPT Performances of Double-Stage Grid-Connected Photovoltaic Systems,” *IEEE Transactions on Industrial Electronics*, vol. 56, no. 11, pp. 4473–4482, Nov. 2009.

[24] Q. Mei, M. Shan, L. Liu, and J. M. Guerrero, “A Novel Improved Variable Step-Size Incremental-Resistance MPPT Method for PV Systems,” *IEEE Transactions on Industrial Electronics*, vol. 58, no. 6, pp. 2427–2434, Jun. 2011.

[25] T. Esram, J. W. Kimball, P. T. Krein, P. L. Chapman, and P. Midya, “Dynamic Maximum Power Point Tracking of Photovoltaic Arrays Using Ripple Correlation Control,” *IEEE Transactions on Power Electronics*, vol. 21, no. 5, pp. 1282–1291, Sep. 2006.

[26] A. J. Fairweather, M. P. Foster, and D. A. Stone, “VRLA battery parameter identification using pseudo random binary sequences (PRBS),” *Power Electronics, Machines and Drives Conference*, 2010.

[27] T. Takashima, K. Otani, K. Sakuta, T. Yamada, T. Igarashi, K. Hasegawa, H. Wakabayashi, and T. Yamaguchi, “Electrical detection and specification of failed modules in PV array,” vol. 3. pp. 2276–2279 Vol.3, 2003.

[28] W. H. Press, S. A. Teukolsky, W. T. Vetterling, and B. P. Flannery, *Numerical Recipes 3rd Edition: The Art of Scientific Computing*. Cambridge University Press, 2007.

[29] E. Ortiz-Rivera and F. Peng, “Analytical model for a photovoltaic module using the electrical characteristics provided by the manufacturer data sheet,” *Power Electronics Specialists …*, pp. 2087–2091, 2005.

[30] D. J. Crain, J. E. Garland, S. E. Rock, and D. Roy, “Quantitative characterization of silicon solar cells in the electro-analytical approach: Combined measurements of temperature and voltage dependent electrical parameters,” *Analytical Methods*, vol. 4, no. 1, p. 106, 2012.

[31] X. Lingyun, S. Lefei, H. Wei, and J. Cong, “Solar Cells Parameter Extraction Using a Hybrid Genetic Algorithm,” in *2011 Third International Conference on Measuring Technology and Mechatronics Automation*, 2011, vol. 3, pp. 306–309.

[32] Z. Michalewicz and D. B. Fogel, *How to sovle it: Modern Heuristics*. 2004.

[33] J. A. Jervase, H. Bourdoucen, and A. Al-Lawati, “Solar cell parameter extraction using genetic algorithms,” *Measurement Science and Technology*, vol. 12, no. 11, pp. 1922–1925, Nov. 2001.

[34] N. Mohan, T. M. Undeland, and W. P. Robbins, *Power electronics: converters, applications, and design*, no. v. 1. John Wiley & Sons, 2003.

[35] R. P. Severns and G. Bloom, *Modern DC-to-DC switchmode power converter circuits*. Van Nostrand Reinhold Co., 1985, p. 342.

[36] T. Wu, C. Chang, and Y. Wu, “Single-stage converters for PV lighting systems with MPPT and energy backup,” *Aerospace and Electronic Systems, …*, vol. 35, no. 4, 1999.

[37] A. Testa, S. De Caro, D. Caniglia, V. Antonucci, M. Ferraro, and F. Sergi, “Compensation of the low frequency current ripple in single phase grid connected fuel cell power systems.” pp. 1–10, 2009.

[38] D. Diaz, D. Meneses, J. A. Oliver, O. Garcia, P. Alou, and J. A. Cobos, “Dynamic Analysis of a Boost Converter With Ripple Cancellation Network by Model-Reduction Techniques,” *IEEE Transactions on Power Electronics*, vol. 24, no. 12, pp. 2769–2775, Dec. 2009.

[39] H. Isoda, G. Kimura, M. Shioya, and M. H. Ohsato, “Battery charging characteristics in small scaled photovoltaic system using resonant DC-DC converter with electric isolation,” in *[Proceedings] IECON ’90: 16th Annual Conference of IEEE Industrial Electronics Society*, 1990, pp. 1118–1123.

[40] P. Bartholomeus and P. Le Moigne, “Battery charger with high quality input waveforms,” in *Proceedings of the IEEE International Symposium on Industrial Electronics*, 1995, vol. 2, pp. 574–579.

[41] E. Durán, J. M. Enrique, M. A. Bohorquez, M. Sidrach-de-Cardona, J. E. Carretero, and J. M. Andujar, “A new Application of the Coupled-Inductors SEPIC Converter to obtain I-V and P-V Curves of Photovoltaic Modules IL1 Zero Ripple Condition,” *European Conference on Power Electronics and Applications*, 2005.

[42] M. J. Schutten, R. L. Steigerwald, and J. A. Sabate, “Ripple current cancellation circuit,” in *Eighteenth Annual IEEE Applied Power Electronics Conference and Exposition, 2003. APEC ’03.*, 2003, vol. 1, pp. 464–470.

[43] D. C. Hamill and P. T. Krein, “A ‘zero’ ripple technique applicable to any DC converter,” in *30th Annual IEEE Power Electronics Specialists Conference. Record. (Cat. No.99CH36321)*, 1999, vol. 2, pp. 1165–1171.

[44] H. R. Visser and P. P. J. van den Bosch, “Modelling of periodically switching networks,” in *PESC ’91 Record 22nd Annual IEEE Power Electronics Specialists Conference*, 1991, pp. 67–73.

[45] N. Benavides and P. Chapman, “Modeling the effect of voltage ripple on the power output of photovoltaic modules,” *Industrial Electronics, IEEE ...*, vol. 55, no. 7, pp. 2638–2643, 2008.

[46] W. Kim, V.-H. Duong, T.-T. Nguyen, and W. Choi, “Analysis of the effects of inverter ripple current on a photovoltaic power system by using an AC impedance model of the solar cell,” *Renewable Energy*, vol. 59, pp. 150–157, Nov. 2013.

[47] J. Bordonau, R. M. Lamaison, and J. Peracaula, “An LCC DC/DC resonant converter designed for applications with variable load and output voltage,” *26th Annual IEEE Power Electronics Specialists Conference,*, pp. 292–297, 1995.

[48] C. Adragna, S. De Simone, and C. Spini, “Designing LLC resonant converters for optimum efficiency,” no. Mi.

[49] R.-L. Lin and W.-C. Ju, “LLC DC/DC Resonant Converter with PLL Control Scheme,” *APEC 07 - Twenty-Second Annual IEEE Applied Power Electronics Conference and Exposition*, pp. 1537–1543, Feb. 2007.

[50] A. Conesa, G. Velasco, H. Martinez, and M. Roman, “LCLC resonant converter as maximum power point tracker in PV systems,” *13th European Conference on Power Electronics and Applications, 2009. EPE ’09.*, pp. 1–9, 2009.

[51] M. P. Foster, D. A. Stone, and C. M. Bingham, “Phase Locked Loop (PLL) based self-oscillating controller for,” pp. 446–450.

[52] R. M. Lamaison, J. Bordonau, A. Esquivel, and J. Peracaula, “Analysis and design of a resonant battery charger for photovoltaic systems,” in *ISIE ’99. Proceedings of the IEEE International Symposium on Industrial Electronics (Cat. No.99TH8465)*, 1999, vol. 2, pp. 463–468.

[53] O. Mostaghimi, N. Wright, and A. Horsfall, “Design and performance evaluation of SiC based DC-DC converters for PV applications,” in *2012 IEEE Energy Conversion Congress and Exposition (ECCE)*, 2012, pp. 3956–3963.

[54] T. Williams, *EMC for Product Designers*. Elsevier Science, 2007.

[55] B. HU and S. SATHIAKUMAR, “A new interleaving technique for voltage ripple cancellation of series-connect photovoltaic systems,” *Journal of Circuits, Systems and Computers*, vol. 23, no. 04, p. 1450045, Apr. 2014.

[56] S.-Y. Tseng and C.-T. Tsai, “Photovoltaic Power System with an Interleaving Boost Converter for Battery Charger Applications,” *International Journal of Photoenergy*, vol. 2012, pp. 1–15, 2012.

[57] C.-W. Tsang, M. Foster, D. Gladwin, and D. Stone, “Active current ripple cancellation in parallel connected buck converter modules,” *IET Power Electronics*, vol. 6, no. 4, pp. 721–731, Apr. 2013.

[58] A. Testa and S. De Caro, “Active voltage ripple compensation in PV Systems for domestic uses,” in *2010 IEEE International Symposium on Industrial Electronics*, 2010, pp. 2193–2198.

[59] P. E. Marenholtz, “Programmable Solar Array Simulator,” *IEEE Transactions on Aerospace and Electronic Systems*, vol. AES-2, no. 6, pp. 104–107, Nov. 1966.

[60] E. Koutroulis, K. Kalaitzakis, and V. Tzitzilonis, “Development of an FPGA-based System for Real-Time Simulation of Photovoltaic Modules,” in *Seventeenth IEEE International Workshop on Rapid System Prototyping (RSP’06)*, 2006, pp. 200–208.

[61] D. S. L. Dolan and J. Durago, “Development of a photovoltaic panel emulator using Labview,” in *2011 37th IEEE Photovoltaic Specialists Conference*, 2011, pp. 001795–001800.

[62] G. Martin-Segura, J. Lopez-Mestre, M. Teixido-Casas, and A. Sudria-Andreu, “Development of a photovoltaic array emulator system based on a full-bridge structure,” in *2007 9th International Conference on Electrical Power Quality and Utilisation*, 2007, pp. 1–6.

[63] M. Ding and K. G. Gard, “Tanh cascode cell amplifier – an arbitrary transfer characteristics amplifier,” *Electronics Letters*, vol. 46, no. 22, p. 1495, 2010.

[64] “Magna-Power | High Power Programmable DC Power Supplies.” [Online]. Available: http://magna-power.com/. [Accessed: 26-Apr-2014].

[65] “E4360 Modular Solar Array Simulators | Agilent .”

[66] I. G. M. Mantera, “Optimum hydroelectric-power-generation scheduling by analogue computer,” *Proceedings of the Institution of Electrical Engineers*, vol. 118, no. 1, p. 110, 1971.

[67] R. J. A. Paul and E. L. Thomas, “The design and applications of a general-purpose analogue computer,” *Journal of the British Institution of Radio Engineers*, vol. 17, no. 1, pp. 49–73, Jan. 1957.

[68] F. D. Tan and R. D. Middlebrook, “Unified modeling and measurement of current-programmed converters,” in *Proceedings of IEEE Power Electronics Specialist Conference - PESC ’93*, 1993, pp. 380–387.

[69] R. D. Middlebrook, “Topics in Multiple-Loop Regulators and Current-Mode Programming,” *IEEE Transactions on Power Electronics*, vol. PE-2, no. 2, pp. 109–124, Apr. 1987.

[70] C. Rodriguez and G. A. J. Amaratunga, “Dynamic maximum power injection control of AC photovoltaic modules using current-mode control,” *IEE Proceedings - Electric Power Applications*, vol. 153, no. 1, p. 83, 2006.

[71] R. C. Dorf and R. H. Bishop, *Modern Control Systems*. Prentice Hall; 12 edition, 2010, p. 1104.

[72] S. Jayasuriya and M. H. Kotzebue, “Classical feedback control with matlab, Boris J. Lurie and Paul J. Enright, Marcel Dekker, Inc., New York, NY 2000 456 pages, ISBN 0-8247-0370-7.,” *International Journal of Robust and Nonlinear Control*, vol. 13, no. 10, pp. 1011–1013, Aug. 2003.

[73] C. J. Harris and S. A. Billings, *Self-tuning and adaptive control: theory and applications*. P. Peregrinus on behalf of the Institution of Electrical Engineers, 1981, p. 333.

[74] “Waste Electrical and Electronic Equipment (WEEE): implementing the recast Directive and UK system changes - Consultations - GOV.UK.” [Online]. Available: https://www.gov.uk/government/consultations/waste-electrical-and-electronic-equipment-weee-implementing-the-recast-directive-and-uk-system-changes. [Accessed: 26-Apr-2014].

[75] A. M. R. Amaral and A. J. M. Cardoso, “State condition estimation of aluminum electrolytic capacitors used on the primary side of ATX power supplies,” in *2009 35th Annual Conference of IEEE Industrial Electronics*, 2009, pp. 442–447.

[76] S.-A. Liang, “A high power and high efficiency PC power supply topology with low cost design to meet 80 Plus Bronze requirements,” in *2009 IEEE International Conference on Industrial Technology*, 2009, pp. 1–6.

[77] G. R. Walker, “Evaluating MPPT converter topologies using a MATLAB PV model,” *AUPEC 2000 : Innovation for Secure Power*. Queensland University of Technology, 27-Feb-2000.

[78] E. Gadjeva and M. Hristov, “Behavioral parameterized SPICE models of photovoltaic modules.” pp. 355–359, 2013.

[79] M. Patsalides, G. E. Georghiou, A. Stavrou, and V. Efthymiou, “Thevenin equivalent circuit for the study of high photovoltaic penetration in distribution grids,” in *IEEE PES ISGT Europe 2013*, 2013, pp. 1–5.

[80] A. Chatterjee and A. Keyhani, “Thevenin’s equivalent of photovoltaic source models for MPPT and power grid studies,” in *2011 IEEE Power and Energy Society General Meeting*, 2011, pp. 1–7.

[81] S. Chowdhury, G. A. Taylor, S. P. Chowdhury, A. K. Saha, and Y. H. Song, “Modelling, simulation and performance analysis of a PV array in an embedded environment,” in *2007 42nd International Universities Power Engineering Conference*, 2007, pp. 781–785.

[82] “Quick Links | National Climatic Data Center (NCDC).” [Online]. Available: http://www.ncdc.noaa.gov/data-access/quick-links. [Accessed: 26-Apr-2014].

[83] W. G. Driscoll, *Handbook of Optics*. McGraw-Hill, 1978, p. 1600.

[84] “Solar Spectral Irradiance: Air Mass 1.5.” [Online]. Available: http://rredc.nrel.gov/solar/spectra/am1.5/. [Accessed: 26-Apr-2014].

[85] R. J. Chaffin and G. C. Osbourn, “Measurement of concentrator solar cell series resistance by flash testing,” *Applied Physics Letters*, vol. 37, no. 7, p. 637, 1980.

[86] J. Summhammer, “Short flash and constant load PV-module tester,” in *IECON 2013 - 39th Annual Conference of the IEEE Industrial Electronics Society*, 2013, pp. 8116–8120.

[87] D. Jungwirth, L. C. Eigler, and S. Espiritu, “Advancements in solar simulators for terrestrial solar cells at high concentration (500 to 5000 Suns) levels,” in *2008 33rd IEEE Photovolatic Specialists Conference*, 2008, pp. 1–6.

[88] F. Bond and C. Cahn, “On the sampling the zeros of bandwidth limited signals,” *IEEE Transactions on Information Theory*, vol. 4, no. 3, pp. 110–113, Sep. 1958.

[89] B. Ji, J. Wang, and J. Zhao, “High-Efficiency Single-Phase Transformerless PV H6 Inverter With Hybrid Modulation Method,” *IEEE Transactions on Industrial Electronics*, vol. 60, no. 5, pp. 2104–2115, May 2013.

[90] D. Dong, X. Zhang, F. Luo, D. Boroyevich, and P. Mattavelli, “Common-mode EMI noise reduction for grid-interface converter in low-voltage DC distribution system,” in *2012 Twenty-Seventh Annual IEEE Applied Power Electronics Conference and Exposition (APEC)*, 2012, pp. 451–457.

[91] M. García-Gracia, N. El Halabi, H. Ajami, and M. P. Comech, “Integrated Control Technique for Compliance of Solar Photovoltaic Installation Grid Codes,” *IEEE Transactions on Energy Conversion*, vol. 27, no. 3, pp. 792–798, Sep. 2012.

[92] T. Williams, *EMC for Product Designers (Google eBook)*. Newnes, 2011, p. 512.

[93] F. Beltrame, F. H. Dupont, H. C. Sartori, E. C. Cancian, C. Rech, and J. R. Pinheiro, “Efficiency optimization of DC/DC boost converter applied to the photovoltaic system,” in *IECON 2013 - 39th Annual Conference of the IEEE Industrial Electronics Society*, 2013, pp. 706–711.

[94] E. Chou, F. Chen, C. Adragna, and B. Lu, “Ripple steering AC-DC converters to minimize input filter,” *2009 IEEE Energy Conversion Congress and Exposition*, pp. 1325–1330, Sep. 2009.

[95] D. S. L. Simonetti, J. Sebastion, and J. Uceda, “The discontinuous conduction mode Sepic and Cuk power factor preregulators: analysis and design,” *IEEE Transactions on Industrial Electronics*, vol. 44, no. 5, pp. 630–637, 1997.

[96] M. Veerachary, “Power tracking for nonlinear PV sources with coupled inductor SEPIC converter,” *IEEE transactions on aerospace and electronic …*, vol. 41, no. 3, 2005.

[97] J. Chen, “Analysis and design of SEPIC converter in boundary conduction mode for universal-line power factor correction applications,” *2001 IEEE 32nd Annual Power Electronics Specialists Conference (IEEE Cat. No.01CH37230)*, vol. 2, pp. 742–747.

[98] H. Sewell, D. Stone, and D. Howe, “Dynamic load impedance correction for induction heaters,” *Power Electronics and Drive …*, no. July, pp. 110–115, 1999.

[99] H. Chung and K. Tse, “A novel maximum power point tracking technique for solar panels using a SEPIC or Cuk converter,” *Power Electronics, …*, vol. 18, no. 3, pp. 717–724, 2003.

[100] “ATX12V Design Guide - Version 2.01 - ATX12V PSDG2.01.pdf.” [Online]. Available: http://www.formfactors.org/developer/specs/ATX12V PSDG2.01.pdf. [Accessed: 26-Apr-2014].

[101] “Computer Repairs | WEEE Recycling | Fulfilment | Aspire Sheffield.” [Online]. Available: http://www.aspire-sheffield.co.uk/. [Accessed: 27-Apr-2014].

[102] C. Lee Sirio, “Analysis of Line Current Harmonics for Single-Phase PFC Converters,” in *2007 IEEE Power Electronics Specialists Conference*, 2007, pp. 1291–1297.

[103] A. Hamadi, S. Rahmani, and K. Al-Haddad, “A Novel Hybrid Series Active Filter for Power Quality Compensation,” in *2007 IEEE Power Electronics Specialists Conference*, 2007, pp. 1099–1104.

[104] K.-H. Liu and Y.-L. Lin, “Current waveform distortion in power factor correction circuits employing discontinuous-mode boost converters,” in *20th Annual IEEE Power Electronics Specialists Conference*, 1989, pp. 825–829.

[105] M. F. Schlecht and B. A. Miwa, “Active Power Factor Correction for Switching Power Supplies,” *IEEE Transactions on Power Electronics*, vol. 2, no. 4, pp. 273–281, 1987.